8-1-2017

Using molecular dynamics to quantify biaxial membrane damage in a multiscale modeling framework for traumatic brain injury

Michael Anthony Murphy

Using molecular dynamics to quantify biaxial membrane damage in a multiscale modeling framework for traumatic brain injury

By

Michael Anthony Murphy

A Dissertation
Submitted to the Faculty of
Mississippi State University
in Partial Fulfillment of the Requirements
for the Degree of Doctor of Philosophy
in Biomedical Engineering
in the Department of Agricultural and Biological Engineering

Mississippi State, Mississippi

August 2017

Using molecular dynamics to quantify biaxial membrane damage in a multiscale modeling framework for traumatic brain injury

By

Michael Anthony Murphy

Approved:

Lakiesha N. Williams (Co-Major Professor)	Rajkumar Prabhu (Co-Major Professor)
Mark F. Horstemeyer (Committee Member)	Steven Gwaltney (Committee Member)

Tonya W. Stone
(Committee Member)

Michelle C. LaPlaca
(Committee Member)

Steven H. Elder
(Graduate Coordinator)

Jason M. Keith
Dean
Bagley College of Engineering

Name: Michael Anthony Murphy

Date of Degree: August 11, 2017

Institution: Mississippi State University

Major Field: Biomedical Engineering

Co-Major Professors: Dr. Lakiesha N. Williams, Dr. Rajkumar Prabhu

Title of Study: Using molecular dynamics to quantify biaxial membrane damage in a multiscale modeling framework for traumatic brain injury

Pages in Study: 134

Candidate for Degree of Doctor of Philosophy

The current study investigates the effect of strain state, strain rate, and membrane planar area on phospholipid bilayer mechanoporation and failure. Using molecular dynamics, a 1-palmitoyl-2-oleoyl-phosphatidylcholine (POPC) bilayer was deformed biaxially to represent injury-induced neuronal membrane mechanoporation and failure. For all studies, water forming a bridge through both phospholipid bilayer leaflets was used as a failure metric. To examine the effect of strain state, 72 phospholipid structures were subjected to equibiaxial, 2:1 non-equibiaxial, 4:1 non-equibiaxial, strip biaxial, and uniaxial tensile deformations at the von Mises strain rate of $5.45 \times 10^8\ s^{-1}$. The stress magnitude, failure strain, headgroup clustering, and damage behavior were strain state dependent. The strain state order of detrimentality in descending order was equibiaxial, 2:1 non-equibiaxial, 4:1 non-equibiaxial, strip biaxial, and uniaxial with failure von Mises strains of 0.46, 0.47, 0.53, 0.77, and 1.67, respectively. Additionally, pore nucleation, growth, and failure were used to create a Membrane Failure Limit Diagram (MFLD) to demonstrate safe and unsafe membrane deformation regions. This MFLD allowed representative equations to be derived to predict membrane failure from in-plane

strains. To examine the effect of strain rate, the equibiaxial and strip biaxial strain states were repeated at multiple strain rates. Additionally, a 144 phospholipid structure, which was twice the size of the 72 phospholipid structure in the x dimension, was subjected to strip biaxial tensile deformations to examine planar area effect. The applied strain rates, planar area, and cross-sectional area had no effect on the von Mises strains at which pores greater than 0.1 nm^2 were detected (0.509 plus/minus 7.8%) or the von Mises strain at failure (0.68 plus/minus 4.8%). Additionally, changes in bilayer planar and cross-sectional areas did not affect the stress response. However, a strain rate increase from 1.4 $\times 10^8$ to 6.8 $\times 10^8$ s^{-1} resulted in a yield stress increase of 44.1 MPa and a yield strain increase of 0.17. Additionally, a stress and mechanoporation behavioral transition was determined to occur at a strain rate of ~1.4 $\times 10^8$ s^{-1}. These results provide the basis to implement a more accurate mechano-physiological internal state variable continuum model that captures lower-length scale damage.

DEDICATION

This research is dedicated to Mary K. Murphy, my wife, who has given me strength and supported me through this process.

To Aaron Moses Murphy and Abigail Sapphira Murphy, my son and daughter, who are learning the wonders of this world and helping me to see the world anew while giving me the motivation to finish.

To Charles and Sharlene Murphy, my parents, who pushed me to be curious and to explore my interests no matter where they took me and supported me to the best of their abilities.

To all my friends and family who continue to help me grow both intellectually, emotionally, and spiritually.

And to God, who has given me guidance, strength, and patience to get through this process. He has blessed me in so many ways and has provided me with the individuals in my life who have helped me through it.

ACKNOWLEDGEMENTS

I would like to acknowledge groups and individuals who contributed to the completion of this work. A special thank you to Dr. Lakiesha Williams and Dr. Rajkumar Prabhu, my major professors, who served as guides both in work and life and were always willing to listen when truly needed. I also would like to acknowledge Dr. Steven Gwaltney, Dr. Mark Horstemeyer, Dr. Tonya Stone, and Dr. Michelle LaPlaca, the remaining members of my graduate committee. They have shared so much time and knowledge with me and have been huge sources of knowledge and guidance in completing this work.

I would also like to acknowledge the support of the many professors and staff of Mississippi State University and my fellow graduate students, so many of whom were willing to give guidance, help, knowledge, or just lend an ear when needed.

Lastly, I would like to acknowledge the organizations that have supported this work and made it possible. The National Science Foundation (NSF) Experimental Program to Stimulation Competitive Research (EPSCoR) and the Department of Defense (DoD) U.S. Army Engineer Research and Development Center (ERDC) Computational Research for Engineering and Science Ground Vehicles (CRES-GV) programs have provided the financial support needed for this work. Additionally, the Department of Agricultural and Biological Engineering and the Center for Advanced Vehicular Systems

(CAVS) supported this work, which included the computational resources provided through CAVS.

TABLE OF CONTENTS

APPENDIX

LIST OF TABLES

LIST OF FIGURES

CHAPTER I

INTRODUCTION

While traumatic brain injury (TBI) is not a new phenomenon, it has recently gained popular recognition in the American public eye due to high-profile injury causes, such as football and boxing athletes. In reality, TBI is much more widespread with TBI-related medical visits being reported for more than 10 million individuals every year [1], of which approximately 1.7 million are in the United States [2], meaning the number of individuals affected is likely much higher. Additionally, falls and car accidents are a much more common mode of injury that is not as publicized [2]. These injuries result in both human and economic losses, which may be short- or long-term [3]. In the worst-case scenario, an individual suffering a TBI can die due to the injury or the related complications. Along with the loss of life and immediate death-related expenses, the TBI-related death would result in losses related to any familial, societal, or professional roles the individual served. In non-death scenarios, losses come from diagnostic exams and, ideally, successful, injury treatment in the short-term. In the long-term, TBI can lead to chronic symptoms including behavioral changes and motor function problems, among many other symptoms [2]. These symptoms can lead to permanent disability, cause social interactions to dramatically change, and prevent individuals from working as they did before injury.

To reduce the rate at which TBIs and other injuries occur, many regulatory safety device standards have been developed and are often mandated for many activities with a high probability of injury. A few examples are air bags in motor vehicles, helmets in many sports, and hard hats in construction. However, the designs for these devices are often not optimal and can be expensive to test using headforms or full-body dummies to represent a human, which may not even represent the human body well. To aid in optimizing these devices and reducing testing costs, computational models can be implemented. One common macroscale method is Finite Element Analysis (FEA), where a structure is treated as a continuum with specified material properties to obtain approximated answers [4]. These answers are strongly affected by the underlying material model's properties and its ability to accurately reproduce the simulated structure's geometry [4]. These models allow designers to change and test a wide variety of parameters without the manufacturing costs or test dummy damage risk, such as when optimizing a football facemask geometry to reduce TBI [5]. However, they do not inherently capture phenomena from length scales lower than that which is being simulated and lack physiological details, necessitating these features be implemented using a multiscale modelling paradigm.

One such multiscale modeling paradigm is the Integrated Computational Materials Engineering (ICME) modeling hierarchy [4]. The ICME paradigm allows lower length scale effects to be introduced in the computational material model through internal state variables. These effects result in more accurate answers and allow for temperature, strain rate, stress state, and history effects to be modelled [4, 6]. The ICME paradigm describes how to scale down from higher length scales to narrow the properties

needed from lower length scales [4]. Simulations and experiments can then be performed to obtain these properties and scaled up as part of the material model to give history and stress state material behavioral effects. Overall, downscaling leads to material models that are less complex with reduced development costs when compared to a similar multiscale model with all properties included. This benefit is particularly helpful when the investigated material is expensive or otherwise difficult to acquire for experimental studies. The ICME paradigm has been implemented in a variety of systems, such as in a motor vehicle control arm and aluminum alloy weapons carrier [6]. For example, in the control arm example, the ICME method accurately predicted the failure location where using a stress or microstructural analysis approach alone failed [6]. This example shows the importance of structure inhomogeneity, history effects, and the progression of damage.

This importance is especially true when one begins to consider materials of biological origin where structure variability is greater and partially deformed structures cannot be analyzed as easily experimentally. With inorganic materials, experimental samples typically can be examined long after the test through a variety of methods without significant sample change after deformations. However, biological tissue samples begin undergoing chemical processes, including decay, nearly immediately following removal from their original host. These processes can significantly affect the mechanical properties and often require a complex testing apparatus for simple tests. Additionally, the samples are typically soft enough to deform under their own weight and must be chemically fixed post experiment to stain and image. These differences make it more difficult to view deformation mechanisms due to testing. Further, tissues often have

several structural levels, meaning the macroscale, mesoscale, and nanoscale may all have different structures. Each of these length scales must be examined to understand the resulting macroscale mechanical properties. For example, tendons have the structural levels of collagen molecules, collagen fibrils, collagen fibers, primary fiber bundle (subfascicle), secondary fiber bundle (fascicle), tertiary fiber bundle, and, finally, the macroscale tendon level [7]. These structural levels start on the nanoscale and extend to the mesoscale with structure diameters of several millimeters [7]. Another biological example is the structure of spider silk, which has molecular sequence-structure correlations that relate to the overall spider silk strength [8]. Testing the silk on the macroscale would have never provided the information needed to make this finding. The ideas behind multiscale modeling also extends into bioinspired design. Bosia, et al. [9] performed hierarchical multiscale simulations when trying to design high strength nanofibers based on the structure of spider silk. This idea of needing to examine the multiple structure levels also extends to the brain, where the length scales would be the brain (organ-macroscale), tissue (groups of cells-mesoscale), cells (microscale), and subcellular (cell organelles and other cellular components-nanoscale and atomic scale). These length scales have several important structural aspects, such as the overall brain shape and its interaction with the brain; sulci and gyri on the tissue level; soma, axons, and dendrites on the cellular level; and the membrane, among other structures, on subcellular level.

Current brain models include both experimental and computational models. The best model would be the human brain itself, which can be examined using imaging techniques, such magnetic resonance imaging (MRI). Improvements in imaging

techniques have helped understand many aspects of TBI by allowing *in vivo* observations [10]. However, imaging can only be used to view TBI post-injury and is limited both by resolution and the time it takes to administer and perform the imaging scan. Other recent attempts to study traumatic brain injury have focused on trying to replicate the damaging effects of TBI experimentally. By performing tests on standardized lab animals, TBI can be observed and then documented along with the type and magnitude of the impact used [11, 12]. However, these experiments are also limited by imaging techniques and they necessitate animal models be sacrificed if cell staining is desired for brain damage analysis. On the microscale, cell models using culture deformation and micropipette aspiration have been used to capture cell deformation behavior. While these experiments capture the effect of deformations on cell death through the tracking of biomarkers on the mesoscale [13-15], they cannot easily quantify the local strain, strain rate, or strain state applied to the membrane [16]. Alternatively, FEA models have been used to create models of the brain and models of parts of the brain [17-26]. These studies implemented constitutive models to replicate the anisotropic material properties of brain to obtain more accurate stress responses [17-26]. However, these FEA models do not have material models that adequately describe the different levels of the brain. Additionally, biological materials often do not have a simple failure point, such as many inorganic materials which fracture, because they are a combination of smaller dissimilar structures and can even self-repair in many cases. This dissimilarity means that molecular dynamics is needed to examine damage mechanisms to obtain information needed for FEA constitutive material models. Of particular interest is the cell membrane because

membrane mechanoporation has been shown to be an important injury mechanism during TBI [27-30].

Investigations of membrane deformations show that the idea of nanoscale deformations having important implications for cellular and tissue well-being has become widely accepted [31-44]. Experimentally, examining the bilayer has largely dealt with determining structural and mechanical properties. The fluid nature of the phospholipid bilayer structure was officially noted by Frye and Edidin [31], who used immunofluorescent antigen markers to observe the movement of phospholipids in the cell membrane. Methods to deform phospholipid structures have been developed as well. A few of note are micropipette aspiration via a vacuum [32-34], electric fields [35], and atomic force microscopy (AFM) [36, 37]. Micropipette aspiration has long provided a method of testing phospholipid bilayers. Using this method, a micropipette is used to aspirate phospholipid structures while measuring the pressure which allows for the stress at failure to be determined and elastic moduli to be determined. One example of this is Needham and Nunn [34] who investigated the effects of cholesterol concentration on the rupture strength of phospholipid vesicles and the area compressibility modulus. Additionally, Evans, et al. [32] used micropipette aspiration to determine defect-limited and cavitation-limited equations for the rupture strength of vesicles in the loading rate range of 0.01-100 $\mathrm{mN \cdot m^{-1} \cdot s^{-1}}$.

Despite micropipette aspiration being the most common method for finding mechanical properties, other methods have also been used. For example, when dealing with sub-freezing temperatures is a concern, using micropipette aspiration is not practical and electric fields are needed to examine mechanical properties [35]. AFM is another

alternative method that allows the membrane to be deformed. AFM uses a cantilever beam equipped with a sharp tip for which a laser and photodiode are used to measure the cantilever deflections [36]. The AFM is a diverse tool with multiple modes to determine both structural and mechanical properties of specimens [36]. Although the resolution of the AFM is similar to that of scanning electron microscopy (SEM), AFM does not require the sample to be fixed in place before imaging and can even be used to examine living biological specimens [36]. This fact is a great advantage when dealing with biological specimens because they are constantly changing and the act of chemically fixing a cell will kill it and can leave significant artifacts. AFM has also been used to study unsupported phospholipid bilayers and to determine values such as the bending modulus and adhesion constant [45]. However, when using AFM an appropriate elastic model must be selected or the results will not be correct [36, 37]. While these experimental methods have provided valuable details, they do not adequately allow the deformation mechanisms to be explored due to multiple factors, such as time and length scales, imaging difficulty, and deformation rates limitations.

To overcome these limitations, the molecular dynamics (MD) method can be used to represent and interpret nanoscale physical phenomena, such as membrane deformations. Several molecular dynamics studies have previously examined deforming phospholipid bilayer structures and the resulting pore response [38-44]. Many of these deformed the bilayer under a state of tension based on the lateral in-plane pressures. Tieleman, et al. [38] varied the lateral plane pressure to deform the lipid bilayer. This applied lateral pressures resulted in pore nucleation at higher pressures and led to phospholipid bilayer destabilization. They also noted that during the mechanical

deformations the phospholipid bilayer thinned considerably in the perpendicular direction. Leontiadou, et al. [39] used this method to display that pores were stable at low lateral pressures when the pore was inserted prior to simulations and resulted in rupture at higher lateral pressures. However, controlling the deformations in this fashion is imprecise when considering the rate at which the bilayer is deformed, which can affect the properties of the phospholipid bilayer. Additionally, controlling deformations using pressure can result in tearing the bilayer apart due to barostat feedback rather than pore nucleation [40].

Alternatively, the phospholipid bilayer can be deformed under tension via changing the dimensions of the in-plane box dimensions and in effect allowing the phospholipids to adjust to the box. Tomasini, et al. [41] used incremental tension to deform the bilayer equibiaxially in the lateral plane, but the deformations are performed with relaxation periods between each stretch. These increments do not represent a continuous deformation. Koshiyama and Wada [42-44] performed simulations using equibiaxial tension using unsteady state stretching in the in-plane direction by using coordinate scaling. This provided a continuous deformation method to allow the phospholipid bilayer to form pores without allowing the structure to partially recover between changes in tension. The predominance of these studies examined the phospholipid bilayer under equibiaxial tensile deformations. However, Tomasini, et al. [41] also simulated shear between the bilayer leaflets by generating an uneven acceleration profile dependent on the z height of each individual atom.

Previous *In silico* deformation studies have focused primarily on equibiaxial deformations with little focus given to other strain states. The studies included here seek

to expand this knowledge by exploring membrane stress and mechanoporation damage in the framework of a multiscale model of TBI. The first study examines the effect of different strain states on membrane deformations by simulating the equibiaxial, 2:1 non-equibiaxial, 4:1 non-equibiaxial, strip biaxial, and uniaxial strain paths using the molecular dynamics method. For each, the resulting stress-strain, pore nucleation, pore growth, damage, and membrane failure are examined. These properties were used to create a novel visualization tool, the Membrane Failure Limit Diagram (MFLD), that allows potential membrane failure to be determined using only the strains. The second study explores the effect of strain rate and structure size when simulating the strip biaxial strain state. The effects of modifying these properties are explored through their effects on pore nucleation and growth, stress, and failure responses. This study also showed that a stress and pore growth behavioral transition may occur on the low end of the strain rates examined. To examine this potential behavioral transition, the third study examines a wider range of strain rates using the equibiaxial and strip biaxial strain states. By using the empirical relation derived by Evans, et al. [32] for defect-limited failure of phospholipid bilayer deformations at high deformation rates, the loading rate was related to the yield and failure strains to find the behavioral transition strain rate. Together, these studies give data needed to develop the nanoscale length scale in the b multiscale mechano-physiological internal state variable (MPISV) material model for TBI.

1.1 References

[1] A. A. Hyder, C. A. Wunderlich, P. Puvanachandra, G. Gururaj, and O. C. Kobusingye, "The impact of traumatic brain injuries: A global perspective," *NeuroRehabilitation,* vol. 22, 2007.

[2] M. Faul, L. Xu, M. M. Wald, and V. G. Coronado, "Traumatic Brain Injury in the United States: Emergency Department Visits, Hospitalizations, and Deaths 2002-2006," ed. Atlanta (GA): Centers for Disease Control Prevention, National Center for Injury Prevention and Control, 2010.

[3] I. Humphreys, R. L. Wood, C. J. Phillips, and S. Macey, "The costs of traumatic brain injury: a literature review," *ClinicoEconomics and outcomes research : CEOR,* vol. 5, pp. 281-7, 2013. doi: 10.2147/CEOR.S44625.

[4] M. F. Horstemeyer, *Integrated Computational Materials Engineering (ICME) for Metals: Using Multiscale Modeling to Invigorate Engineering Design with Science*: Wiley, 2012.

[5] K. L. Johnson, S. Chowdhury, W. B. Lawrimore, Y. Mao, A. Mehmani, R. Prabhu*, et al.*, "Constrained topological optimization of a football helmet facemask based on brain response," *Materials & Design,* vol. 111, pp. 108-118, 2016. doi: 10.1016/j.matdes.2016.08.064.

[6] M. F. Horstemeyer and P. Wang, "Cradle-to-grave simulation-based design incorporating multiscale microstructure-property modeling: Reinvigorating design with science," *Journal of Computer-Aided Materials Design,* vol. 10, pp. 13-34, 2003. doi: 10.1023/b:jcad.0000024171.13480.24.

[7] P. Kannus, "Structure of the tendon connective tissue," *Scandinavian Journal of Medicine & Science in Sports,* vol. 10, pp. 312-320, 2000. doi: 10.1034/j.1600-0838.2000.010006312.x.

[8] G. Bratzel and M. J. Buehler, "Sequence-structure correlations in silk: Poly-Ala repeat of N. clavipes MaSp1 is naturally optimized at a critical length scale," *Journal of the Mechanical Behavior of Biomedical Materials,* vol. 7, pp. 30-40, 2012. doi: 10.1016/j.jmbbm.2011.07.012.

[9] F. Bosia, M. J. Buehler, and N. M. Pugno, "Hierarchical simulations for the design of supertough nanofibers inspired by spider silk," *Phys Rev E Stat Nonlin Soft Matter Phys,* vol. 82, p. 056103, Nov 2010.

[10] M. F. Kraus, T. Susmaras, B. P. Caughlin, C. J. Walker, J. A. Sweeney, and D. M. Little, "White matter integrity and cognition in chronic traumatic brain injury: a diffusion tensor imaging study," *Brain,* vol. 130, pp. 2508-2519, October 1, 2007 2007. doi: 10.1093/brain/awm216.

[11] I. Cernak, B. Stoica, K. R. Byrnes, S. D. Giovanni, and A. I. Faden, "Role of the Cell Cycle in the Pathobiology of Central Nervous System Trauma," *Cell Cycle,* vol. 4, pp. 1286-1293, 2005.

[12] M. T. Begonia, R. Prabhu, J. Liao, W. R. Whittington, A. Claude, B. Willeford*, et al.*, "Quantitative analysis of brain microstructure following mild blunt and blast trauma," *Journal of Biomechanics,* vol. 47, pp. 3704-3711, 11/28/ 2014. doi: 10.1016/j.jbiomech.2014.09.026.

[13] M. LaPlaca and L. Thibault, "Anin vitro traumatic injury model to examine the response of neurons to a hydrodynamically-induced deformation," *Annals of Biomedical Engineering,* vol. 25, pp. 665-677, 1997/07/01 1997. doi: 10.1007/BF02684844.

[14] M. C. LaPlaca, D. K. Cullen, J. J. McLoughlin, and R. S. Cargill Ii, "High rate shear strain of three-dimensional neural cell cultures: a new in vitro traumatic brain injury model," *Journal of Biomechanics,* vol. 38, pp. 1093-1105, 2005/05// 2005. doi: 10.1016/j.jbiomech.2004.05.032.

[15] M. C. LaPlaca and G. R. Prado, "Neural mechanobiology and neuronal vulnerability to traumatic loading," *Journal of Biomechanics,* vol. 43, pp. 71-78, 1/5/ 2010. doi: 10.1016/j.jbiomech.2009.09.011.

[16] D. K. Cullen, V. N. Vernekar, and M. C. LaPlaca, "Trauma-Induced Plasmalemma Disruptions in Three-Dimensional Neural Cultures Are Dependent on Strain Modality and Rate," *Journal of Neurotrauma,* vol. 28, pp. 2219-2233, 2011/11/01 2011. doi: 10.1089/neu.2011.1841.

[17] R. J. H. Cloots, H. M. T. Gervaise, J. A. W. van Dommelen, and M. G. D. Geers, "Biomechanics of Traumatic Brain Injury: Influences of the Morphologic Heterogeneities of the Cerebral Cortex," *Annals of Biomedical Engineering,* vol. 36, pp. 1203-1215, 2008/07/01 2008. doi: 10.1007/s10439-008-9510-3.

[18] N. C. Colgan, M. D. Gilchrist, and K. M. Curran, "Applying DTI white matter orientations to finite element head models to examine diffuse TBI under high rotational accelerations," *Progress in Biophysics and Molecular Biology,* vol. 103, pp. 304-309, 12// 2010. doi: 10.1016/j.pbiomolbio.2010.09.008.

[19] R. Prabhu, M. F. Horstemeyer, Y. Mao, J. L. Bouvard, E. B. Marin, L. N. Williams*, et al.*, "Simulation Based Analysis of an Experimentally Quantified Traumatic Brain Injury from an In-Theater Blast Explosion.," *(Under review, PNAS),* 2014.

[20] K. Miller, "Constitutive model of brain tissue suitable for finite element analysis of surgical procedures," *Journal of Biomechanics,* vol. 32, pp. 531-537, 1999/05// 1999. doi: 10.1016/S0021-9290(99)00010-X.

[21] K. K. Mendis, R. L. Stalnaker, and S. H. Advani, "A Constitutive Relationship for Large Deformation Finite Element Modeling of Brain Tissue," *Journal of Biomechanical Engineering,* vol. 117, pp. 279-285, 1995. doi: 10.1115/1.2794182.

[22] R. Prabhu, M. F. Horstemeyer, M. T. Tucker, E. B. Marin, J. L. Bouvard, J. A. Sherburn*, et al.*, "Coupled experiment/finite element analysis on the mechanical response of porcine brain under high strain rates," *Journal of the Mechanical Behavior of Biomedical Materials,* vol. 4, pp. 1067-1080, 2011. doi: 10.1016/j.jmbbm.2011.03.015.

[23] B. Rashid, M. Destrade, and M. D. Gilchrist, "Mechanical characterization of brain tissue in tension at dynamic strain rates," *Forensic Biomechanics,* vol. 33, pp. 43-54, 2014/05// 2014. doi: 10.1016/j.jmbbm.2012.07.015.

[24] T. El Sayed, A. Mota, F. Fraternali, and M. Ortiz, "Biomechanics of traumatic brain injury," *Computer Methods in Applied Mechanics and Engineering,* vol. *197*, pp. 4692-470, 2008. doi: 10.1016/j.cma.2008.06.006.

[25] B. Rashid, M. Destrade, and M. D. Gilchrist, "Mechanical characterization of brain tissue in compression at dynamic strain rates," *Journal of the Mechanical Behavior of Biomedical Materials,* vol. 10, pp. 23-38, 2012/06// 2012. doi: 10.1016/j.jmbbm.2012.01.022.

[26] B. Rashid, M. Destrade, and M. D. Gilchrist, "Mechanical characterization of brain tissue in simple shear at dynamic strain rates," *Journal of the Mechanical Behavior of Biomedical Materials,* vol. 28, pp. 71-85, 2013/12// 2013. doi: 10.1016/j.jmbbm.2013.07.017.

[27] O. Farkas, J. Lifshitz, and J. T. Povlishock, "Mechanoporation Induced by Diffuse Traumatic Brain Injury: An Irreversible or Reversible Response to Injury?," *J Neurosci,* vol. 26, pp. 3130-40, Mar 22 2006. doi: 10.1523/JNEUROSCI.5119-05.2006.

[28] D. Kilinc, G. Gallo, and K. A. Barbee, "Mechanically-induced membrane poration causes axonal beading and localized cytoskeletal damage," *Experimental Neurology,* vol. 212, pp. 422-430, 8// 2008. doi: 10.1016/j.expneurol.2008.04.025.

[29] D. M. Geddes, R. S. Cargill, 2nd, and M. C. LaPlaca, "Mechanical stretch to neurons results in a strain rate and magnitude-dependent increase in plasma membrane permeability," *J Neurotrauma,* vol. 20, pp. 1039-49, Oct 2003. doi: 10.1089/089771503770195885.

[30] O. Farkas and J. T. Povlishock, "Cellular and subcellular change evoked by diffuse traumatic brain injury: a complex web of change extending far beyond focal damage," in *Progress in Brain Research*. vol. Volume 161, T. W. John and I. R. M. Andrew, Eds., ed: Elsevier, 2007, pp. 43-59.

[31] L. D. Frye and M. Edidin, "The Rapid Intermixing of Cell Surface Antigens After Formation of Mouse-Human Heterokaryons," *Journal of Cell Science,* vol. 7, pp. 319-335, September 1, 1970 1970.

[32] E. Evans, V. Heinrich, F. Ludwig, and W. Rawicz, "Dynamic tension spectroscopy and strength of biomembranes," *Biophys J,* vol. 85, pp. 2342-50, Oct 2003. doi: 10.1016/S0006-3495(03)74658-X.

[33] E. Evans and B. A. Smith, "Kinetics of Hole Nucleation in Biomembrane Rupture," *New J Phys,* vol. 13, Sep 16 2011. doi: 10.1088/1367-2630/13/9/095010.

[34] D. Needham and R. S. Nunn, "Elastic deformation and failure of lipid bilayer membranes containing cholesterol," *Biophysical Journal,* vol. 58, pp. 997-1009, 10// 1990. doi: 10.1016/S0006-3495(90)82444-9.

[35] F. Thom, "Mechanical properties of the human red blood cell membrane at −15 degrees C," *Cryobiology,* vol. 59, pp. 24-27, 8// 2009. doi: 10.1016/j.cryobiol.2009.04.001.

[36] L. Picas, P.-E. Milhiet, and J. Hernández-Borrell, "Atomic force microscopy: A versatile tool to probe the physical and chemical properties of supported membranes at the nanoscale," *Chemistry and Physics of Lipids,* vol. 165, pp. 845-860, 12// 2012. doi: 10.1016/j.chemphyslip.2012.10.005.

[37] E. Ovalle-García, J. J. Torres-Heredia, A. Antillón, and I. n. Ortega-Blake, "Simultaneous Determination of the Elastic Properties of the Lipid Bilayer by Atomic Force Microscopy: Bending, Tension, and Adhesion," *The Journal of Physical Chemistry B,* vol. 115, pp. 4826-4833, 2011/04/28 2011. doi: 10.1021/jp111985z.

[38] D. P. Tieleman, H. Leontiadou, A. E. Mark, and S. J. Marrink, "Simulation of pore formation in lipid bilayers by mechanical stress and electric fields," *J Am Chem Soc,* vol. 125, pp. 6382-3, May 28 2003. doi: 10.1021/ja029504i.

[39] H. Leontiadou, A. E. Mark, and S. J. Marrink, "Molecular dynamics simulations of hydrophilic pores in lipid bilayers," *Biophys J,* vol. 86, pp. 2156-64, Apr 2004. doi: 10.1016/S0006-3495(04)74275-7.

[40] T. V. Tolpekina, W. K. den Otter, and W. J. Briels, "Simulations of stable pores in membranes: system size dependence and line tension," *J Chem Phys,* vol. 121, pp. 8014-20, Oct 22 2004. doi: 10.1063/1.1796254.

[41] M. D. Tomasini, C. Rinaldi, and M. S. Tomassone, "Molecular dynamics simulations of rupture in lipid bilayers," *Experimental Biology and Medicine (Maywood, N.J.),* vol. 235, pp. 181-8, Feb 2010. doi: 10.1258/ebm.2009.009187.

[42] K. Koshiyama and S. Wada, "Molecular dynamics simulations of pore formation dynamics during the rupture process of a phospholipid bilayer caused by high-speed equibiaxial stretching," *Journal of Biomechanics,* vol. 44, pp. 2053-8, 2011/07/28/ 2011. doi: 10.1016/j.jbiomech.2011.05.014.

[43] T. Shigematsu, K. Koshiyama, and S. Wada, "Effects of Stretching Speed on Mechanical Rupture of Phospholipid/Cholesterol Bilayers: Molecular Dynamics Simulation," *Scientific Reports,* vol. 5, p. 15369, 10/16/online 2015. doi: 10.1038/srep15369.

[44] T. Shigematsu, K. Koshiyama, and S. Wada, "Molecular dynamics simulations of pore formation in stretched phospholipid/cholesterol bilayers," *Chemistry and Physics of Lipids,* vol. 183, pp. 43-49, 10// 2014. doi: 10.1016/j.chemphyslip.2014.05.005.

[45] L. Picas, F. Rico, and S. Scheuring, "Direct Measurement of the Mechanical Properties of Lipid Phases in Supported Bilayers," *Biophysical Journal,* vol. 102, pp. L01-L03, 1/4/ 2012. doi: 10.1016/j.bpj.2011.11.4001.

CHAPTER II

MOLECULAR DYNAMICS SIMULATIONS SHOWING 1-PALMITOYL-2-OLEOYL-PHOSPHATIDYLCHOLINE (POPC) MEMBRANE MECHANOPORATION DAMAGE UNDER DIFFERENT STRAIN PATHS

2.1 Introduction

In the United States, approximately 1.7 million new cases of traumatic brain injury (TBI) result in human and economic losses every year [1, 2]. Further, TBI is estimated to affect more than 10 million people globally resulting in hospitalization or death [3]. Falls and motor vehicle accidents are the top scenarios resulting in TBI [1], pointing to a need for better protective equipment, such as motor vehicle air bags. These scenarios can cause physical insults to the head and can result in stress wave propagation and physiological damage in the brain [4-6]. Current brain material models use internal state variables (ISV) focused on mechanical properties and lack lower length scale physiological effects [7-11]. However, physiological aspects must also be incorporated to accurately model TBI, creating the need for a Mechano-Physiological Internal State Variable (MPISV) material model. Therefore, a better brain material model is critical for evaluating and increasing the effectiveness of protective equipment. While it is currently not feasible, and likely unnecessary, to incorporate all physiological injury mechanisms into the models, specific mechanisms can be quantified and incorporated into the MPISV

model. One important physiological injury mechanism is neuron membrane mechanoporation, which can have devastating results biologically, including neuron death [12, 13]. Membrane integrity is important to the well-being of the neuron because the membrane tightly regulates molecular diffusion and maintains the intracellular ion homeostasis [14, 15]. Any disruption of intracellular ion concentrations, specifically intracellular calcium ions, has been shown to trigger a number of pathways both resulting in membrane repair (vesicle-plasma membrane fusion) and apoptosis or necrosis based on the level of disruption [14-17]. By quantifying neuron membrane mechanoporation, membrane damage can be calculated as the product of pore nucleation and growth, as has been extensively performed for metals [18-20]. Implementing these damage properties in the MPISV model to capture injury effects from mechanoporation is crucial for macroscale brain models used in human-centric design.

Considering the multiscale structure of the human brain [21], a multiscale approach would be logical to capture the brain's mechanical behavior. Implementing MPISV would allow for the most important variables to be considered at each length scale. ISV theory has previously been implemented to capture complex material behavior for a range of materials, such as metals [19, 20], polymers [22], and biological tissues [10]. Of importance is the ability of ISV theory to capture strain rate dependence, strain state dependence, and history effects through ISVs. Thus, ISV theory allows a more accurate macroscale material model to be created [23]. Implementing these properties across length scales is critical to capturing neuronal cell death thresholds through the disruption of the membrane integrity [11, 24-27]. The characterization of these ISVs and

the final model, however, require the use of experimental and computational research to capture the phenomena at their respective length scales.

Experimentally, cell culture deformation and micropipette aspiration have been used to capture cell behavior during microscale membrane deformations. Cell culture deformation experiments capture the effect of deformation on cell death through the tracking of biomarkers on the mesoscale [28-30] but cannot easily quantify the local strain, strain rate, or strain state applied to the membrane [31]. Using micropipette aspiration to apply equibiaxial surface tension to phospholipid structures has also been used to capture rupture strength and elastic constants [32-36]. However, pore nucleation cannot be readily captured at the meso- or micro-scale experimentally. To capture damage due to mechanoporation, lower length scale (nanoscale) simulations are required to observe pore nucleation and evolution (damage) during membrane deformation.

Molecular dynamics can be used to perform these lower length scale simulations. Multiple previous studies have investigated the phospholipid bilayer when deformed *in silico* [21, 25, 37-41]. However, these studies typically focused on the equibiaxial strain state and did not adequately quantify the pore nucleation and evolution behavior in sufficient detail to implement in an MPISV model [25, 37, 38, 40, 41]. The assumption of equibiaxial stresses is appropriate for non-deformation scenarios because the bilayer would experience equibiaxial stresses during typical cellular processes where intracellular pressures would dominate stresses placed on the cell membrane. However, multiple strain states would be present on the lower length scale during injury, so other strain states must be accounted for. Exceptions are Tomasini, et al. [39], who considered surface shear along with the equibiaxial strain state to investigate nanoparticle induced

mechanical damage, and Murphy, et al. [21], who considered the pore nucleation and evolution behavior during the strip biaxial strain state. These studies have found that the stress behavior is highly strain rate dependent when deformed at a constant stretching speed [21, 25, 40]. Additionally, while pore nucleation and evolution have been observed to change considerably with strain rate [35], they are unaffected by strain rate within the strain rate range currently considered [21]. In this study, the strain state dependency for the stress-strain and the pore nucleation and evolution behavior due to phospholipid bilayer mechanoporation are evaluated, and a membrane failure limit diagram is developed.

2.2 Methods

2.2.1 Simulation Details

Structure equilibrations, deformations, and failure determination were performed as described in Murphy, et al. [21]. Briefly, a structure containing 72 1-palmitoyl-2-oleoylphosphatidylcholine (POPC) phospholipid and 9,070 TIP3P water molecules (original structure sourced from Klauda, et al. [42] and 6,828 TIP3P water molecules were added) was equilibrated for ten nanoseconds and deformed under a constant temperature of 310 K using the program LAMMPS [43] and the CHARMM36 all-atom lipid force field [42]. The deformation parameters were modified from Murphy, et al. [21] to examine the effect of strain state. The equilibrated structure was subjected to constant velocity deformations in the x and y dimensions, shown in Table 2.1, correlating to the von Mises strain rate $\dot{\varepsilon}_{VM} = 5.5 \times 10^8\ s^{-1}$, while the z dimension was allowed to adjust freely under a pressure of 1 atm. Figure 2.1 shows representative schematics for the examined strain states. Additionally, each equilibration and set of deformations were

performed three times using different velocity seed numbers to obtain averaged results from different initial structures.

Table 2.1 Summary of Deformation Velocities Correlating to a von Mises Strain Rate ($\dot{\varepsilon}_{VM}$) of 5.5×10^8 s^{-1}

Strain State	Initial Structure	$\dot{\varepsilon}_y/\dot{\varepsilon}_x$	v_x ($m \cdot s^{-1}$)	v_y ($m \cdot s^{-1}$)
Equibiaxial Tension	1	1	4.0	3.8
	2	1	3.7	4.0
	3	1	4.0	3.7
2:1 Non-Equibiaxial Tension	1	½	4.6	2.2
	2	½	4.3	2.3
	3	½	4.6	2.1
4:1 Non-Equibiaxial Tension	1	¼	4.4	1.0
	2	¼	4.4	1.1
	3	¼	4.5	1.0
Strip Biaxial Tension	1	0	4.0	0
	2	0	3.7	0
	3	0	4.0	0
Uniaxial Tension	1	-	4.0	Pressure of 1 atm
	2	-	3.7	
	3	-	4.0	

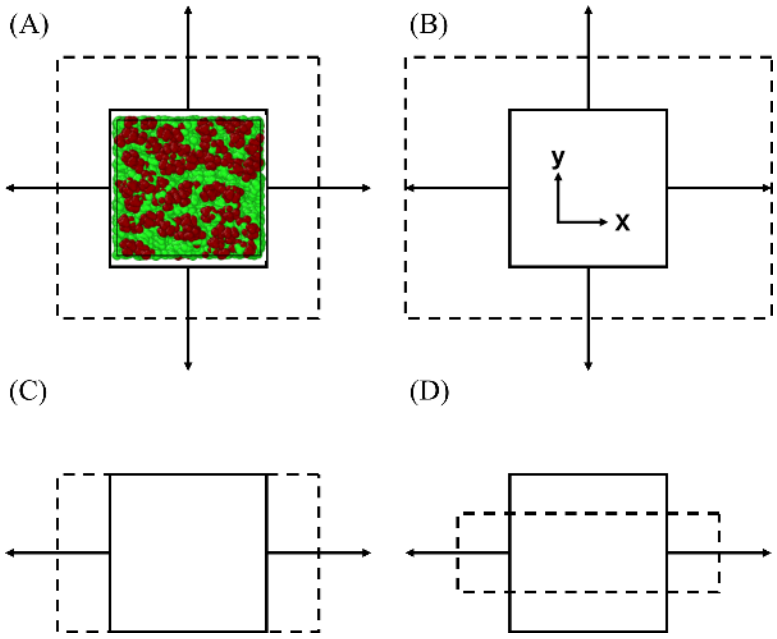

Figure 2.1 Representative perpendicular (top) schematic of the deformations performed for (A) equibiaxial, (B) non-equibiaxial, (C) strip biaxial, and (D) uniaxial tension.

Solid and dashed lines represent the undeformed and deformed structures, respectively. The phospholipid structure overlay in (A) shows red for phospholipid headgroups and green for phospholipids tails.

2.3 Analysis

Qualitative image analysis was performed using OVITO [44] with atom radii set according to van der Waals radii [45]. Periodic images were displayed, showing a 3x3x1 (a total of 9 boxes) structure, so all pores large enough for detection were displayed fully in at least one location when viewed from the perpendicular (top) view. All atoms were colored black and rendered every 5 ps using the default options. A custom MATLAB [46] function was used to analyze these images. Partial pores on the exterior periodic image boundaries and duplicate pores due to periodic images were removed. Remaining pores were used to determine pore density, mean pore area, and initial pore nucleation strains for properties of interest. Damage was then calculated using the equation $\phi = \eta \upsilon c$,

where ϕ is damage, η is nucleation, υ is growth, and c is coalescence [20]. In this case, nucleation (η) is pore density, and the product of pore growth and coalescence (υ*c) is the mean pore area. This image analysis was performed for pores with a minor axis length greater than 0 Å to detect all pores, 3 Å to detect pores large enough to allow passage of water [47], and 10 Å to detect pores large enough to allow penetration of a calcium ion with two hydration layers [48]. Due to periodic boundaries, the final data point for qualitative and quantitative analyses was determined for each simulation to be when any pore exceeded the box dimension.

For quantitative analysis, von Mises stress and strain were used as described in Murphy, et al. [21] using a moving average with an interval of 5 ps. Yield was determined to be when the overall slope of the von Mises stress-strain curve turned negative. The use of von Mises strain is necessary for quantifying deformations to allow a comparison between strain states. The simulation box was orthogonal with no shear strains. Therefore, shear strains and uncontrolled dimensions in the von Mises strain equation (z, xy, xz, and yz) were assumed zero, which reduced the von Mises strain equation to $\varepsilon_{VM} = (2/9 * [(\varepsilon_x - \varepsilon_y)^2 + (\varepsilon_x)^2 + (\varepsilon_y)^2])^{0.5}$, where von Mises strain is ε_{VM} and ε_x, ε_y are the principle in-plane true strains of the simulation box. This equation was also used to determine an equivalent von Mises strain rate, by replacing ε_x and ε_y with their corresponding strain rates, to allow comparison of equivalent strain states. Although $\dot{\varepsilon}_y$ was assumed to be zero when calculating the equivalent von Mises strain rate for the uniaxial case, ε_y was included in strain calculations.

2.4 Results

2.4.1 Stress-Strain Behavior

Figure 2.2 shows how the applied strain state affected the stress-strain behavior and failure. The stress quickly increased initially while exhibiting two linear regions before peaking and decreasing more slowly for all strain path simulations. The yield stress varied depending on the strain path, with the equibiaxial strain path simulations exhibiting the highest yield stress, and the uniaxial and strip biaxial strain path simulations exhibiting the lowest yield stresses (Figure 2.2). Additionally, all strain path simulations, except uniaxial, exhibited a similar yield strain (Figure 2.2, Table 2.2). Despite the similar von Mises stress behavior for the strip biaxial and uniaxial strain path simulations, the component stresses were significantly different with the strip biaxial strain path simulations having higher component stresses (Figure A.1 in APPENDIX A).

Figure 2.2 shows the failure (water penetration) strain was lowest for the equibiaxial and 2:1 non-equibiaxial strain path simulations and highest for the uniaxial strain path simulations. A large difference was observed between the lowest and highest observed failure strains with the average uniaxial strain path simulation's failure strain being over three times the average for the equibiaxial strain path simulations.

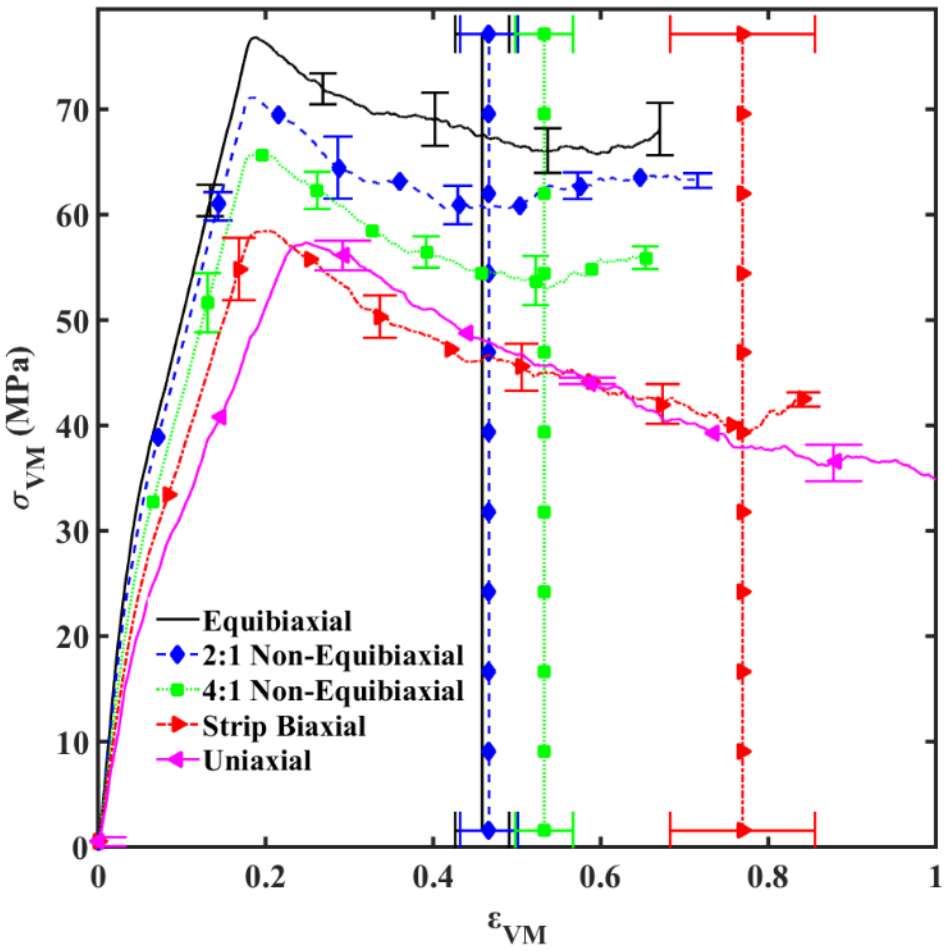

Figure 2.2 Average von Mises stress versus strain curve displaying the effect of strain state (equibiaxial, 2:1 non-equibiaxial, 4:1 non-equibiaxial, strip biaxial, and uniaxial) at $\dot{\varepsilon}_{VM} = 5.5 \times 10^8\ s^{-1}$.

Vertical lines with markers matching their corresponding curve display when full water penetration occurred. Penetration for the uniaxial strain state is not shown, but the average penetration occurred at $\varepsilon_{VM} = 1.635 \pm 11.6\%$.

Table 2.2 Equibiaxial, 2:1 Non-Equibiaxial, 4:1 Non-Equibiaxial, Strip Biaxial, and Uniaxial Mechanical Properties of the 72 Phospholipid Bilayer

Strain State	σ^{VM}_{Yield} (MPa)	ε^{VM}_{Yield}	$\varepsilon^{VM}_{FirstPore}$ (d ≥ 3 Å)	$\varepsilon^{VM}_{Failure}$	$\varepsilon^{VM}_{FirstPore}$ (d ≥ 10 Å)
Equibiaxial	76.7	0.185	0.314	0.459	0.484
2:1 Non-Equibiaxial	71.1	0.182	0.345	0.467	0.525
4:1 Non-Equibiaxial	65.6	0.182	0.417	0.533	0.569
Strip Biaxial	58.4	0.187	0.561	0.769	0.826
Uniaxial	57.2	0.239	1.205	1.665†	n/a
Average	65.8	0.195 (0.184*)	0.568 (0.410*)	0.778 (0.557*)	0.601
Rel StDev (%)	12.6	12.7 (1.3*)	64.8 (26.9*)	65.7 (26.1*)	25.6
P-Value (95%)	<0.01	<0.01	0.03	<0.01	<0.01
P-Value (95%)*	<0.01	0.2197	<0.01	<0.01	<0.01

† Calculated using two data points
* Values calculated when excluding the uniaxial strain state
$p < 0.05$ significantly different; $p > 0.05$ not significantly different for one-way ANOVA

2.4.2 Pore Nucleation and Evolution

Table 2.2 shows that pores sufficiently large to theoretically allow water (d = 3 Å [47]) and calcium ions with two hydration layers (d = 10 Å [48]) occurred for all strain path simulations except the uniaxial strain path simulations, which only developed pores large enough to allow water penetration. For both pore size thresholds, the strains for initial detection were lowest for the equibiaxial strain path simulations and increased as the y strain rate to x strain rate ratio became smaller (reference Table 2.1 for the ratios). Figure 2.3(A-E) shows a representative progression of phospholipid bilayer pore evolution for each strain state simulation via snapshots correlated to von Mises stress-strain curves. Note the change in scale in each sub-figure. Deformations of the phospholipid bilayer resulted in yield and initial pore nucleation near the yield stress for the equibiaxial, 2:1 non-equibiaxial, and 4:1 non-equibiaxial strain path simulations. Initial pore detection for the strip biaxial and uniaxial strain path simulations were at greater strains compared to the aforementioned strain path simulations. The snapshots in

Figure 2.3(A-E) show that pores nucleated and then grew large enough to theoretically allow calcium penetration for all simulations except those for the uniaxial strain state. During this deformation process, phospholipid headgroups spread out differently depending on the strain state, which resulted in clusters of phospholipid headgroups. This clustering has been quantified using the mean nearest neighbor distance, shown in Figure 2.3(F).

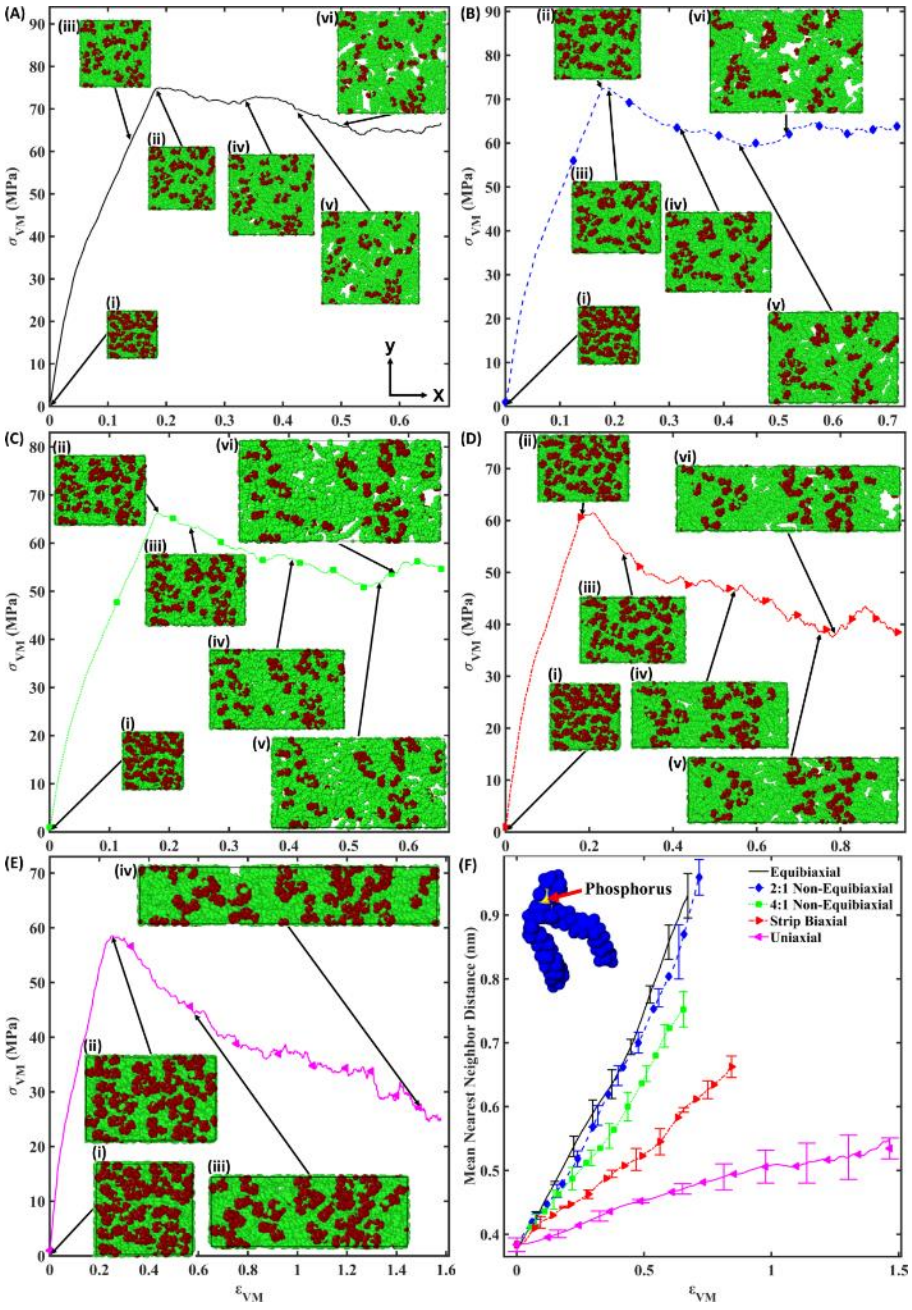

Figure 2.3 Representative von Mises stress versus von Mises strain curves for the (A) equibiaxial, (B) 2:1 non-equibiaxial, (C) 4:1 non-equibiaxial, (D) strip biaxial, and (E) uniaxial strain states at $\dot{\varepsilon}_{VM} = 5.5 \times 10^8$ s^{-1} and (F) corresponding mean nearest neighbor distance curves for phospholipid headgroup phosphorus atoms.

Top view snapshots of the phospholipid bilayer (water hidden) show the phospholipid bilayer with red phospholipid headgroups and green phospholipid tails at the (i) initial structure (x and y dimensions of 48.9 Å x 46.1 Å for the shown structure), (ii) first yield stress, (iii) first pore with diameter larger than 0 Å, (iv) first pore with diameter larger than 3 Å, (v) initial full water penetration, and (vi) the first pore with diameter larger than 10 Å.). In (F), phosphorus is colored yellow and non-phosphorus atoms are colored blue.

2.4.3 Phospholipid Bilayer Damage

In Figure 2.4, the pore number density serves as a quantification of pore nucleation η to calculate damage. The nucleation quickly increased for the equibiaxial, 2:1 non-equibiaxial, and 4:1 non-equibiaxial strain path simulations. The strip biaxial and uniaxial strain path simulations resulted in lower nucleation rates. Figure 2.5 shows that the mean pore area, which is equivalent to the product of pore growth and coalescence (υc) portion of the damage equation but will be referred to as pore growth for simplicity, increases as the applied deformation increases. The equibiaxial and 2:1 non-equibiaxial strain path simulations yield the same pore growth rates. The pore growth magnitude decreased progressively as the strain path changed from 4:1 non-equibiaxial to strip biaxial strain paths. Despite the 4:1 non-equibiaxial strain path simulations resulting in lower pore nucleation and growth, the error bars show that pore nucleation and growth were not significantly different for the equibiaxial, 2:1 non-equibiaxial, and 4:1 non-equibiaxial strain path simulations. Figure 2.6(A) shows that the resulting damage curves maintain the similarity between the equibiaxial and 2:1 non-equibiaxial strain path simulations. However, the average damage is more separated between the two strain paths when compared to pore number density in Figure 2.4 and mean pore area in Figure 2.5. Further, as expected from the pore nucleation and growth results, the strip biaxial strain path simulations resulted in less damage than the more equibiaxial strain path simulations. Figure 2.6(B) also displays the amount of damage when water penetration (failure) occurred. The uniaxial strain path simulations resulted in negligible nucleation, pore growth, and damage for the strains presented, so the uniaxial strain state has been omitted from Figure 2.4, Figure 2.5, and Figure 2.6.

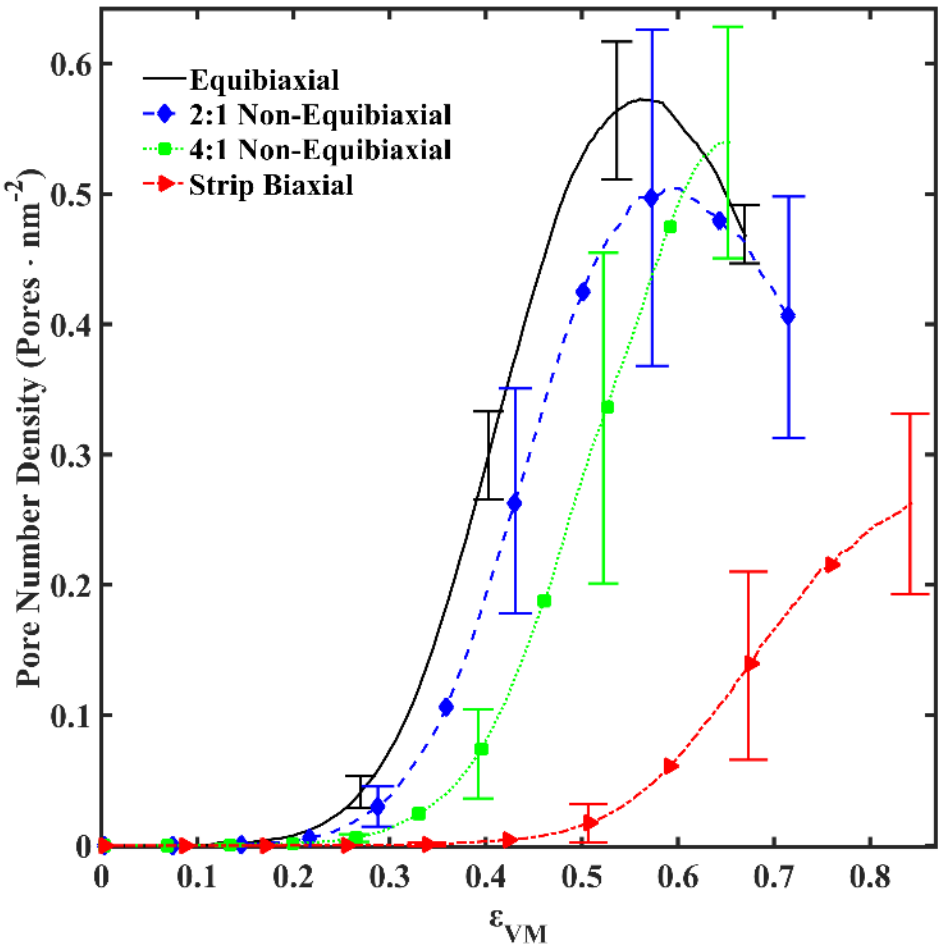

Figure 2.4 Pore number density (pore nucleation) versus von Mises strain for the equibiaxial, 2:1 non-equibiaxial, 4:1 non-equibiaxial, strip biaxial, and uniaxial strain path simulations.

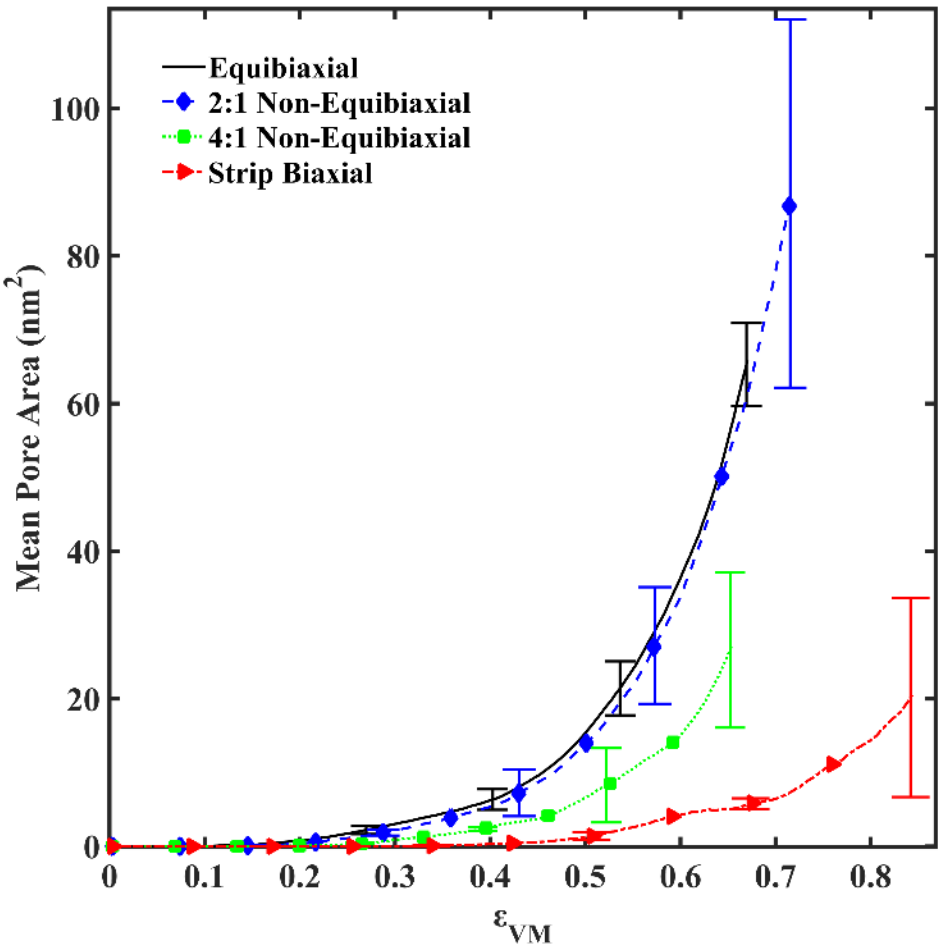

Figure 2.5 Mean pore area (pore growth and coalescence) versus von Mises strain for the equibiaxial, 2:1 non-equibiaxial, 4:1 non-equibiaxial, strip biaxial, and uniaxial strain path simulations.

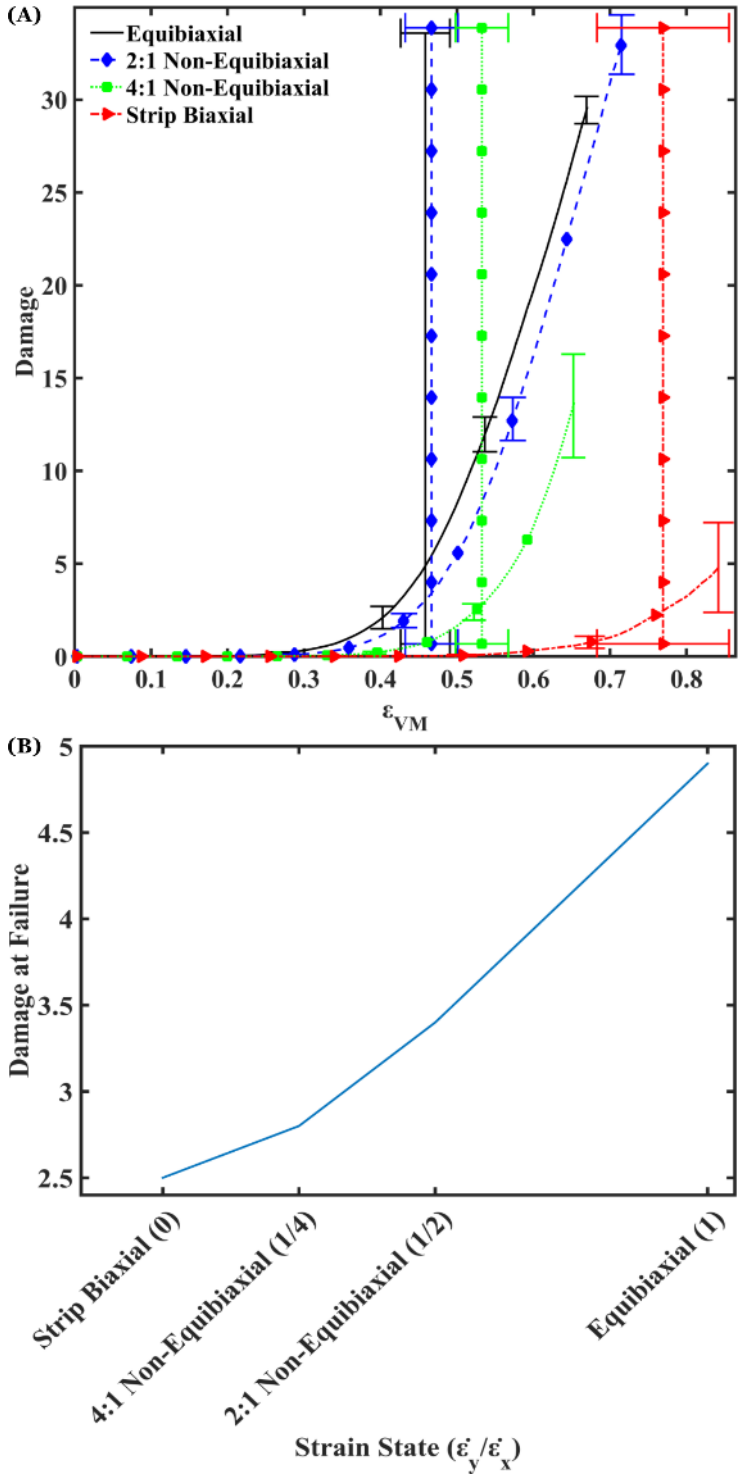

Figure 2.6 (A) Damage (ϕ) versus von Mises strain and (B) damage at failure versus strain state for the equibiaxial, 2:1 non-equibiaxial, 4:1 non-equibiaxial, and strip biaxial strain states.

In (A), vertical lines with markers corresponding to when full water penetration occurred.

2.4.4 Membrane Failure Limit Diagram

Due to sheet metal being planar in nature like the phospholipid bilayer, taking inspiration from methods used to describe sheet metal failure can yield interesting methods for describing the phospholipid bilayer. For example, the forming limit diagram (FLD) tool can be used to determine strains at which different sheet metal forming methods will result in failure [49-51]. By creating a two-dimensional (2-D) strain space, the FLD shows the strains at which failure is likely to occur for each strain state in a easy to interpret format [49-51]. The forming limit diagram is constructed by plotting the major and minor strains against one another, which creates limit lines that indicate if a structure is likely to fail within a given strain space [49-51].

This concept has been adopted in the current study to construct a limit diagram for the simulated phospholipid bilayer, shown in Figure 2.7, that includes multiple traumatic brain injury related phenomena. To distinguish this diagram from the traditional FLD diagram, the name Membrane Failure Limit Diagram (MFLD) has been adopted. Strain limit lines for yield, first detected pore, first pore large enough for water diffusion, failure, and first pore large enough for calcium diffusion are shown. These limit lines help to determine where bilayer deformations can be considered safe, potentially unsafe, and unsafe. In this way, the MFLD provides a simplified way to determine when mechanoporation and failure are likely to occur by designating zones where the phospholipid bilayer is considered safe, possibly failed (transitional), and definitely failed based on the in-plane bilayer strains arising from damage analysis. In Figure 2.7, these zones are colored green, blue, and red, respectively, for easy recognition. Because the

phospholipid bilayer is symmetric, the MFLD can also be mirrored on the equibiaxial strain line, but has been left unmirrored for simplicity.

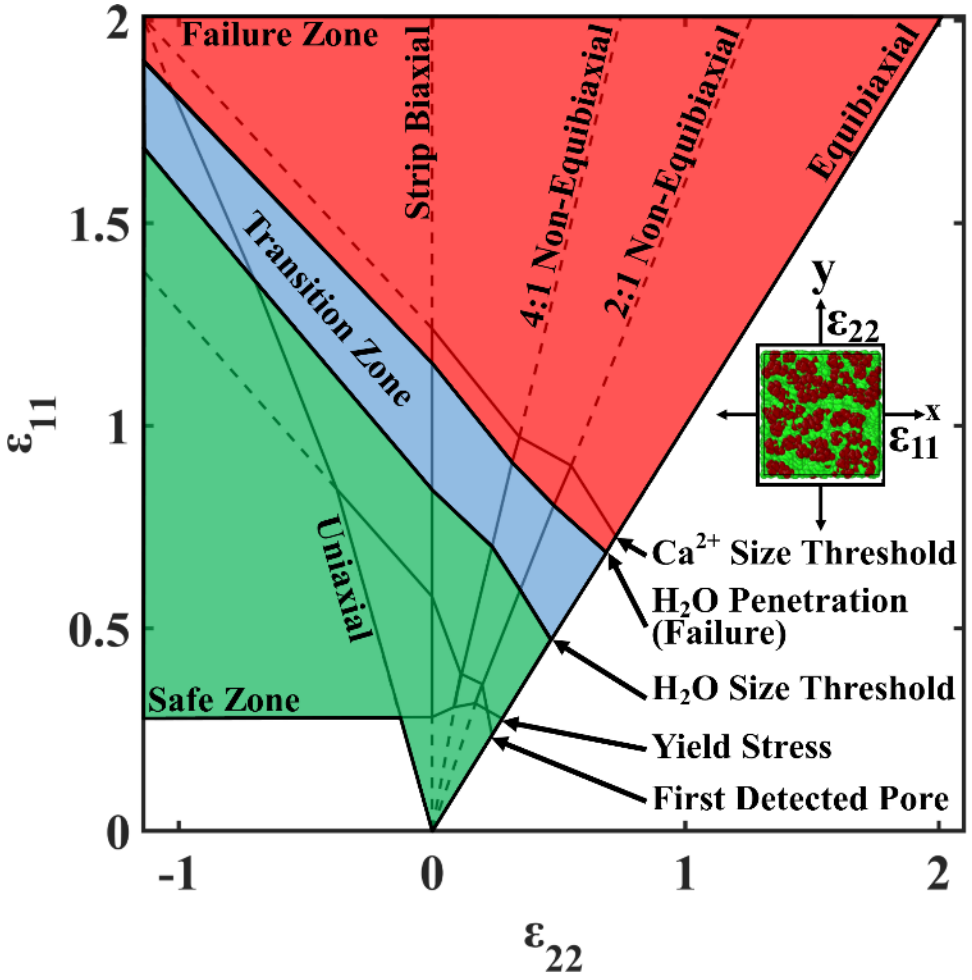

Figure 2.7 Average ε_{22} - ε_{11} true strain Membrane Failure Limit Diagram (MFLD) for the initial yield stress, first detected pore, water size threshold (d = 3 Å), water penetration, and calcium size threshold (d = 10 Å) for equibiaxial, non-equibiaxial, strip biaxial, and uniaxial tension deformations at $\dot{\varepsilon}_{VM} = 5.5 \times 10^8\ s^{-1}$.

The zones indicate expected damage with the Failure Zone (red) being dangerous strains, Transition Zone (blue) being potentially dangerous strains, and the Safe Zone (green) being safe strains.

2.5 Discussion

The effect of strain state on the resulting stress and damage behavior for phospholipid bilayer deformations at high rates has been examined in the current study. By investigating the resulting mechanoporation and damage of the phospholipid bilayer, simulation results give an idea of the damage due to deformations. The strain rate and strain state dependent stress and damage behavior of the phospholipid bilayer provide needed microstructural evolution data relevant for damage implementation in multiscale TBI constitutive models. Previous *in silico* deformation studies have primarily focused on deforming the phospholipid bilayer equibiaxially [25, 37-39, 52], but multiple strain states are essential for the development of a multiscale constitutive model for simulating diverse injury scenarios. To obtain a better understanding of TBI and the nanoscale mechanical insult leading to neuron injury, it is necessary to examine multiple strain states. Our previous work began this endeavor through an investigation of the rate and model size dependency of the phospholipid bilayer when subjected to the strip biaxial strain state [21]. The current research study applies mechanical deformations to the phospholipid bilayer to investigate phospholipid bilayer mechanoporation (deformation and failure) under the equibiaxial, non-equibiaxial, strip biaxial, and uniaxial strain states at the equivalent von Mises strain rate of 5.5×10^8 s^{-1}. This von Mises strain rate arose from velocities in the range of 1-4.6 m/s (Table 2.1), depending on the simulated strain path and loading direction, which includes velocities in the range listed by the NOCSAE football helmet standards for testing safety efficacy [53] and seen in experimental animal impact models [54]. Von Mises strain and von Mises stress were calculated to quantify

the mechanical behavior to deformations, and image analysis was used to quantify pore nucleation and evolution for damage analysis.

2.5.1 Stress-Strain Behavior

The real-world boundary value problem of neuronal cell deformations necessitates the stress-strain behavior for multiple strain states be quantified. However, previous phospholipid bilayer simulation studies have primarily focused on the equibiaxial strain state [25, 37-41]. Here, the elastic region, yield, and failure are explored for the stress-strain curves.

Because of phospholipids' short tail lengths, the two linear regions observed in the stress-strain curves (Figure 2.2) are likely governed by Rouse dynamics, where the resistance to change is due to molecular chains being pulled across one another rather than entanglement, as has been found previously for diffusion in phospholipid membranes [55]. For the forced membrane deformations currently examined, these two distinct linear regions are possibly due to chain rotation or straightening. However, investigating structural changes for these linear regions will be the focus of future studies and is not addressed further in the current paper. The phospholipid bilayer then "yielded" and began to soften, resulting in a stress decrease. This type of curve is consistent with findings for the strip biaxial strain state at similar strain rates [21], where Murphy, et al. [21] stated that deforming the bilayer at sufficiently high strain rates, which include the currently examined strain rate, inhibits efficient phospholipid rearrangement and energetically favorable pore growth. By forcefully pulling the phospholipid apart at higher strain rates, the phospholipid tails disengage in a way that prevents an energetically favorable structure from forming. Conversely, phospholipid tails allowed to

separate at a slower pace during lower strain rates may account for the for an extended peak stress-strain region before yielding occurs, as seen in some previous studies [25, 39].

Excluding the uniaxial strain state, the similarity in (von Mises) yield strain for all the strain states (Table 2.2) ($p = 0.2197$) indicates the yield strain is independent of the strain state when the strain state is biaxial. However, the yield stress was dependent on strain state ($p < 0.01$). Figure 2.2 shows this dependence, where the strip biaxial and uniaxial strain path simulations had a yield stress similar in magnitude, but the yield stress increased in magnitude as the simulated strain path became more equibiaxial. A previous study has shown the yield stress increases when the membrane is deformed at increasing strain rates, which also increases the loading rate (slope of stress versus time) [21]. Therefore, the difference in yield stress suggests the resulting loading rates may have varied between the simulated strain paths. The authors confirmed this thought using stress versus time curves (Figure A.2 in APPENDIX A), which showed the equibiaxial strain path simulations resulted in a loading rate ~1.45 times greater than the uniaxial strain path simulations. This difference means the equibiaxial strain state results in a greater loading rate even under a comparable equivalent strain rate. Murphy, et al. [21] also found that increasing strain rate increased the yield strain. Combined with the current finding that strain state has no effect on the yield strain even though it has an apparent effect on loading rate means that the yield strain is determined by strain rate, not loading rate. These findings mean that when these parameters are implemented into the MPISV model they may need to be based on different independent variables.

The difference in failure (water penetration) strain was strain state dependent based on a one-way ANOVA ($p < 0.01$). While the observed failure strains in the strain path simulations increased in the order of equibiaxial, 2:1 non-equibiaxial, and 4:1 non-equibiaxial, a Tukey post-hoc test revealed that the differences in failure strain were not statistically significant for these strain path simulations. The failure strain was statistically greater for the strip biaxial and then uniaxial strain path simulations. In particular, the average failure strain for the uniaxial strain path simulations was over three times the failure strain of the equibiaxial strain path simulations (Table 2.2). Because the failure strain increases as the strain state becomes less equibiaxial, the increasing failure strain shows that the failure strain is dependent on how much the phospholipids are pulled in both directions. This observation means the membrane is most likely to fail due to an applied tensile hydrostatic pressure or biaxial strain state. Conversely, the strain path simulations with the highest failure strain, uniaxial, is the least likely to be observed under native physiological conditions on the local scale. A strain state dependent failure strain has an interesting implication when considering the previous findings of Murphy, et al. [21], who showed the failure strain to be strain rate independent for the strip biaxial strain state in the current loading range. Importantly, membrane failure being dependent only on strain state means it is possible to develop rate independent equations, within the given loading range, for predicting bilayer failure during a given strain state. An equation predicting failure is discussed further in Section 2.5.3. First, however, pore nucleation and evolution, which are needed to implement the MPISV constitutive model, are discussed.

2.5.2 Pore Nucleation, Evolution, and Damage

Pore nucleation and evolution are affected by strain state when the membrane is deformed. The sequence of pore nucleation and evolution has been discussed previously for the strip biaxial strain state [21]. As the bilayer deformed, pores nucleated under small strains, indicating internal voids nucleating between phospholipids. Further deformation allowed nucleated pores to grow larger than 3 Å in diameter, which is theoretically large enough to allow passage of water molecules [47]. However, full water penetration (failure) required that water penetrate through both leaflets independently and connect to form a water bridge between the leaflets. Because of this process, there was a delay between when water could theoretically penetrate (based on image analysis—Section 2.3) and when water penetrated the membrane. Additionally, current findings show that pores experiencing water penetration quickly grow large enough to also allow diffusion of calcium ions.

Several observations can be made regarding pore nucleation and evolution based on the representative snapshots in Figure 2.3(A-E) and Table 2.2. First, the typical order of events of interest in terms of increasing strain was yield, first detectable pore, first pore large enough for water molecule diffusion, failure, and first pore large enough for calcium ion diffusion. The exception to this order was the equibiaxial strain path simulations, which nucleated a pore before yield. While the uniaxial strain path simulations did not grow pores large enough for calcium ion diffusion, it followed the same order of events as the other strain path simulations. As mentioned in Section 2.5.1, the yield strain is strain state independent for the non-uniaxial strain path simulations. The same is not true for the other mechanical properties. For each observed property, the

measured strain differences were statistically significant (Table 2.2). Strains for the equibiaxial strain path simulations were the lowest. However, despite the pore nucleation and evolution strains being greater for the 2:1 and then 4:1 non-equibiaxial strain path simulations, the differences found were not statistically significant using the Tukey post-hoc test.

Additionally, the snapshots in Figure 2.3(A-E) show the phospholipid headgroups cluster differently depending on the simulated strain paths. This headgroup clustering has been quantified using mean nearest neighbor distance [56], shown in Figure 2.3(F). Here, phospholipid headgroups clustered the least and were similar in the equibiaxial and 2:1 non-equibiaxial strain path simulations. The 4:1 non-equibiaxial, strip biaxial, and uniaxial strain states, ranked in that order, had significantly more phospholipid headgroup clustering. The reason for this difference can be viewed visually in Figure 2.3(A-E). The phospholipid headgroups follow the box deformations and the magnitude thereof. In other words, the equibiaxial strain path simulations' phospholipids clustered the least because they move equally in the x and y dimensions, and the uniaxial strain path simulations' phospholipids clustered the most because the x dimension is pulled while the y dimension is allowed to relax in a Poisson manner. This finding shows that each strain state induces phospholipid headgroup localization in the membrane. This localization may have significant localized effects on the way ions interact with a deforming membrane including potentially limiting excitotoxic accumulation in the cell. For example, a denser cluster of phospholipid headgroups will create a region that is more attractive to ions, which may help to steer the ions away from growing pores in the exposed phospholipid tail areas. Further experimental studies on phospholipid headgroup

clustering needs to be carried out to confirm this assertion. If confirmed, a localization metric could be quantified to determine the localized strain states in a deformed cell's membrane. Observing this metric in experimental studies of cells would help to determine if a cell is more or less likely to suffer damage and potential loss of homeostasis during deformation due to localized strain states.

As explained in Section 2.3, image analysis was used to identify and record properties for pores of defined sizes. This analysis showed the simulated strain path affected both pore nucleation and growth due to mechanoporation ($p < 0.01$). The peak in pore nucleation, which is explicitly shown for two strain states but would occur in others given further deformations (Figure 2.4), suggests the rate of pore coalescence has exceeded the rate of pore nucleation. These results show the equibiaxial and non-equibiaxial strain path simulations nucleate more pores than the strip biaxial and uniaxial strain path simulations at considerably lower strains. In other words, the equibiaxial and non-equibiaxial strain path simulations nucleated a higher number of pores and did so faster. Along with this higher nucleation rate, pores grew faster during the equibiaxial and non-equibiaxial strain path simulations (Figure 2.5). However, despite the difference being not statistically significant according to the Tukey post hoc test, pore growth for the 4:1 non-equibiaxial strain path simulations were less than that observed for the equibiaxial and 2:1 non-equibiaxial strain path simulations, meaning a slightly increased failure strain would be expected.

Due to these pore nucleation and growth results, the equibiaxial and 2:1 non-equibiaxial strain path simulations resulted in the highest damage (Figure 2.6(A)) followed by the 4:1 non-equibiaxial and then strip biaxial strain path simulations. This

result follows from the pore nucleation and growth results, the product of which is damage [20]. Additionally, the phospholipid bilayer failed in the 4:1 non-equibiaxial strain path simulations shortly after the equibiaxial and 2:1 non-equibiaxial strain path simulations, as was expected due to the differences observed for pore growth. However, according to a Tukey post-hoc test, the difference in these failure strains were not statistically significant. As expected due to the lower pore nucleation and growth, the strip biaxial strain path simulations' failure strains were much greater. Despite the similarity in some of the strain path simulations, Figure 2.6(B) shows this damage at failure increased almost linearly as the strain state changed from strip biaxial to equibiaxial. Overall, these properties show the equibiaxial and 2:1 non-equibiaxial strain states resulted in a greater level of damage than the other strain states.

To summarize, several important points can be observed from this data. First, the equibiaxial and 2:1 non-equibiaxial strain path simulations nucleated pores at the highest rates. Further, pores grew faster during simulations for these two strain states. Second, deleterious mechanoporation and the associated damage occurred at much lower strains in the equibiaxial and 2:1 non-equibiaxial strain path simulations. These lower strains show that the phospholipids are able to rearrange the least during more equibiaxial strain states. Comparatively, the uniaxial strain state allows phospholipids to effectively rearrange, which delayed the growth of pores and effectively minimized the damage. However, while an unrestrained bilayer could potentially rearrange when pulled in only one direction, obstructions in a neuronal cell membrane would restrict phospholipid movements in a deformation scenario. In other words, a true uniaxial strain state would not be likely in a natural system at the nanoscale. Third, due to a lack of phospholipid

headgroup clustering, excitotoxic ions may enter pores more easily during more equibiaxial strain states due to ions being attracted to the more polarized clusters of phospholipid headgroups in other strain states. As a whole, the mechanoporation damage and phospholipid clustering suggest the equibiaxial and 2:1 non-equibiaxial strain states are the most detrimental strain states currently examined.

2.5.3 Membrane Failure Limit Diagram

The need for relating membrane damage directly to TBI provides a distinct challenge due to the difficulty of measuring damage *in vivo* and *in vitro*. As an alternative, *in silico* models can be used to quantify stress-strain and damage parameters, but these properties will be difficult to quantify in real-time experiments and may provide an undesirable conceptual battle for non-engineers. A simpler form of damage criteria is needed for this usage case. Hence, the forming limit diagram (FLD) tool has been adapted from the planar material of sheet metal to construct a Membrane Failure Limit Diagram (MFLD), which is given in Figure 2.7. The aim for this MFLD is to serve as a map for where injury will likely occur. To that end, multiple limits have been constructed related to both mechanical and physiological membrane phenomena. Specifically, limit lines for the yield, initial pore nucleation, first pore large enough for a water molecule, water penetration (failure), and the first pore large enough for a calcium ion with two hydrated shells are defined. These limits provide regions where the phospholipid bilayer can be considered safe or unsafe, which indicates if any events are physiologically detrimental to the neuron. The strain space where all pores are smaller than the water size threshold is considered to be safe because it is assumed the phospholipid bilayer integrity is maintained. Anything past water penetration is considered potentially unsafe because the

phospholipid bilayer has been compromised, which can lead to further damage—especially if membrane deformation continues. The strain space between the safe and failure zones is considered to be potentially hazardous because water may or may not penetrate both leaflets when pores are large enough to allow water passage. Additionally, the strain limit for the calcium ion penetration threshold shows that the potential for calcium ion penetration exists shortly after the penetration of water, a much smaller molecule, occurs. This finding is significant because it shows that calcium ion penetration is theoretically possible even for such a small system.

Another important finding Figure 2.7 shows is that, aside from yield, the strain values pertaining to pore nucleation and growth increased linearly from the equibiaxial to the uniaxial strain path simulations. This finding shows that it may be possible to develop a simple novel mechanistic equation that readily captures the strain threshold for neuronal membrane damage under diverse strain states. The change in behavior is linear, so the equation can be described using y - m*x = b, where m is slope, b is the y intercept, y is ε_{11} (x strain), and x is ε_{22} (y strain). The slopes are similar for the water size threshold, water penetration, and calcium ion size threshold lines, so a representative equation with a slope of -0.7 ± 5.4% and an intercept of 0.83, the intercept from the water size threshold line, gives a conservative estimate describing when cell membrane failure can occur. This gives Equation 2.1 for the orientation displayed in Figure 2.7.

$$\varepsilon_{11} + 0.7 * \varepsilon_{22} = 0.83 \quad (2.1)$$

Due to system symmetry, x and y (ε_{11} and ε_{22}) can be swapped, which would mirror the MFLD in Figure 2.7 along the equibiaxial line, to give Equation 2.2 for when right of the equibiaxial line.

$$\varepsilon_{11} + 1.4 * \varepsilon_{22} = 1.2 \quad (2.2)$$

By implementing the MFLD and developing a mechanistic equation, specified strains can be easily deemed safe or unsafe, allowing a simple way to determine potential neuronal damage in a multiscale modeling paradigm. This ease of observing and determining safe versus unsafe strain zones makes the MFLD a novel visual tool for exploring deformations of the phospholipid bilayer failure.

While the MFLD provides a simple novel way to analyze damage to the neuronal membrane, the current MFLD only provides a rough approximation of strains expected to result in injury. A more complex membrane will be implemented in future studies to better mimic the neuronal membrane structure, including additional phospholipid types and cholesterol, to more accurately capture the neuronal membrane's mechanical properties. Such a membrane will provide a more accurate representation of the neuron and be used to update the MFLD.

2.6 Conclusions

While mechanoporation has been observed to result in TBI [13], the underlying strains and limits for mechanoporation and the effect of strain state have not been previously quantified. The current study has quantified the nanoscale stress and mechanoporation damage behavior occurring in the neuronal membrane during TBI. These data will progress the current understanding of TBI at the nanoscale and aid to develop higher fidelity macroscale TBI constitutive models through mechano-physiological internal state variables (MPISVs). The major findings are as follows:

- The phospholipid bilayer stress behavior is strain state dependent with the equibiaxial having the highest stress followed by the 2:1 non-equibiaxial, 4:1 non-

equibiaxial, and strip biaxial strain states, where each has a progressively lower stress (Figure 2.2). The uniaxial strain state von Mises stress behavior is similar to that of the strip biaxial strain state, but the underlying component stresses are different.

- The difference in yield strain is not statistically significant when omitting the uniaxial strain state ($p = 0.2197$), so all non-uniaxial strain paths yielded at a similar strain level. Additionally, the difference in failure strain (water penetration) is strain state dependent ($p < 0.01$) with equibiaxial having the lowest failure strain (Figure 2.2, Table 2.2). However, three of the five strain path simulations (equibiaxial, 2:1 non-equibiaxial, and 4:1 non-equibiaxial) gave statistically insignificant failure strains.

- Simulations for the equibiaxial and 2:1 non-equibiaxial strain paths demonstrated the least phospholipid headgroup clustering during deformations (Figure 2.3(F)). Uniaxial strain path simulations clustered the phospholipid headgroups the most. Therefore, phospholipid headgroup clustering is a mechanism that induces localization in a deformed membrane that may allow assessing the localized strain state of a deformed membrane. Quantifying this mechanism to create a localization metric would allow experimentalists to determine any potential increased risk of cellular damage due to local strain states resulting from applied cellular loading.

- Damage from membrane mechanoporation, the product of pore nucleation and growth (Figure 2.4 and Figure 2.5), is strain state dependent with the equibiaxial and 2:1 non-equibiaxial strain path simulations resulting in the most damage

(Figure 2.6). Based on the above findings, the overall strain state order of detrimentality is equibiaxial, 2:1 non-equibiaxial, 4:1 non-equibiaxial, strip biaxial, and uniaxial, where equibiaxial and 2:1 non-equibiaxial strain states are the most detrimental and the uniaxial strain state is the least detrimental.

- The Membrane Failure Limit Diagram (MFLD) provides a simple novel way to illustrate the in-plane phospholipid bilayer deformations and the associated damage resulting from mechanoporation (Figure 2.7). At a given set of x and y strains representing any strain state, the MFLD clearly shows when the membrane's structural integrity is compromised, which can lead to catastrophic water tunneling, ion diffusion, loss of homeostasis, and cell death. The well-defined regions created allow for safe and unsafe deformations to be identified and representative equations to be defined. Equations 2.1 and 2.2 give a strain-based mechanistic description for the neuronal membrane failure based on damage analysis.

The findings presented herein will aid in the development of a more robust MPISV model required for higher fidelity models of TBI. However, additional membrane elements, such as other phospholipid types and cholesterol, are needed to develop molecular models that are more accurate and, ideally, tissue specific.

2.7 Acknowledgements

This material is based upon work supported by the Department of Agricultural and Biological Engineering and the Center for Advanced Vehicular Systems at Mississippi State University. Further, material presented in this paper is a product of the CREATE-GV Element of the Computational Research and Engineering Acquisition

Tools and Environments (CREATE) Program sponsored by the U.S. Department of Defense HPC Modernization Program Office. This effort was sponsored under contract number W912HZ-13-C-0037.

2.8 References

[1] M. Faul, L. Xu, M. M. Wald, and V. G. Coronado, "Traumatic Brain Injury in the United States: Emergency Department Visits, Hospitalizations, and Deaths 2002-2006," ed. Atlanta (GA): Centers for Disease Control Prevention, National Center for Injury Prevention and Control, 2010.

[2] I. Humphreys, R. L. Wood, C. J. Phillips, and S. Macey, "The costs of traumatic brain injury: a literature review," *ClinicoEconomics and outcomes research : CEOR,* vol. 5, pp. 281-7, 2013. doi: 10.2147/CEOR.S44625.

[3] A. A. Hyder, C. A. Wunderlich, P. Puvanachandra, G. Gururaj, and O. C. Kobusingye, "The impact of traumatic brain injuries: A global perspective," *NeuroRehabilitation,* vol. 22, 2007.

[4] A. M. Nahum, R. Smith, and C. C. Ward, "Intracranial Pressure Dynamics During Head Impact," 1977.

[5] X. Trosseille, C. Tarriere, and F. Lavaste, "Development of a F.E.M. of the Human Head According to a Specific Test Protocol," *Proceedings of the 30th Stapp Car Crash Conference,* pp. 235-253, 1992 1992.

[6] T. M. J. C. Andriessen, B. Jacobs, and P. E. Vos, "Clinical characteristics and pathophysiological mechanisms of focal and diffuse traumatic brain injury," *Journal of Cellular and Molecular Medicine,* vol. 14, pp. 2381-2392, 2010/10// 2010. doi: 10.1111/j.1582-4934.2010.01164.x.

[7] K. Miller, "Constitutive model of brain tissue suitable for finite element analysis of surgical procedures," *Journal of Biomechanics,* vol. 32, pp. 531-537, 1999/05// 1999. doi: 10.1016/S0021-9290(99)00010-X.

[8] K. K. Mendis, R. L. Stalnaker, and S. H. Advani, "A Constitutive Relationship for Large Deformation Finite Element Modeling of Brain Tissue," *Journal of Biomechanical Engineering,* vol. 117, pp. 279-285, 1995. doi: 10.1115/1.2794182.

[9] T. El Sayed, A. Mota, F. Fraternali, and M. Ortiz, "A variational constitutive model for soft biological tissues," *Journal of Biomechanics,* vol. 41, pp. 1458-1466, 2008 2008. doi: 10.1016/j.jbiomech.2008.02.023.

[10] R. Prabhu, M. F. Horstemeyer, M. T. Tucker, E. B. Marin, J. L. Bouvard, J. A. Sherburn*, et al.*, "Coupled experiment/finite element analysis on the mechanical response of porcine brain under high strain rates," *Journal of the Mechanical Behavior of Biomedical Materials,* vol. 4, pp. 1067-1080, 2011. doi: 10.1016/j.jmbbm.2011.03.015.

[11] B. Rashid, M. Destrade, and M. D. Gilchrist, "Mechanical characterization of brain tissue in tension at dynamic strain rates," *Forensic Biomechanics,* vol. 33, pp. 43-54, 2014/05// 2014. doi: 10.1016/j.jmbbm.2012.07.015.

[12] D. M. Geddes, R. S. Cargill, 2nd, and M. C. LaPlaca, "Mechanical stretch to neurons results in a strain rate and magnitude-dependent increase in plasma membrane permeability," *J Neurotrauma,* vol. 20, pp. 1039-49, Oct 2003. doi: 10.1089/089771503770195885.

[13] O. Farkas and J. T. Povlishock, "Cellular and subcellular change evoked by diffuse traumatic brain injury: a complex web of change extending far beyond focal damage," in *Progress in Brain Research*. vol. Volume 161, T. W. John and I. R. M. Andrew, Eds., ed: Elsevier, 2007, pp. 43-59.

[14] A. Kampfl, R. Posmantur, R. Nixon, F. Grynspan, X. Zhao, S. J. Liu*, et al.*, "μ-Calpain Activation and Calpain-Mediated Cytoskeletal Proteolysis Following Traumatic Brain Injury," *Journal of Neurochemistry,* vol. 67, pp. 1575-1583, 1996/10/01/ 1996. doi: 10.1046/j.1471-4159.1996.67041575.x.

[15] B. J. Gwag, L. M. T. Canzoniero, S. L. Sensi, J. A. DeMaro, J. Y. Koh, M. P. Goldberg*, et al.*, "Calcium ionophores can induce either apoptosis or necrosis in cultured cortical neurons," *Neuroscience,* vol. 90, pp. 1339-1348, 1999/06// 1999. doi: 10.1016/S0306-4522(98)00508-9.

[16] M. Terasaki, K. Miyake, and P. L. McNeil, "Large Plasma Membrane Disruptions Are Rapidly Resealed by Ca2+-dependent Vesicle–Vesicle Fusion Events," *The Journal of Cell Biology,* vol. 139, pp. 63-74, 1997/10/06/ 1997.

[17] S. T. Cooper and P. L. McNeil, "Membrane Repair: Mechanisms and Pathophysiology," *Physiological Reviews,* vol. 95, pp. 1205-1240, 2015/10/01/ 2015. doi: 10.1152/physrev.00037.2014.

[18] A. L. Gurson, "Continuum Theory of Ductile Rupture by Void Nucleation and Growth: Part I—Yield Criteria and Flow Rules for Porous Ductile Media," *Journal of Engineering Materials and Technology,* vol. 99, pp. 2-15, 1977/01/01/ 1977. doi: 10.1115/1.3443401.

[19] M. F. Horstemeyer and A. M. Gokhale, "A void–crack nucleation model for ductile metals," *International Journal of Solids and Structures,* vol. 36, pp. 5029-5055, 11// 1999. doi: 10.1016/S0020-7683(98)00239-X.

[20] M. F. Horstemeyer, J. Lathrop, A. M. Gokhale, and M. Dighe, "Modeling stress state dependent damage evolution in a cast Al–Si–Mg aluminum alloy," *Theoretical and Applied Fracture Mechanics,* vol. 33, pp. 31-47, 2// 2000. doi: 10.1016/S0167-8442(99)00049-X.

[21] M. A. Murphy, M. F. Horstemeyer, S. R. Gwaltney, T. Stone, M. LaPlaca, J. Liao*, et al.*, "Nanomechanics of phospholipid bilayer failure under strip biaxial stretching using molecular dynamics," *Modelling and Simulation in Materials Science and Engineering,* vol. 24, p. 055008, 2016. doi: 10.1088/0965-0393/24/5/055008.

[22] J. L. Bouvard, D. K. Ward, D. Hossain, E. B. Marin, D. J. Bammann, and M. F. Horstemeyer, "A general inelastic internal state variable model for amorphous glassy polymers," *Acta Mechanica,* vol. 213, pp. 71-96, 2010. doi: 10.1007/s00707-010-0349-y.

[23] M. F. Horstemeyer and D. J. Bammann, "Historical review of internal state variable theory for inelasticity," *Special Issue In Honor of David L. McDowell,* vol. 26, pp. 1310-1334, 2010/09// 2010. doi: 10.1016/j.ijplas.2010.06.005.

[24] D. K. Cullen, C. M. Simon, and M. C. LaPlaca, "Strain rate-dependent induction of reactive astrogliosis and cell death in three-dimensional neuronal–astrocytic co-cultures," *Brain Research,* vol. 1158, pp. 103-115, 7/16/ 2007. doi: 10.1016/j.brainres.2007.04.070.

[25] K. Koshiyama and S. Wada, "Molecular dynamics simulations of pore formation dynamics during the rupture process of a phospholipid bilayer caused by high-speed equibiaxial stretching," *Journal of Biomechanics,* vol. 44, pp. 2053-8, 2011/07/28/ 2011. doi: 10.1016/j.jbiomech.2011.05.014.

[26] B. Rashid, M. Destrade, and M. D. Gilchrist, "Mechanical characterization of brain tissue in compression at dynamic strain rates," *Journal of the Mechanical Behavior of Biomedical Materials,* vol. 10, pp. 23-38, 2012/06// 2012. doi: 10.1016/j.jmbbm.2012.01.022.

[27] B. Rashid, M. Destrade, and M. D. Gilchrist, "Mechanical characterization of brain tissue in simple shear at dynamic strain rates," *Journal of the Mechanical Behavior of Biomedical Materials,* vol. 28, pp. 71-85, 2013/12// 2013. doi: 10.1016/j.jmbbm.2013.07.017.

[28] M. LaPlaca and L. Thibault, "Anin vitro traumatic injury model to examine the response of neurons to a hydrodynamically-induced deformation," *Annals of Biomedical Engineering,* vol. 25, pp. 665-677, 1997/07/01 1997. doi: 10.1007/BF02684844.

[29] M. C. LaPlaca, D. K. Cullen, J. J. McLoughlin, and R. S. Cargill Ii, "High rate shear strain of three-dimensional neural cell cultures: a new in vitro traumatic brain injury model," *Journal of Biomechanics,* vol. 38, pp. 1093-1105, 2005/05// 2005. doi: 10.1016/j.jbiomech.2004.05.032.

[30] M. C. LaPlaca and G. R. Prado, "Neural mechanobiology and neuronal vulnerability to traumatic loading," *Journal of Biomechanics,* vol. 43, pp. 71-78, 1/5/ 2010. doi: 10.1016/j.jbiomech.2009.09.011.

[31] D. K. Cullen, V. N. Vernekar, and M. C. LaPlaca, "Trauma-Induced Plasmalemma Disruptions in Three-Dimensional Neural Cultures Are Dependent on Strain Modality and Rate," *Journal of Neurotrauma,* vol. 28, pp. 2219-2233, 2011/11/01 2011. doi: 10.1089/neu.2011.1841.

[32] R. M. Hochmuth, "Micropipette aspiration of living cells," *Journal of Biomechanics,* vol. 33, pp. 15-22, 2000/01// 2000.

[33] W. Rawicz, B. A. Smith, T. J. McIntosh, S. A. Simon, and E. Evans, "Elasticity, Strength, and Water Permeability of Bilayers that Contain Raft Microdomain-Forming Lipids," *Biophysical Journal,* vol. 94, pp. 4725-4736, 2008/06/15/ 2008. doi: 10.1529/biophysj.107.121731.

[34] E. Ovalle-García, J. J. Torres-Heredia, A. Antillón, and I. Ortega-Blake, "Simultaneous Determination of the Elastic Properties of the Lipid Bilayer by Atomic Force Microscopy: Bending, Tension, and Adhesion," *The Journal of Physical Chemistry B,* vol. 115, pp. 4826-4833, 2011/04/28/ 2011. doi: 10.1021/jp111985z.

[35] E. Evans, V. Heinrich, F. Ludwig, and W. Rawicz, "Dynamic tension spectroscopy and strength of biomembranes," *Biophys J,* vol. 85, pp. 2342-50, Oct 2003. doi: 10.1016/S0006-3495(03)74658-X.

[36] D. Needham and R. S. Nunn, "Elastic deformation and failure of lipid bilayer membranes containing cholesterol," *Biophysical Journal,* vol. 58, pp. 997-1009, 10// 1990. doi: 10.1016/S0006-3495(90)82444-9.

[37] H. Leontiadou, A. E. Mark, and S. J. Marrink, "Molecular dynamics simulations of hydrophilic pores in lipid bilayers," *Biophys J,* vol. 86, pp. 2156-64, Apr 2004. doi: 10.1016/S0006-3495(04)74275-7.

[38] D. P. Tieleman, H. Leontiadou, A. E. Mark, and S. J. Marrink, "Simulation of pore formation in lipid bilayers by mechanical stress and electric fields," *J Am Chem Soc,* vol. 125, pp. 6382-3, May 28 2003. doi: 10.1021/ja029504i.

[39] M. D. Tomasini, C. Rinaldi, and M. S. Tomassone, "Molecular dynamics simulations of rupture in lipid bilayers," *Experimental Biology and Medicine (Maywood, N.J.),* vol. 235, pp. 181-8, Feb 2010. doi: 10.1258/ebm.2009.009187.

[40] T. Shigematsu, K. Koshiyama, and S. Wada, "Effects of Stretching Speed on Mechanical Rupture of Phospholipid/Cholesterol Bilayers: Molecular Dynamics Simulation," *Scientific Reports,* vol. 5, p. 15369, 10/16/online 2015. doi: 10.1038/srep15369.

[41] T. Shigematsu, K. Koshiyama, and S. Wada, "Molecular dynamics simulations of pore formation in stretched phospholipid/cholesterol bilayers," *Chemistry and Physics of Lipids,* vol. 183, pp. 43-49, 10// 2014. doi: 10.1016/j.chemphyslip.2014.05.005.

[42] J. B. Klauda, R. M. Venable, J. A. Freites, J. W. O'Connor, D. J. Tobias, C. Mondragon-Ramirez*, et al.*, "Update of the CHARMM All-Atom Additive Force Field for Lipids: Validation on Six Lipid Types," *Journal of Physical Chemistry B,* vol. 114, pp. 7830-7843, 2010/06/17 2010. doi: 10.1021/jp101759q.

[43] S. Plimpton, "Fast Parallel Algorithms for Short-Range Molecular Dynamics," *Journal of Computational Physics,* vol. 117, pp. 1-19, 3/1/ 1995. doi: 10.1006/jcph.1995.1039.

[44] A. Stukowski, "Visualization and analysis of atomistic simulation data with OVITO–the Open Visualization Tool," *Modelling and Simulation in Materials Science and Engineering,* vol. 18, p. 015012, 2010.

[45] A. Bondi, "van der Waals Volumes and Radii," *The Journal of Physical Chemistry,* vol. 68, pp. 441-451, 1964/03/01 1964. doi: 10.1021/j100785a001.

[46] *MATLAB and Image Processing Toolbox Release 2013a, The MathWorks Inc., Natick, MA, 2013.*

[47] A. H. Narten and H. A. Levy, "Liquid Water: Molecular Correlation Functions from X-Ray Diffraction," *The Journal of Chemical Physics,* vol. 55, pp. 2263-2269, 1971. doi: 10.1063/1.1676403.

[48] C. F. Schwenk and B. M. Rode, "Ab initio QM/MM MD simulations of the hydrated Ca2+ ion," *Pure and applied chemistry,* vol. 76, pp. 37-47, 2004.

[49] S. P. Keeler and W. A. Backofen, "Plastic Instability and Fracture in Sheets Stretched Over Rigid Punches," *Transactions of the American Society of Metals Quarterly,* vol. 56, pp. 25-48, 1963.

[50] M. Safari, S. J. Hosseinipour, and H. D. Azodi, "Experimental and Numerical Analysis of Forming Limit Diagram (FLD) and Forming Limit Stress Diagram (FLSD)," *Materials Sciences and Applications,* vol. 02, pp. 496-502, 2011. doi: 10.4236/msa.2011.25067.

[51] M. F. Horstemeyer, "A Numerical Parametric Investigation of Localization and Forming Limits," *International Journal of Damage Mechanics,* vol. 9, pp. 255-285, 2000. doi: doi:10.1177/105678950000900304.

[52] T. V. Tolpekina, W. K. den Otter, and W. J. Briels, "Simulations of stable pores in membranes: system size dependence and line tension," *J Chem Phys,* vol. 121, pp. 8014-20, Oct 22 2004. doi: 10.1063/1.1796254.

[53] NOCSAE, "Standard Performance Specification for Newly Manufactured Football Helmets," NOCSAE DOC (ND)002-13m13, December 2013.

[54] M. T. Begonia, R. Prabhu, J. Liao, W. R. Whittington, A. Claude, B. Willeford, *et al.*, "Quantitative analysis of brain microstructure following mild blunt and blast trauma," *Journal of Biomechanics,* vol. 47, pp. 3704-3711, 11/28/ 2014. doi: 10.1016/j.jbiomech.2014.09.026.

[55] J. C. M. Lee, M. Santore, F. S. Bates, and D. E. Discher, "From Membranes to Melts, Rouse to Reptation: Diffusion in Polymersome versus Lipid Bilayers," *Macromolecules,* vol. 35, pp. 323-326, 2002/01/01 2002. doi: 10.1021/ma0112063.

[56] P. J. Clark and F. C. Evans, "Distance to Nearest Neighbor as a Measure of Spatial Relationships in Populations," *Ecology,* vol. 35, pp. 445-453, 1954. doi: 10.2307/1931034.

CHAPTER III

NANOMECHANICS OF PHOSPHOLIPID BILAYER FAILURE UNDER STRIP BIAXIAL STRETCHING USING MOLECULAR DYNAMICS

Previously published, M. A. Murphy, M. F. Horstemeyer, S. R. Gwaltney, T. Stone, M. LaPlaca, J. Liao, et al., "Nanomechanics of phospholipid bilayer failure under strip biaxial stretching using molecular dynamics," Modelling and Simulation in Materials Science and Engineering, vol. 24, p. 055008, 2016. doi: 10.1088/0965-0393/24/5/055008.

3.1 Introduction

Traumatic brain injury (TBI) has become a great concern with approximately 1.7 million new cases every year in the United States alone, resulting in both human and economic losses [1]. TBI arises because of complex deleterious interactions operating at different length scales. By implementing continuum constitutive models into finite element analysis researchers have attempted to better replicate the brain's morphology and stress responses under TBI scenarios [2-6]. However, the macroscale continuum theory does not currently have local damage related to neuron death. Damage is defined as the pore volume fraction in the macroscale continuum, which is multiplicatively decomposed into Mechano-Physiological Internal State Variables (MPISVs) for pore number density (related to nucleation), pore growth (related to size), and pore coalescence (related to nearest neighbor distance). The mathematical equations for the macroscale MPISVs are currently unknown for the brain material. In this context, Figure 3.1 illustrates our multiscale hierarchical paradigm for the mechanical deformation of the

brain during a TBI event. Under this hierarchical paradigm (Figure 3.1) relevant microstructural information are obtained from the Molecular Dynamics (MD) simulations of the mechanoporation of a neuronal lipid bilayer. As Bridge 6 in Figure 3.1 illustrates, identifying the local mechanisms and quantifying the pore nucleation, pore growth, and pore coalescence values in a phospholipid bilayer under large deformations are key to understanding TBI at the macroscale. Macroscale physics-based constitutive models with MPISVs allow one to implicitly introduce lower length scale effects in the continuum like the damage related to neuron death as well as predicting history effects, physiological changes, and microstructural changes. Hence, the MPISVs require subscale information, from MD simulations, to better define when a physical insult (an event that results in injury) occurs and to understand the strain rate and stress state relations for relevant biological microstructures. Experimental studies have shown that membrane mechanoporation (creation of pores due to a mechanical insult) increases membrane permeability post-injury and leads to TBI [7-9]. This penetration can disrupt normal cell functions, potentially leading to necrosis or apoptosis [10]. Because the phospholipid bilayer provides extensive protective functions as part of the neuronal cell membrane, a better understanding of bilayer mechanoporation is critical to understanding mechanical injuries to neurons and, as such, the human brain.

Previous *in vitro* studies of phospholipid bilayer deformations have investigated mechanical properties, such as rupture strength and elastic constants, via micropipette aspiration [11-13]. This method enabled experimental examination of pore nucleation, but controlling deformations with in-plane stresses restricted the ability to control the deformation rates. These experiments did show, however, that phospholipid bilayer

rupture is rate dependent [11] and stiffened by cholesterol [13]. Despite these experimental studies, many mechanical properties of the phospholipid bilayer and their immediate physical reactions to deformations require *in silico* atomic-level simulations. Molecular dynamics (MD) simulations can be used to represent and interpret the mechano-physiological phenomena of mechanoporation that occur at the nanoscale and give a more robust microstructure-based structure-property correlation of TBI at lower length scales. This robust model of TBI will aid in determining structural failure and, ultimately, bodily injury.

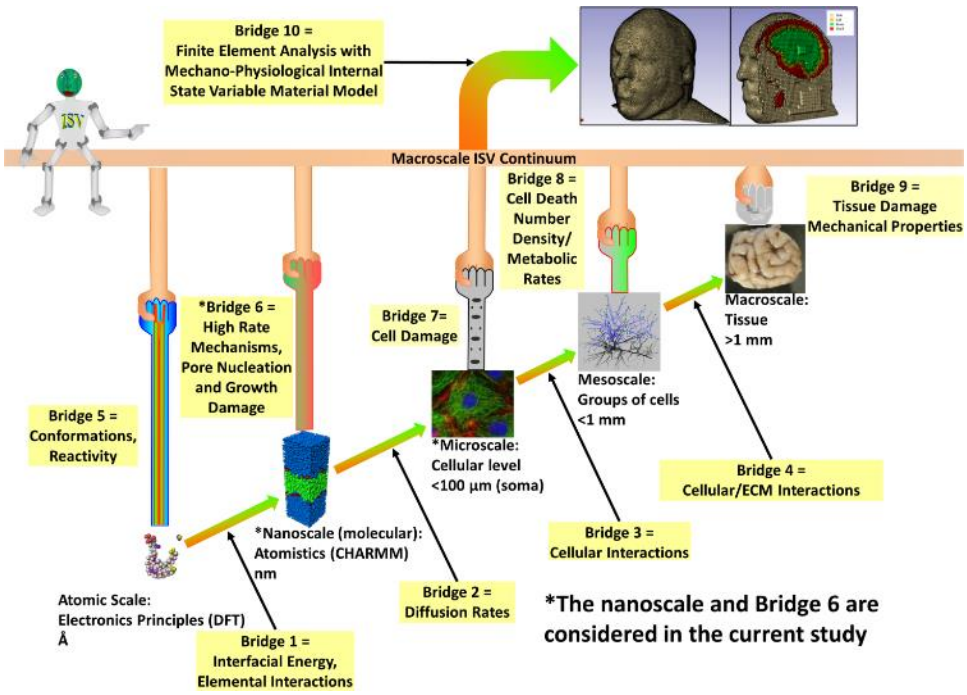

Figure 3.1 Overview of the multiscale modelling hierarchy displaying the principle of a physics-based constitutive model for TBI.

More recently, *in silico* studies have been revealed aspects of phospholipid bilayer deformations and pore nucleation [14-18]. Some of these studies deformed the bilayer

using in-plane lateral stresses (pressures) and showed that higher applied in-plane stresses led to phospholipid bilayer thinning, mechanoporation, and destabilization [14, 15]. Additionally, stable pores were possible under low in-plane stresses [15]. However, deformations using applied in-plane stresses can artificially tear the bilayer apart due to barostat feedback rather than pore nucleation [16]. Alternative methods of deforming the phospholipid bilayer have also been implemented, such as simulation box stretching [16], incremental tensile and in-plane shear stretching [17], or unsteady tensile stretching [18]. Studies that used phospholipid bilayer stretching with relaxation periods did not represent a continuous deformation and used volume conservation to control the perpendicular dimension [16, 17]. Instead, unsteady stretching better represented continuous deformations and allowed the perpendicular dimension to relax simultaneously [18]. With continuous deformation, the phospholipid bilayer nucleated pores without partially recovering between deformations.

A comprehensive analysis of the diverse strain rate and strain state boundary conditions on phospholipid bilayer's inelastic behavior needs quantification in order to understand the neuronal phospholipid bilayer mechanoporation for the development of a physics-based multiscale constitutive model for TBI. In this study, the authors use MD to examine the effect of strain rate on the von Mises (equivalent) stress during strip biaxial tensile deformations of the phospholipid bilayer and show that the results for a smaller structure are equivalent to those of a larger structure. Damage-related properties related to the bridging of length scales for mechanoporation, that is, pore area fraction, pore number density, and average nearest neighbor's distance (NND), have been quantified for the first time to give a better understanding of mechanoporation during TBI.

3.2 Methods

3.2.1 System Equilibration

A 1-palmitoyl-2-oleoylphosphatidylcholine (POPC) phospholipid bilayer was used as a representative structure for a neuronal cell membrane. Atomic coordinates for a pre-equilibrated phospholipid bilayer were obtained from the website of the Laboratory of Computational Biology: Membrane Biophysics Section based on the works of Klauda and others [19]. The obtained phospholipid bilayer structure contained 72 phospholipids and 2,242 TIP3P water molecules. The molecular dynamics simulator LAMMPS (http://lammps.sandia.gov) [20] paired with the CHARMM36 all-atom lipid [19, 21] force field was used for all simulations. Water molecules were added to the top and bottom of the bilayer structure to limit interactions between the periodic images during deformations, resulting in a total of 9,070 water molecules.

The temperature for the structure was chosen to be 310 K to replicate the natural human body temperature. The simulation temperature was ramped to 310 K using the NVT (canonical: constant number of particles, volume, and temperature) ensemble. The NPT (isothermal-isobaric: constant number of particles, pressure, and temperature) ensemble was used to allow the simulation box to equilibrate under a pressure of 1 atm in all principal dimensions (controlled independently), resulting in a total of 5 ns of equilibration. Thermostatting and barostatting were performed using Nose-Hoover style equations [22] with a thermostat constant of 100 fs. The barostat constant was 500 fs and consistent with previous literature [18]. All simulations were performed in an orthogonal simulation box using periodic boundary conditions and a particle-particle particle-mesh (PPPM) solver grid of 1×10^{-5} Å with analytical differentiation, which was updated every

500 fs. A 0.5 fs timestep with the verlet integrator was used as recommended for systems with flexible molecules and bonds [23]. The neighbor list was checked every step and updated if any atoms had moved more than 1 Å. Additionally, Lennard-Jones and Coulombic interactions were given an inner cutoff radius of 10 Å.

The structure with water was then replicated by a factor of two in the x dimension to create a phospholipid bilayer structure that had dimensions of approximately ten by five nanometers. Both structures were further equilibrated for an additional 5 ns, resulting in area per phospholipid values of 0.63 and 0.60 nm^2/lipid for the structures with 72 and 144 phospholipids, respectively. Figure 3.2 shows a comparison of phospholipid bilayer structures.

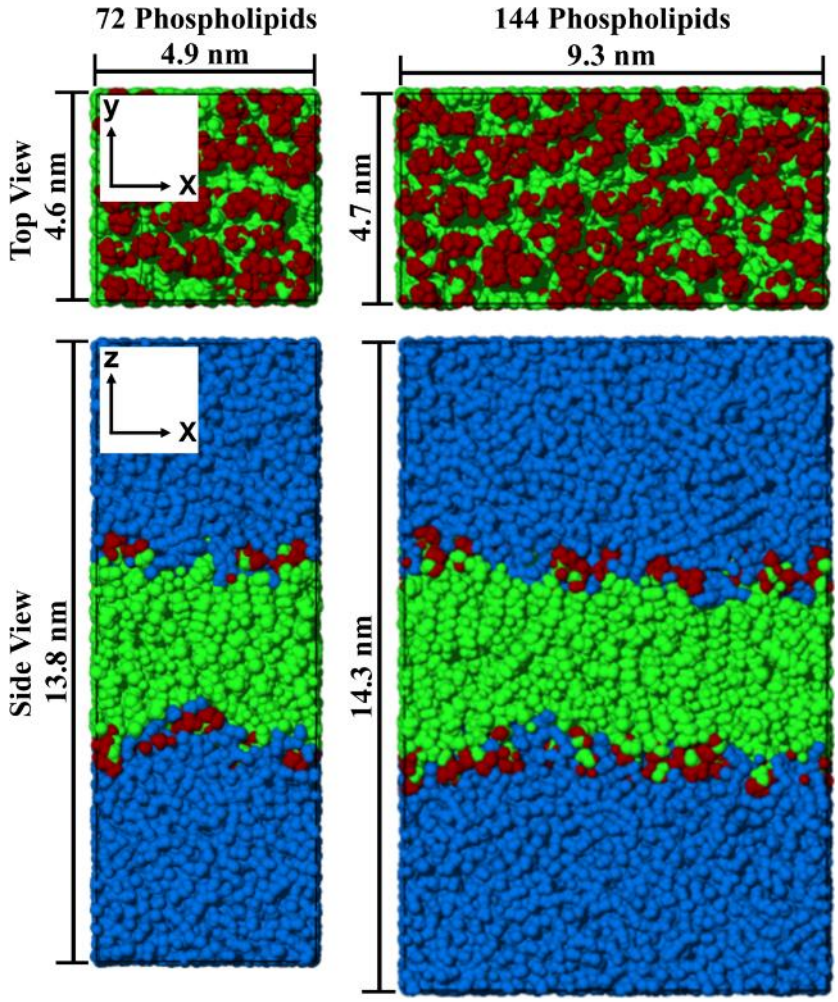

Figure 3.2 Top view and side view size comparisons of the equilibrated phospholipid bilayer structures displaying the differences between the 72 phospholipid structure with water displayed (left) and 144 phospholipid structure with water visually hidden (right).

Blue is water, phospholipid headgroups are red, and phospholipid tails are green.

3.2.2 Deformation Simulations

Large deformations were applied to the computational specimens by increasing the simulation box length in the x and y dimensions at defined velocities to maintain constant engineering strain rate deformations. Specifically, each specimen was deformed at constant velocity in the *x* dimension while the *y* dimension was held constant.

Phospholipids and water were allowed to respond to the box freely and flowed into the expanding box as it expanded. Additionally, one deformation case for the larger specimen held the x dimension constant while the y dimension was deformed. These deformations created a state of strip biaxial tension as shown in Figure 3.3 (A) and continued until well past failure. No specific stopping point was defined, allowing examination of pore nucleation, growth, and coalescence. Table 3.1 shows a summary of the deformation simulation parameters.

Deformation velocities were determined using identical strain rates for both bilayer systems. The *z* dimension was allowed to adjust freely while being subjected to a pressure of 1 atm and a temperature of 310 K for all cases. Thermostatting and barostatting time constants for the z dimension as well as non-deformation parameters remained the same as during equilibration simulations. There was no net change in temperature during deformations with the magnitude of the average temperature fluctuations being less than 0.2 K. In addition, to verify no significant effect due to the equilibrated structure, the 72 phospholipid structure was equilibrated twice more using different initial velocities. The resulting structures were deformed at the strain rates seen in Table 3.1 for the 72x1, 72x2, 72x3, and 72x5 cases and provided similar results. A separate simulation was also run with a 0.25 fs timestep to verify a 0.5 fs timestep was adequate.

The structure was visualized using the program OVITO [24] with an atomic radii of 1.2 Å employed. Structure failure was determined by hiding all phospholipids to observe water penetration into the hydrophobic region of the phospholipid bilayer, as

shown in Figure 3.3 (B). Formation of a water bridge, following penetration through both the top and bottom phospholipid leaflets, constituted failure of the structure.

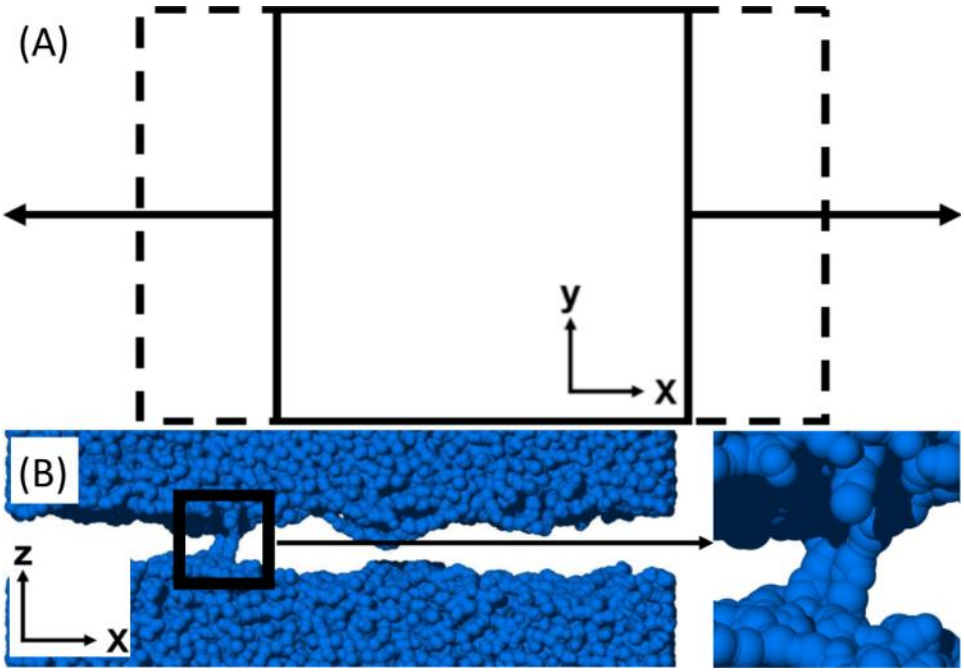

Figure 3.3 (A) Representative perpendicular (top) schematic of the deformations performed.

The original structure is represented by a solid black line and the deformed structure by a dashed line. (B) Side view of the phospholipid bilayer with all phospholipids visually removed for the 72x1 case. The water bridge has just connected and is enlarged to the right.

Table 3.1 Summary of Deformation Simulations

Case Name	Number of Phospholipids	$\dot{\varepsilon}$ (s^{-1})	$\dot{\varepsilon}_{VM}$ (s^{-1})	Deformation Rate ($m \cdot s^{-1}$)
72x1	72	2.0×10^8	1.4×10^8	1.0
72x2	72	4.1×10^8	2.7×10^8	2.0
72x3	72	6.1×10^8	4.1×10^8	3.0
72x5	72	1.0×10^9	6.8×10^8	5.0
144x1.9	144	2.0×10^8	1.4×10^8	1.9
144x3.8	144	4.1×10^8	2.7×10^8	3.8
144x5.7	144	6.1×10^8	4.1×10^8	5.7
144x9.5	144	1.0×10^9	6.8×10^8	9.5
144y4.8	144	1.0×10^9	6.8×10^8	4.8

3.2.3 Analysis Methods

3.2.3.1 Qualitative Image Analysis

OVITO [24] was used to render images every 5 ps. The OpenGL renderer with an antialiasing value of 6 was used while rendering. All water molecules were visually hidden, and phospholipid atoms were colored black on a white background so that pores appeared as white gaps between phospholipids. The images were imported into the image analysis software ImageJ [25] for analysis of two different pore sizes: those with areas greater than 0.0 nm^2 and for pores with areas greater than 0.1 nm^2, which is large enough for a water molecule to penetrate based on a calculated circular area of ~0.07 nm^2 ($d \approx$ 0.3 nm [26]). The following pore properties were calculated from each image using an in-house MATLAB [27] code: pore number density (pores/nm^2), percent area fraction, and mean nearest neighbor distance (nm). The pore number density is the number of pores per nm^2; the percent area fraction is the ratio of pore area to the total bilayer area, and the mean nearest neighbor distance is the average distance between each pore and the nearest neighboring pore. All objects reported by ImageJ were treated as unique pores. Thus,

counting partial pores crossing a periodic boundary led to a higher pore count than actually present. Please also see the tutorial Particle Characterization with ImageJ: https://icme.hpc.msstate.edu/mediawiki/index.php/Particle_Characterization_with_ImageJ).

3.2.4 Quantitative Analysis

Deformations in the current study are biaxial in nature and have significant stress responses for the in-plane dimensions. Therefore, measuring the stress for the phospholipid bilayer requires the use of an equivalent stress. Typically, surface tension is used as a planar equivalent stress but requires both the principle stresses and the bilayer height. As an alternative, the von Mises stress provides a method to view the equivalent stress on the system without measuring the bilayer height. Ergo, the equivalent von Mises stress paired with von Mises strain was used for quantifying the response to deformations. As expected of a fluid, the observed shear stresses were not affected by deformations and assumed to be numerical noise, so the von Mises stress equation was effectively $\sigma_{VM} = (1/2 * [(\sigma_x - \sigma_y)^2 + (\sigma_y - \sigma_z)^2 + (\sigma_x - \sigma_z)^2])^{0.5}$, where σ_{VM} is the equivalent von Mises stress and σ_x, σ_y, and σ_z are the principal pressures (stresses) averaged for all atoms during the simulation. Similarly, the simulation box was orthogonal, so the von Mises strain was calculated as $\varepsilon_{VM} = (2/9 * [(\varepsilon_x - \varepsilon_y)^2 + (\varepsilon_x)^2 + (\varepsilon_y)^2])^{0.5}$ where ε_{VM} is the equivalent von Mises strain and ε_x, ε_y are the principal true strains. ε_z was omitted because the dimension was not controlled. The yield stress and strain were determined as the initial peak stress with its corresponding strain, respectively. Due to the stress peaking and then decreasing in higher rate cases, the magnitude of the yield stress was often close to that of the maximum stress.

The surface tension was calculated, for use when calibrating to an empirical model, using the equation: $\gamma = (\sigma_z - (\sigma_x + \sigma_y)/2) * l_z$, where γ is surface tension and l_z is the phospholipid bilayer height approximated linearly from the initial bilayer height with a 15 Å layer of water (~60 Å total) to the final recorded box height, which corresponded to the bilayer height with a layer of water approximately 15 Å thick. As such, we use the approximated height and not the box height, which is necessary because the surface tension equation is only applicable to the area concerning the interface [28]. If the full box height were used to calculate the surface tension, surface tension results would be less accurate. Additional details and justifications for surface tension calculations using the height approximation are found in APPENDIX B. All quantitative data processing was performed using the commercial software package MATLAB [27].

3.3 Results

3.3.1 Pore Nucleation and Growth

Deformations from the strip biaxial tensile simulation quickly resulted in pore nucleation and thinning of the bilayer structure. As the structure experienced more deformation, larger gaps between the phospholipid heads developed, allowing chains of water to penetrate into the hydrophobic region. This continued until chains of water molecules from both sides connected as shown in Figure 3.3 (B). Figure 3.4 shows the typical progression from initial structure to multiple fully penetrated pores.

The simulations showed no correlation between strain rate or bilayer area when comparing the strain level between the appearance of the first and the second pores that exhibited full water penetration. At the lowest strain rate ($\dot{\varepsilon}_{VM} = 1.4 \times 10^8\ s^{-1}$), the structures developed a single large, circular pore that grew, while subsequent locations of

water penetration initially did not expand. At higher strain rates ($\dot{\varepsilon}_{VM} = 2.7 \times 10^8$ s^{-1}, 4.1×10^8 s^{-1}, and 6.8×10^8 s^{-1}), the structures typically developed multiple large pores that were similar in area with less circularity. Figure 3.5 shows a comparison of the pore growth paths for the 1.4×10^8 s^{-1} and 2.7×10^8 s^{-1} von Mises strain rates. However, there was no relation between the strain rate and the mean pore areas when compared at the same strains.

Table 3.2 summarizes the yield stress and strains, the first detectable pore greater than 0.0 nm^2, the first detectable pore greater than 0.1 nm^2, and failure. The maximum surface tension values were also included for reference.

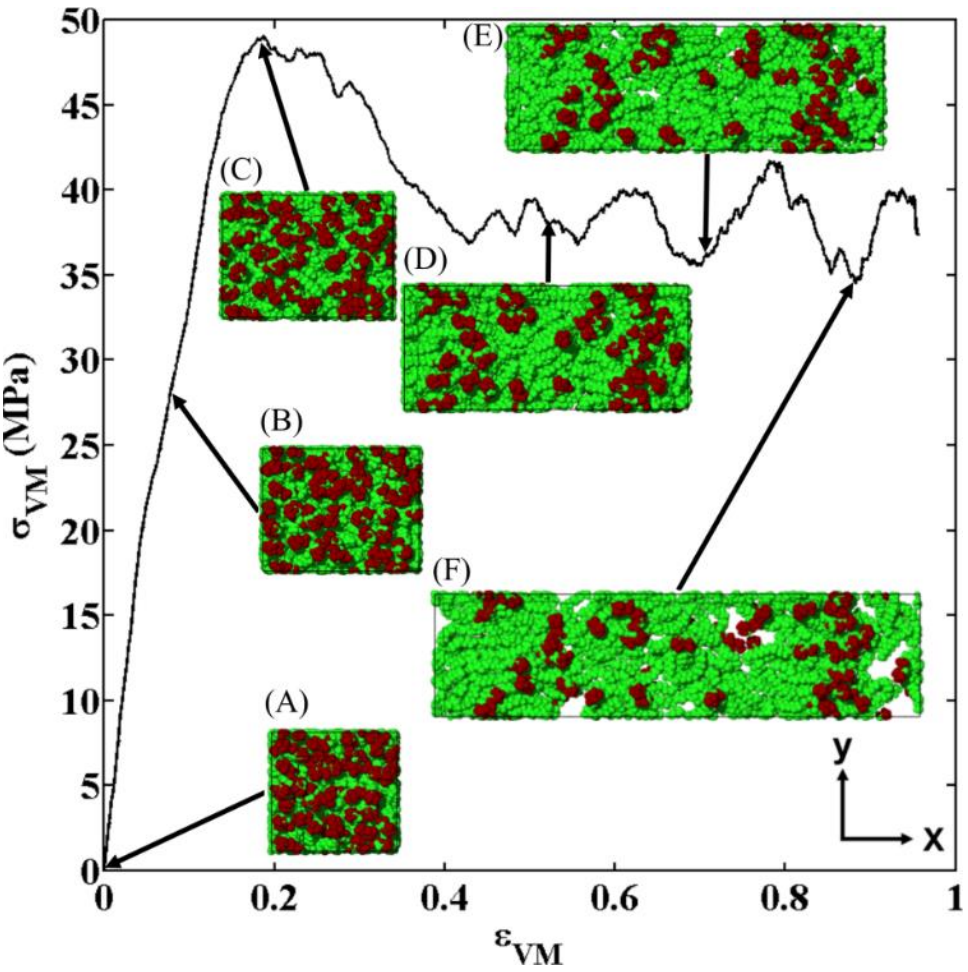

Figure 3.4 Von Mises stress-strain curve for the 4.1×10^8 s^{-1} von Mises strain rate.

Snapshots of the top view of the phospholipid bilayer (water visually removed) show the phospholipid bilayer at the (A) initial structure, (B) first detected pore, (C) first peak stress, (D) first detected pore larger than 0.1 nm^2, (E) initial full water penetration, and (F) multiple fully penetrating pores. Each color represents a different atom type. Hydrogen atoms surrounding the phospholipid head group are colored red (dark grey in greyscale).

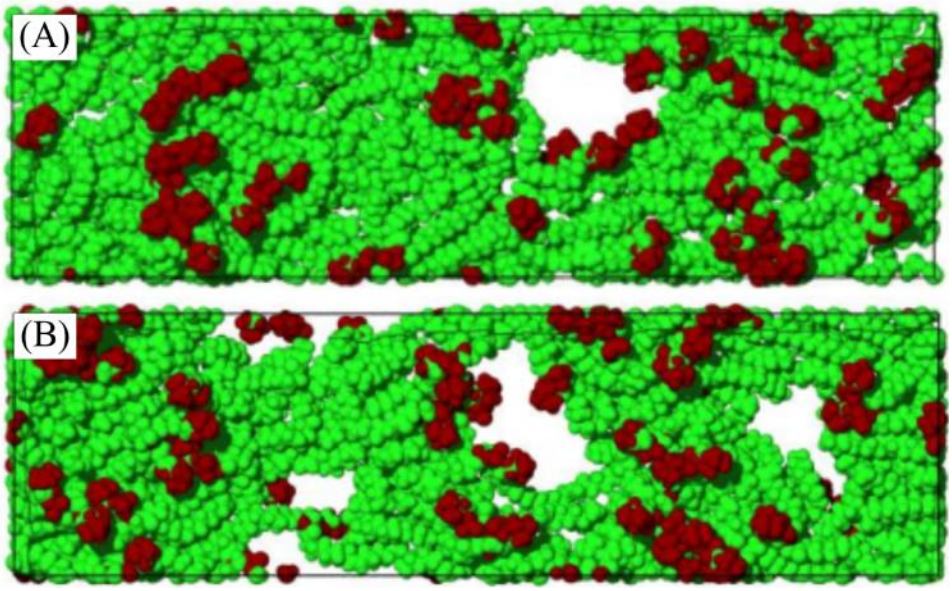

Figure 3.5 Pores at a von Mises strain of 0.8 for the von Mises strain rates (A) 1.4×10^8 s^{-1} and (B) 2.7×10^8 s^{-1} for the 72 phospholipid bilayer.

Each color represents a different atom type. Hydrogen atoms surrounding the phospholipid head group are colored red (dark grey in greyscale).

Table 3.2 Mechanical Properties of the Phospholipid Bilayer Under Strip Biaxial Tension at Different Strain Rates and Numbers of Phospholipids

Case Name	$\dot{\varepsilon}_{VM}$ (s^{-1})	σ^{VM}_{Yield} (MPa)	γ_{Yield} ($mN \cdot m^{-1}$)	ε^{VM}_{Yield}	$\varepsilon^{VM}_{FirstPore}$	$\varepsilon^{VM}_{FirstPore}$ ≥ 0.1 nm^2	$\varepsilon^{VM}_{Failure}$
72x1	1.4×10^8	26.6	137.6	0.057	0.079	0.529	0.721
72x2	2.7×10^8	42.7	226.7	0.117	0.127	0.430	0.615
72x3	4.1×10^8	48.9	235.1	0.180	0.126	0.516	0.703
72x5	6.8×10^8	64.4	309.6	0.225	0.197	0.526	0.687
144x1.9	1.4×10^8	26.5	131.9	0.056	0.151	0.460	0.691
144x3.8	2.7×10^8	41.3	203.2	0.120	0.233	0.548	0.649
144x5.7	4.1×10^8	53.9	262.7	0.160	0.126	0.535	0.653
144x9.5	6.8×10^8	66.7	304.7	0.225	0.275	0.553	0.715
144y4.8	6.8×10^8	64.3	310.2	0.226	0.231	0.486	0.684

Figure 3.6 and Figure 3.7 show the results for the pore area fraction and pore number density for all pores greater than 0.0 nm^2 and for only pores greater than 0.1 nm^2 and include vertical lines indicating water penetration for each case. Initially, no pores

are present in the structure. After pores began appearing, they continued to increase as indicated by the continually increasing pore area fraction in Figure 3.6 and number density curves in Figure 3.7. The pore number density for all pores is much greater than the pore number density for pores with areas larger than 0.1 nm^2. However, the difference in area fraction between all pores and pores with areas larger than 0.1 nm^2 is much smaller. Therefore, the pore area for the large pores constitutes the majority of the pore area detected. When considering all pores, the pore number density values for the 144 phospholipid bilayer are considerably smaller than the values for the 72 phospholipid bilayer, but the pore number density curves are similar for all rates and bilayer structures tested in the current study. Additionally, the pore number density magnitudes are similar for all rates at the same strains. Hence, as the stain rate increased, the pore nucleation rate increased.

The mean nearest neighbor curves were similar for all cases, but the values were initially larger for the 144 phospholipid structure due to pores nucleating farther apart in the x dimension. Initially, the mean nearest neighbor distance curves begin spiking and going back to zero due to pores forming and closing. This spiking continues until the pores remain visible and allow continuous detection. Figure 3.8 shows that as pores nucleate and grow, the mean nearest neighbor distance continues to decrease until becoming relatively constant.

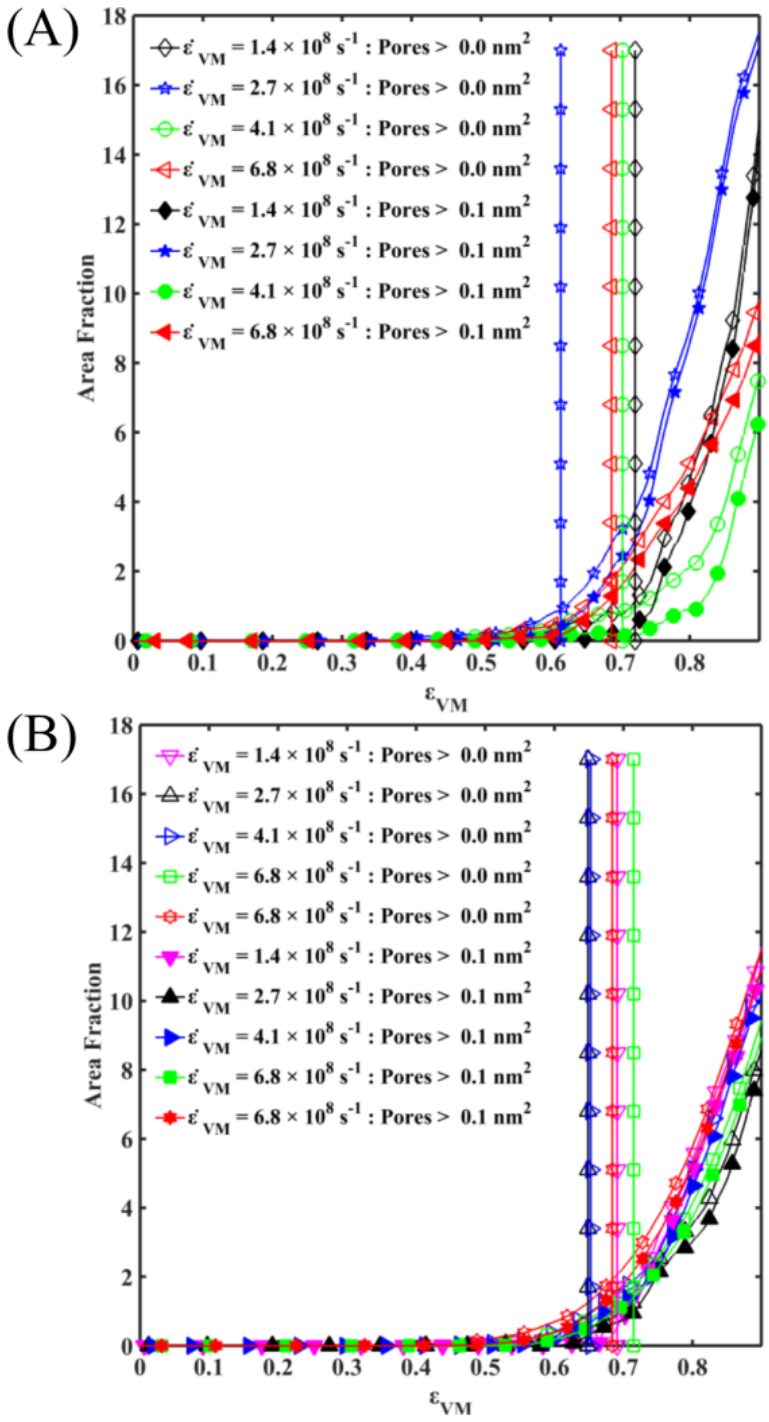

Figure 3.6 Percent area fraction for the (A) 72 phospholipid and (B) 144 phospholipid bilayer for the von Mises rates of 1.4×10^8 s^{-1}, 2.7×10^8 s^{-1}, 4.1×10^8 s^{-1}, and 6.8×10^8 s^{-1}.

Vertical lines with markers matching their corresponding curve indicate when full water penetration occurred.

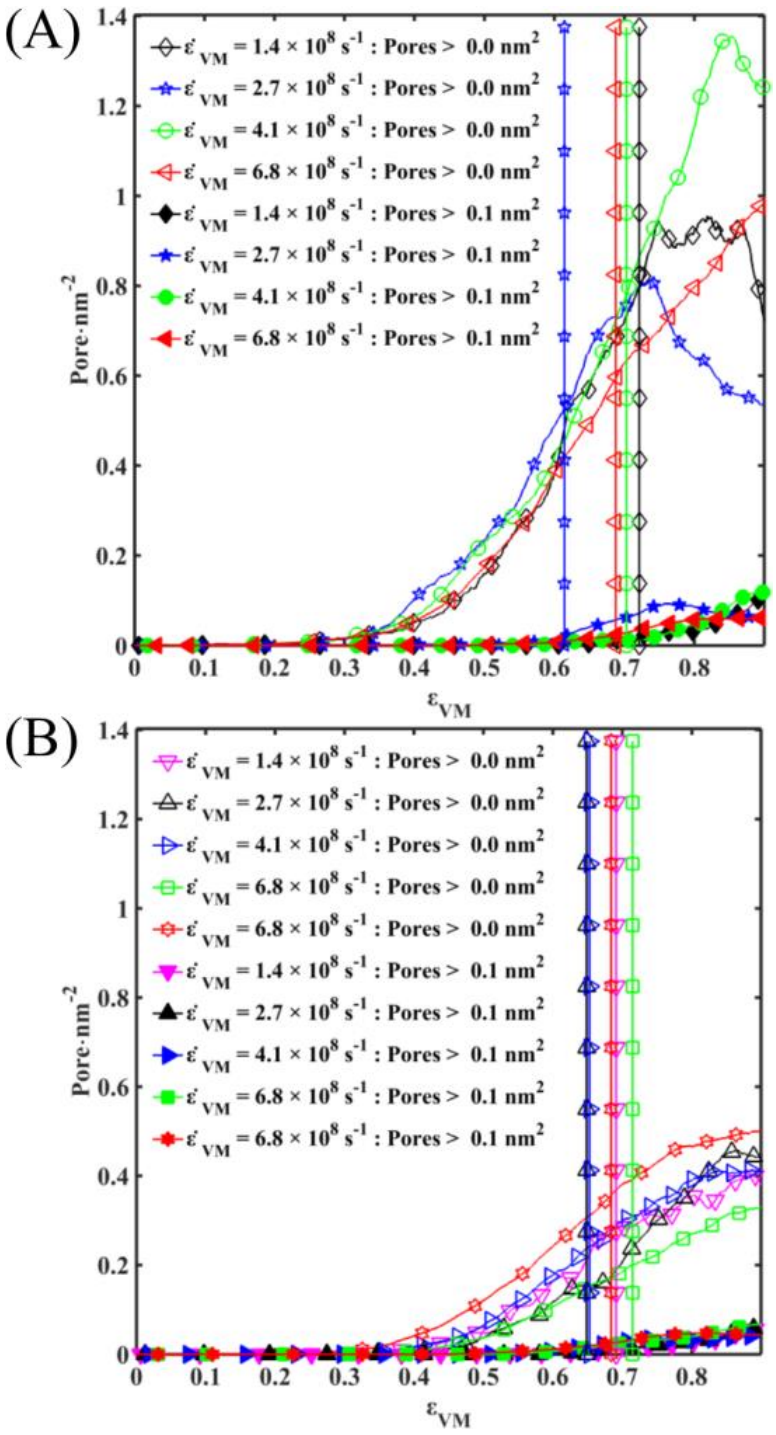

Figure 3.7 Pore number density for the (A) 72 phospholipid and (B) 144 phospholipid bilayer for the von Mises strain rates of 1.4×10^8 s^{-1}, 2.7×10^8 s^{-1}, 4.1×10^8 s^{-1}, and 6.8×10^8 s^{-1}.

Vertical lines with markers matching their corresponding curve indicate when full water penetration occurred.

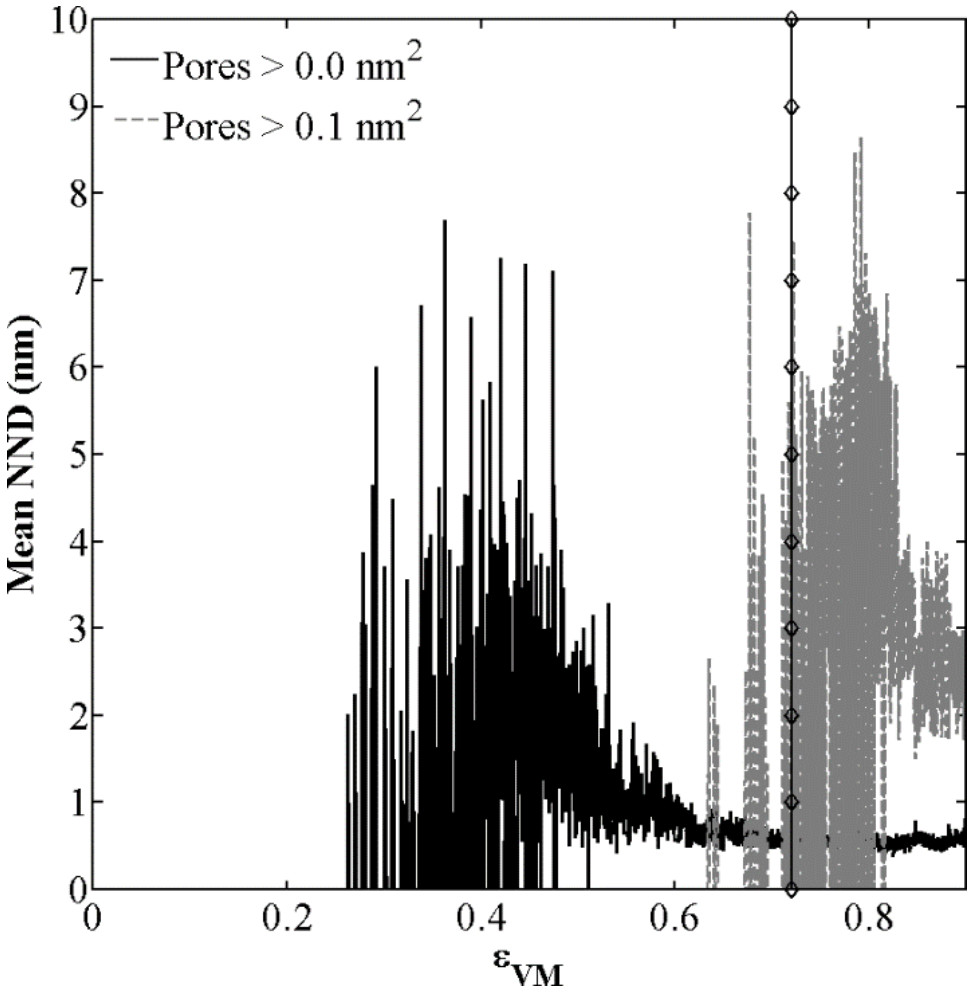

Figure 3.8 Mean nearest neighbor distance for the 72x1 case ($\dot{\varepsilon} = 1.4 \times 10^8$).

A vertical line with markers indicates when full water penetration occurred.

3.3.2 Deformation Stress

Figure 3.9 and Figure 3.10 show that all of the structures experienced "yield" stress when the simulation box deformed near the beginning of the straining. The stress then decreased until it saturated at a certain level. The 72x1 and 144x1.9 cases were an exception to this behavior because they continued to fluctuate around the initial maximum stress for the remaining deformations. The effect of bilayer planar and cross-

sectional areas on the von Mises stress and point of failure in Figure 3.10 appears to be minimal.

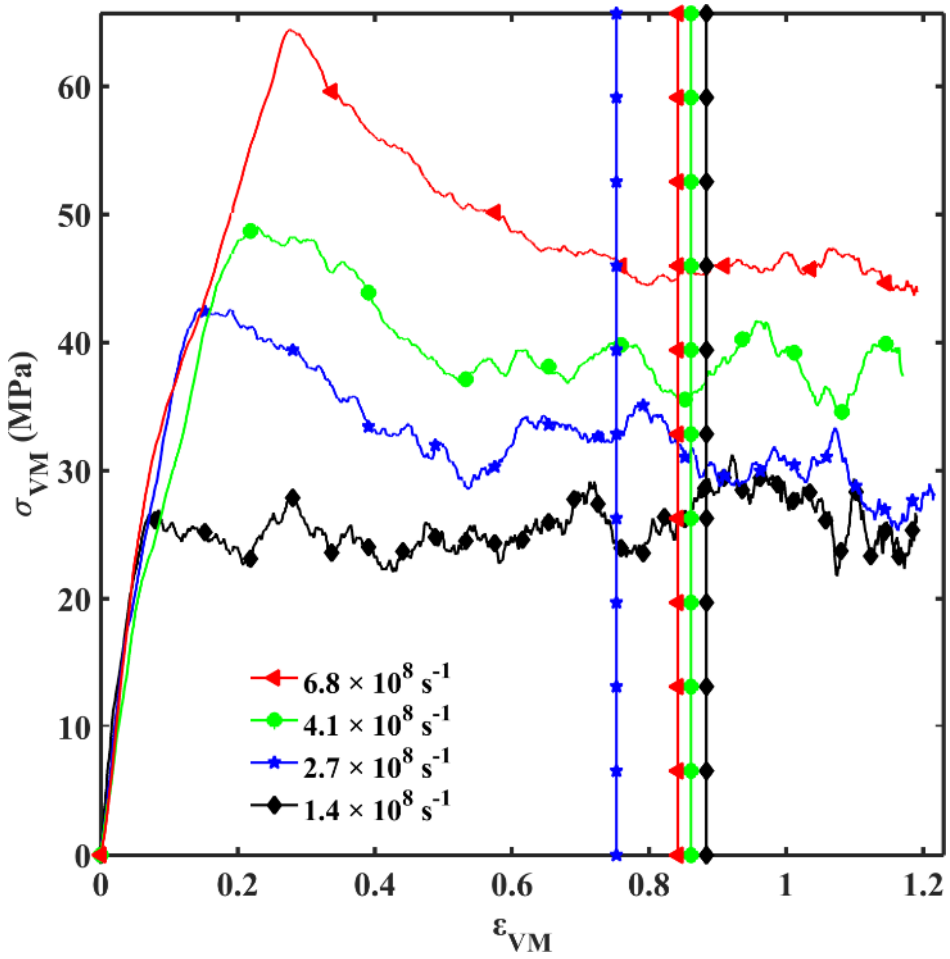

Figure 3.9 Von Mises stress-strain curve displaying the effect of the strain rate ($\dot{\varepsilon}_{VM}$ = 1.4×10^8 s^{-1}, 2.7×10^8 s^{-1}, 4.1×10^8 s^{-1}, and 6.8×10^8 s^{-1}) on the 72 phospholipid bilayer.

Vertical lines with markers matching their corresponding curve display when full water penetration occurred.

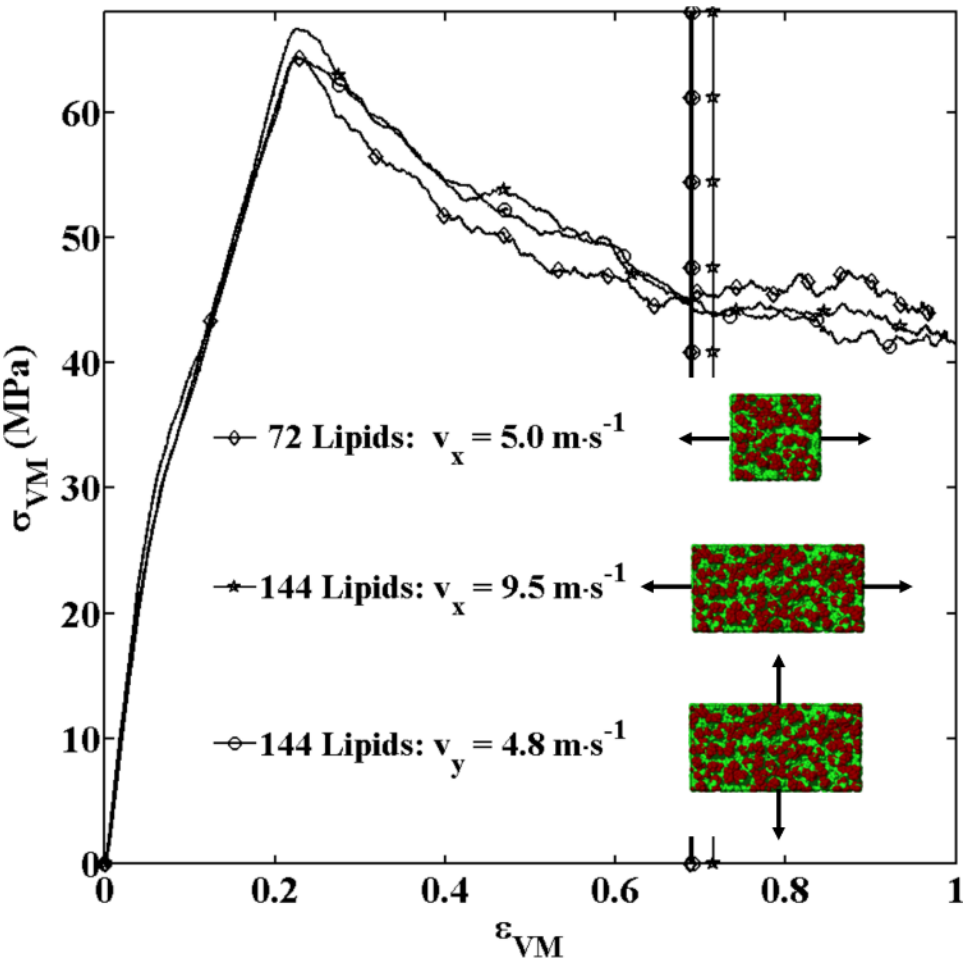

Figure 3.10 Von Mises stress-strain curve displaying the effect of planar and cross-sectional area at a von Mises strain rate of 6.8×10^8 s^{-1}.

Vertical lines with markers matching their corresponding curve display when full water penetration occurred.

3.4 Discussion

The widespread prevalence and damage resulting from TBI necessitates a high fidelity computational model. Current constitutive material models lack the localized damage describing neuronal damage [2-6]. In an attempt to describe this local damage, molecular dynamics can be employed to analyze and develop the MPISVs required for implementing damage in the constitutive material model via a multiscale modelling hierarchy. However, previous *in silico* studies of membrane damage have primarily

focused on deforming the phospholipid bilayer to match experiments, largely limiting the simulations to in-plane equibiaxial deformations [14-18].

The current study investigates mechanoporation (deformation and failure) of a simplified membrane resulting from an external mechanical insult, specifically with regard to strip biaxial tension at four different strain rates, two bilayer planar areas, and two bilayer cross-sectional areas. All simulations used POPC phospholipids to simulate mechanoporation on a membrane due to high rate deformations. To quantify the damage due to mechanoporation, image analysis was used to investigate pore nucleation and growth. We have explored mechanical damage progression within a phospholipid bilayer in the strip biaxial strain state under high strain rates. The lower limit velocities employed here (see Table 3.1) include the upper limit velocity used by Koshiyama and Wada [18] for equibiaxial bilayer deformation simulations. The upper limit velocity also exceeds most of the velocities used for the NOCSAE drop standard, a test for the efficacy of football helmets [29], and exceed the velocities expected for typical falls. The velocities for falls are particularly important considering falls are the leading cause of TBI in the United States [1]. However, velocities causing macroscale injuries likely do not translate directly to those observed at the nanoscale length scale, as indicated by the extremely high strain rates that arise in small structures. Therefore, the primary goal is to identify and quantify relevant nanoscale damage mechanisms and specifically quantify pore nucleation, pore growth, and pore coalescence so that a physics-based multiscale modelling framework for a macroscale MPISV constitutive model can be developed for TBI [30]. The macroscale damage model can be multiplicatively decomposed into the three MPISVs in the following equation [30],

$$\phi = \eta v c \tag{3.1}$$

such that the rate equation with respect to time is given by the following,

$$\dot{\phi} = \dot{\eta} v c + \eta \dot{v} c + \eta v \dot{c} \tag{3.2}$$

where ϕ is the pore volume fraction (or area in two dimensions) sometimes called damage, and $\dot{\phi}$ is the time rate of change of the pore volume; η and $\dot{\eta}$ are the pore nucleation MPISV (number of pores per volume) and pore nucleation rate, respectively; v and $\dot{v}$ are the pore growth MPISV and pore growth rate, respectively; and c and $\dot{c}$ are the pore coalescence MPISV (inverse of nearest neighbor distance) and pore coalescence rate, respectively. In addition, calculation of the von Mises strain, von Mises stress, and surface tension for the structure allowed quantification of the mechanical response to deformations.

3.4.1 Pore Nucleation and Growth

Overall, the 72 and 144 phospholipid bilayers had similar behavior regarding pore nucleation. Strain rate only affected pore growth after water penetration. Figure 3.4 displays the general progression of structure failure from the initial structure to multiple fully penetrating pores. Initially, even though initial pore detection via image analysis occurs by Figure 3.4 (B) and pores larger than 0.1 nm^2 by Figure 3.4 (D), they are not visible under casual visual inspection. Indeed, not until water penetration occurs, as shown in Figure 3.4 (E), are pores readily visible. Despite having a similar response with regard to pore nucleation, initially following water penetration, the lowest strain rate cases (1.4×10^8 s^{-1}) preferentially expand a single pore that is more circular in shape

while secondary locations of water penetration do not initially expand. The higher strain rates ($\dot{\varepsilon}_{VM} = 2.7 \times 10^8\ s^{-1}$, $4.1 \times 10^8\ s^{-1}$, and $6.8 \times 10^8\ s^{-1}$) exhibit growth of multiple pores of similar area that were less circular in shape, which Figure 3.5 shows through a comparison of the 72x1 and 72x2 cases. In an experimental study, Evans, et al. [11] proposed that phospholipid bilayer failure at high loading rates were "defect-limited" with failure relying on the nucleation of "defects". This observation is consistent with observations of the current simulations where chains of water penetrate into resulting gaps (defects) between phospholipid heads in both leaflets. These gaps lead to full water penetration when two of the water chains meet. However, because the lowest strain rate results in different behavior after water penetration, it appears this defect-limited regime must be subdivided further depending on strain rate. Assuming that the single circular pore is more thermodynamically stable, the transition to multiple less-circular pores suggests that the higher strain rate deformations are pulling the phospholipid bilayer apart faster than the pores can obtain the thermodynamically preferable form. Interestingly, because the mean pore area does not change with strain rate, the max pore area must be larger for the lowest strain rate because the later pores do not immediately expand, which reduces the mean pore area. Conversely, that also means that the difference between the max pore area and mean pore area was smaller for the higher rates where multiple pores expanded. This change in the pore growth paths could have significant implications regarding the size of molecules allowed entry into the cell during deformations at different deformation rates.

Figure 3.6 shows the porosity (or pore area fraction) curves, and Figure 3.7 shows the pore number density curves, which represent pore nucleation. The pore number

density curves in Figure 3.7 show that pores begin nucleating under small strains of the phospholipid bilayer, but these pores are transient and indicate that voids (internal defects) are nucleating within the phospholipid structure. In response, the phospholipid tails rearrange to fill the voids and cause phospholipid bilayer thinning. If the structure were allowed to relax, pores would quickly close as the structure recovered. However, pores large enough for water molecules have the potential to become stable because they allow water chains to dip into the hydrophobic region of the phospholipid bilayer. Chains dipping separately into the upper and lower bilayer leaflets can connect to form a bridge, leading to pore stability and growth. Despite the number of smaller pores being much greater than the number of larger pores, the larger pores make up the bulk of the pore area fraction. Figure 3.8 shows full water penetration occurs after the appearance of multiple larger pores, indicating larger pores are a greater indicator of when water penetration is likely to occur. Because pores need to reach a minimum cross-sectional area of roughly 0.07 nm^2 to allow a water molecule to pass through and because water molecules need time to initially diffuse through the bilayer leaflets, the water penetration occurring shortly after the appearance of pores larger than 0.1 nm^2 is not surprising.

Figure 3.6 and Figure 3.7 also show that the larger structure reduces the amount of variability between strain rates for pore area fraction and pore number density. The increased number of phospholipids in the larger structure are likely able to rearrange more efficiently, given the extra space provided by a larger volume, allowing them to fill voids more easily. This phospholipid rearrangement would explain why the larger structure has lower pore number density values than those observed in the smaller

structure. Similarly, more efficient phospholipid rearrangement also explains why less variability is present in the area fraction curves for the larger structure.

3.4.2 Strain

The strain rate, planar bilayer area, and cross-sectional bilayer area had no significant effect on the strains associated with pore nucleation or on the full water penetration (failure) strain. There was no obvious pattern to when pores initially began to nucleate (Table 3.2). The lack of a consistent strain at which the small pores nucleated is due to phospholipids rearranging to fill small nucleating voids. Therefore, the initial pore nucleation depends on how the local phospholipids randomly rearrange during structural deformation, regardless of strain rate. In comparison, the strains for the detection of pores ≥ 0.1 nm^2 occurred at a von Mises strain of $0.509 \pm 7.8\%$. The detection of larger pores at a specific strain indicates that the phospholipid bilayer had reached a critical strain threshold where it could no longer rearrange sufficiently by thinning to offset stretching effects. Because failure occurred shortly after the appearance of multiple larger pores, the von Mises strain at failure ($0.68 \pm 4.8\%$) is consistent with the idea of critical strain thresholds as well.

The strains at failure are approximately twice the upper range of values found in simulations of equibiaxial deformations of POPC by Koshiyama and Wada [18], who found that the structure failed in the von Mises strain range of $0.20 \leq \varepsilon_{failure} \leq 0.37$. Additionally, Koshiyama and Wada [18] found that increasing strain rates caused the strain at failure to increase; however, our work revealed that the strain rate only affected the strain at which the yield stress occurred. Assuming the strip biaxial and equibiaxial strain states behave similarly with regards to the rate dependency of the failure strain, the

failure strain found in the current study suggests that a threshold strain rate exists where the failure strain becomes strain rate independent.

3.4.3 Stress

Figure 3.9 reveals that the phospholipid bilayer is highly dependent on the strain rate with regards to the stress levels and the yield strain. As the strain rate increases, the stress increases. Similarly, the yield strain increases with strain rate because the large strain rates extend the elastic regime. This behavior occurs in most materials, including metals, polymers, and other biomaterials. More specifically, because the phospholipid bilayer behaves as a fluid, the initial peak behavior is a result of the phospholipid bilayer viscosity, which would cause an initial resistance to change.

Figure 3.10 shows that the bilayer planar and cross-sectional area did not affect the stress response. The largest percent deviations for yield stress and strain of the applied strain rates (which were applied to multiple phospholipid bilayer areas) were 4.86% and 5.88%, respectively, showing that there was very little deviation due to planar or cross-sectional area. These values indicate that the number of phospholipids, and in extension the phospholipid bilayer area, is not a limiting factor over the area range used in these simulations and that deformations are only strain rate dependent at the currently simulated scales.

The current study agrees with previous experimental and computational studies qualitatively with regards to the stress response of the phospholipid bilayer being strain rate dependent [11, 18]. Experimentally, phospholipid bilayers fail at low surface tensions (stresses), even when stiffened with cholesterol [13]. However, due to simulation strain rates being many orders of magnitude larger than those produced in experiments,

directly comparing surface tension results is not possible. The difference in strain rate between simulation and experimental studies requires a comparison via estimates based on experimental data. These estimates were determined based on Equation 3.3 [11].

$$\frac{\gamma}{\gamma_\delta} = \ln\left(\frac{\Re_\delta}{\nu_{0\delta}{}^*\gamma_\delta}\right) \tag{3.3}$$

where γ ($N{\cdot}m^{-1}$) is the rupture surface tension, γ_δ ($N{\cdot}m^{-1}$) is a normalization material parameter, $\nu_{0\delta}$ (s^{-1}) is the frequency for spontaneous nucleation of defects, and $\Re_\gamma$ ($N{\cdot}m^{-1}{\cdot}s^{-1}$) is the loading rate. Note that Evans, et al. [11] originally used the symbol σ to represent surface tension in this equation, but it was replaced with γ for consistency with the surface tension equation in Section 2.3.2. Following the approach described by Evans, et al. [11], the material parameters γ_δ and $\nu_{0\delta}$ were determined. First, the loading rate $\Re_\gamma$ ($N{\cdot}m^{-1}{\cdot}s^{-1}$) was determined from the slope of the surface tension versus time curve for each deformation case. Then, the yield surface tension values for each deformation case was plotted against the natural log of $\Re_\gamma$. The slope of the yield surface tension versus $\ln(\Re_\gamma)$ curve was found, giving the value $\gamma_\delta = 0.13$ $N{\cdot}m^{-1}$. The relation $\Re_{\gamma=0} = \nu_{0\delta}{}^*\gamma_\delta$ was then used to solve for $\nu_{0\delta} = 1.3 \times 10^9$ s^{-1} after determining $\Re_{\gamma=0}$ using the linear trend line equation from the yield surface tension versus $\ln(\Re_\gamma)$ curve.

The resulting line fits well with the values determined in the current simulations with an R^2 value of 0.97, showing that the data follow the expected semi-log linear trend. However, the parameter values found here differ considerably from those found by Evans, et al. [11], whose values were ~0.2 s^{-1} and 4.0×10^{-3} $N{\cdot}m^{-1}$ for $\nu_{0\delta}$ and γ_δ, respectfully, for similar phospholipid types. This difference indicates that there may be limited regimes of deformation rates for which these parameters values are valid. From a physical viewpoint, it makes sense that these parameters would change, because it is a

reasonable expectation for the nucleation rate $v_{0\delta}$ to increase with the deformation rate, although the reasoning for why they are constant for ranges of loading rates, leading to defined regimes, may not be as readily apparent. The authors believe these regimes may correspond to physical phenomena, and, in this case, the observed regime likely corresponds to the inability of the energetically favorable single larger pore to form at higher rates. In other words, the parameter values found using the current simulation data correspond to loading rates where the phospholipid bilayer cannot adequately rearrange to form the pore's energetically favored form. The change in pore growth behavior implies that some point exists where the linear curve on a semi-log plot, representing the deformation rate regime seen in the current study, will suddenly change to another, similar linear curve with different parameter values. If true, this process would continue and bridge the defect-limited deformation parameter values originally observed by Evans, et al. [11] and the parameter values for the current observed deformation rate regime.

Although the fitting method used for the current simulations is the same method used for experimental studies [11], and the surface tension versus $\ln(\Re_\gamma)$ curve follow the same semi-log linear trend as experimental data [11], it is likely that the surface tension magnitude is dependent on the chosen phospholipid force field, so the values determined using simulations should be considered approximations, as with any simulation. That stated, the magnitude of these values suggests that the rupture strength of the phospholipid bilayer increases quickly when deformed under high strain rates.

Additionally, the stress peaks and falls prior to water penetration, indicating that the phospholipid bilayer could potentially sustain temporary high rate deformations (and the resulting high stress) without permanent injury to the neuron. While the human body

is unlikely to experience these strain rates as a whole under normal circumstances, when considering the local nanostructure, it only requires a deformation of a few meters per second to reach these deformation rates. This observation indicates that, at the rates tested in this study, phospholipid bilayers will fail primarily due to reaching a critical strain, rather than due to mechanical stress. To substantiate this observation in other strain states, future simulations will include similar high strain rate deformations for the equibiaxial and non-equibiaxial strain states. The authors will also examine the mechanical responses of membranes stiffened with cholesterol, attempt to improve upon the image analysis methods used, and perform analysis for larger pores, such as those needed for the passage of Ca^{2+} ions and other biomarkers believed to be major contributors to cell dysfunction and apoptosis during TBI.

3.5 Conclusions

The current study has examined the deformation characteristics of a POPC phospholipid bilayer when deformed under strip biaxial tension while varying the strain rate and the bilayer area. The major findings are the following:

1. The 72 and 144 phospholipid bilayers maintained similar behavior regarding the pore nucleation strains for all applied strain rates (Figure 3.6 and Figure 3.7). Post water penetration (failure), the applied strain rates affected the shape and number of expanding pores (Figure 3.5).
2. Multiple pores with an area of 0.1 nm^2 were detected before the first full water penetration occurrence (Figure 3.8) regardless of strain rate, planar area, or cross-sectional area.

3. The applied strain rates, planar area, and cross-sectional area had no effect on the von Mises strains at which pores greater than 0.1 nm^2 were detected (0.509 ± 7.8%) or the von Mises strain at which full water penetration (failure) (0.68 ± 4.8%) occurred. See Table 3.2 for individual case values.
4. The phospholipid bilayer yield stress and strain increased as the strain rate increased (Figure 3.9), but they did not change due to the bilayer planar or cross-sectional area (Figure 3.10). Hence, no size scale issue arose for mechanical analysis of the phospholipid bilayers.

In addition, current findings concurred with previous experimental studies [11] with respect to pore damage resulting from high rates being defect-limited. The results also agree qualitatively with other experimental and simulated results in that the phospholipid bilayer stress response is rate dependent [11, 18].

3.6 Acknowledgements

This material is based upon work supported by the Center for Advanced Vehicular Systems (CAVS) and the Tissue Engineering Research Center (TERC) through the Department of Agricultural and Biological Engineering at Mississippi State University. We would also like to thank the NSF EPSCoR research program (EPS_0903787) for funding the multiscale aspect of the current research. Any opinions, findings, and conclusions or recommendations expressed in this material are those of the author(s) and do not necessarily reflect the views of the NSF.

3.7 References

[1] M. Faul, L. Xu, M. M. Wald, and V. G. Coronado, "Traumatic Brain Injury in the United States: Emergency Department Visits, Hospitalizations, and Deaths 2002-2006," ed. Atlanta (GA): Centers for Disease Control Prevention, National Center for Injury Prevention and Control, 2010.

[2] R. J. H. Cloots, H. M. T. Gervaise, J. A. W. van Dommelen, and M. G. D. Geers, "Biomechanics of Traumatic Brain Injury: Influences of the Morphologic Heterogeneities of the Cerebral Cortex," *Annals of Biomedical Engineering,* vol. 36, pp. 1203-1215, 2008/07/01 2008. doi: 10.1007/s10439-008-9510-3.

[3] N. C. Colgan, M. D. Gilchrist, and K. M. Curran, "Applying DTI white matter orientations to finite element head models to examine diffuse TBI under high rotational accelerations," *Progress in Biophysics and Molecular Biology,* vol. 103, pp. 304-309, 12// 2010. doi: 10.1016/j.pbiomolbio.2010.09.008.

[4] R. Prabhu, M. F. Horstemeyer, M. T. Tucker, E. B. Marin, J. L. Bouvard, J. A. Sherburn*, et al.*, "Coupled experiment/finite element analysis on the mechanical response of porcine brain under high strain rates," *Journal of the Mechanical Behavior of Biomedical Materials,* vol. 4, pp. 1067-1080, 2011. doi: 10.1016/j.jmbbm.2011.03.015.

[5] R. Prabhu, M. F. Horstemeyer, Y. Mao, J. L. Bouvard, E. B. Marin, L. N. Williams*, et al.*, "Simulation Based Analysis of an Experimentally Quantified Traumatic Brain Injury from an In-Theater Blast Explosion.," *(Under review, PNAS),* 2014.

[6] B. Yang, K.-M. Tse, N. Chen, L.-B. Tan, Q.-Q. Zheng, H.-M. Yang*, et al.*, "Development of a Finite Element Head Model for the Study of Impact Head Injury," *BioMed Research International,* vol. 2014, 2014. doi: 10.1155/2014/408278.

[7] O. Farkas, J. Lifshitz, and J. T. Povlishock, "Mechanoporation Induced by Diffuse Traumatic Brain Injury: An Irreversible or Reversible Response to Injury?," *J Neurosci,* vol. 26, pp. 3130-40, Mar 22 2006. doi: 10.1523/JNEUROSCI.5119-05.2006.

[8] D. Kilinc, G. Gallo, and K. A. Barbee, "Mechanically-induced membrane poration causes axonal beading and localized cytoskeletal damage," *Experimental Neurology,* vol. 212, pp. 422-430, 8// 2008. doi: 10.1016/j.expneurol.2008.04.025.

[9] D. M. Geddes, R. S. Cargill, 2nd, and M. C. LaPlaca, "Mechanical stretch to neurons results in a strain rate and magnitude-dependent increase in plasma membrane permeability," *J Neurotrauma,* vol. 20, pp. 1039-49, Oct 2003. doi: 10.1089/089771503770195885.

[10] O. Farkas and J. T. Povlishock, "Cellular and subcellular change evoked by diffuse traumatic brain injury: a complex web of change extending far beyond focal damage," in *Progress in Brain Research*. vol. Volume 161, T. W. John and I. R. M. Andrew, Eds., ed: Elsevier, 2007, pp. 43-59.

[11] E. Evans, V. Heinrich, F. Ludwig, and W. Rawicz, "Dynamic tension spectroscopy and strength of biomembranes," *Biophys J,* vol. 85, pp. 2342-50, Oct 2003. doi: 10.1016/S0006-3495(03)74658-X.

[12] E. Evans and B. A. Smith, "Kinetics of Hole Nucleation in Biomembrane Rupture," *New J Phys,* vol. 13, Sep 16 2011. doi: 10.1088/1367-2630/13/9/095010.

[13] D. Needham and R. S. Nunn, "Elastic deformation and failure of lipid bilayer membranes containing cholesterol," *Biophysical Journal,* vol. 58, pp. 997-1009, 10// 1990. doi: 10.1016/S0006-3495(90)82444-9.

[14] D. P. Tieleman, H. Leontiadou, A. E. Mark, and S. J. Marrink, "Simulation of pore formation in lipid bilayers by mechanical stress and electric fields," *J Am Chem Soc,* vol. 125, pp. 6382-3, May 28 2003. doi: 10.1021/ja029504i.

[15] H. Leontiadou, A. E. Mark, and S. J. Marrink, "Molecular dynamics simulations of hydrophilic pores in lipid bilayers," *Biophys J,* vol. 86, pp. 2156-64, Apr 2004. doi: 10.1016/S0006-3495(04)74275-7.

[16] T. V. Tolpekina, W. K. den Otter, and W. J. Briels, "Simulations of stable pores in membranes: system size dependence and line tension," *J Chem Phys,* vol. 121, pp. 8014-20, Oct 22 2004. doi: 10.1063/1.1796254.

[17] M. D. Tomasini, C. Rinaldi, and M. S. Tomassone, "Molecular dynamics simulations of rupture in lipid bilayers," *Experimental Biology and Medicine (Maywood, N.J.),* vol. 235, pp. 181-8, Feb 2010. doi: 10.1258/ebm.2009.009187.

[18] K. Koshiyama and S. Wada, "Molecular dynamics simulations of pore formation dynamics during the rupture process of a phospholipid bilayer caused by high-speed equibiaxial stretching," *Journal of Biomechanics,* vol. 44, pp. 2053-8, 2011/07/28/ 2011. doi: 10.1016/j.jbiomech.2011.05.014.

[19] J. B. Klauda. (n.d., June 23). *Laboratory of Molecular & Thermodynamic Modeling*. Available: http://mackerell.umaryland.edu/CHARMM_ff_params.html

[20] S. Plimpton, "Fast Parallel Algorithms for Short-Range Molecular Dynamics," *Journal of Computational Physics,* vol. 117, pp. 1-19, 3/1/ 1995. doi: 10.1006/jcph.1995.1039.

[21] J. B. Klauda, R. M. Venable, J. A. Freites, J. W. O'Connor, D. J. Tobias, C. Mondragon-Ramirez*, et al.*, "Update of the CHARMM All-Atom Additive Force Field for Lipids: Validation on Six Lipid Types," *Journal of Physical Chemistry B,* vol. 114, pp. 7830-7843, 2010/06/17 2010. doi: 10.1021/jp101759q.

[22] W. Shinoda, M. Shiga, and M. Mikami, "Rapid estimation of elastic constants by molecular dynamics simulation under constant stress," *Physical Review B,* vol. 69, p. 134103, 04/07/ 2004.

[23] A. Leach, *Molecular Modelling: Principles and Applications (2nd Edition)*. Harlow, England: Prentice Hall, 2001.

[24] A. Stukowski, "Visualization and analysis of atomistic simulation data with OVITO–the Open Visualization Tool," *Modelling and Simulation in Materials Science and Engineering,* vol. 18, p. 015012, 2010.

[25] C. A. Schneider, W. S. Rasband, and K. W. Eliceiri, "NIH Image to ImageJ: 25 years of image analysis," *Nature Methods,* vol. 9, pp. 671-675, 2012. doi: 10.1038/nmeth.2089.

[26] A. H. Narten and H. A. Levy, "Liquid Water: Molecular Correlation Functions from X-Ray Diffraction," *The Journal of Chemical Physics,* vol. 55, pp. 2263-2269, 1971. doi: 10.1063/1.1676403.

[27] "MATLAB," 8.1.0.604 ed. Natick, MA: The MathWorks Inc., 2013.

[28] Y. Zhang, S. E. Feller, B. R. Brooks, and R. W. Pastor, "Computer simulation of liquid/liquid interfaces. I. Theory and application to octane/water," *The Journal of Chemical Physics,* vol. 103, pp. 10252-10266, 1995. doi: 10.1063/1.469927.

[29] NOCSAE, "Standard Performance Specification for Newly Manufactured Football Helmets," NOCSAE DOC (ND)002-13m13, December 2013.

[30] M. F. Horstemeyer, J. Lathrop, A. M. Gokhale, and M. Dighe, "Modeling stress state dependent damage evolution in a cast Al–Si–Mg aluminum alloy," *Theoretical and Applied Fracture Mechanics,* vol. 33, pp. 31-47, 2// 2000. doi: 10.1016/S0167-8442(99)00049-X.

CHAPTER IV

LOADING RATE EFFECT ON THE YIELD AND FAILURE BEHAVIORAL TRANSITION OF A SIMPLIFIED 1-PALMITOYL-2-OLEOYL-PHOSPHATIDYLCHOLINE (POPC) MEMBRANE

4.1 Introduction

While traumatic brain injury (TBI) is widespread and affects millions every year causing personal and financial loss [1-3], many of its aspects remain a mystery. Many experimental techniques have been used to study TBI, including observational studies of injured individuals using medical imaging techniques [4], controlled injuries using animal models [5, 6], directly deforming neurons *in vitro* [7-9], and testing headforms and other dummy models. However, all of these have two major disadvantages. The first disadvantage is that none of these methods show the full picture of TBI. Observational studies can typically only view the after-effects of the injury, effects seen in animal models may not directly translate to humans, cell cultures are a micro-window of what could be happening during injury, and dummy models only provide no physiological feedback. The second disadvantage is that, with the exception of the dummy models, these methods have limited to no applicability in designing and optimizing protective gear to prevent TBI in the first place. To address both of these disadvantages, computer models of TBI can be implemented.

Finite element analysis (FEA) is a common method for simulating TBI. Current models of TBI use brain material models with internal state variables focused on mechanical properties and lack lower length scale physiological effects [10-14] [10, 11, 13-20]. For a model to best capture the effects of TBI, both mechanical and physiological aspects must be implemented. In line with this idea, relevant nanoscale and microscale injury mechanisms must be quantified and implemented using a Mechano-Physiological Internal State Variable (MPISV) model. In doing so, temperature, strain rate, stress state, and history effects can be added to the FEA model [21, 22]. To build this model, needed parameters must be identified and then quantified using experiments or lower-length scale simulations.

Cell membrane mechanoporation has been shown to be an important injury mechanism during TBI [23-26], so this injury mechanism is a prime target to be added to the MPISV model. It has been shown in both experimental [27] and computational [28, 29] studies that the phospholipid bilayer is rate dependent with regards to the stress response. Additionally, Evans, et al. [27] showed that the membrane failure mechanism changes at high loading rates. This leads to low and high loading rate regimes with low rates leading to cavitation-limited failure and high rates leading to defect-limited failure [27]. A similar phenomenon was observed by Murphy, et al. [29] when deforming a membrane *in silico*, who noted that the defect-limited high loading rate regime described by Evans, et al. [27] may need to be divided into multiple regimes. This assertion is also supported by multiple studies that have noted that higher strain rates tend to develop multiple simultaneous pores [28-30]. Evidence for a behavioral strain rate transition can also be observed via the stress behavior, which continues to slowly increases post yield at

lower strain rates [28, 31] but yields and then decreases during higher rates [29]. In the current study, the molecular dynamics method and the empirical relations derived by Evans, et al. [27] are used to investigate the phospholipid bilayer deformation strain rate required for the pore growth and stress behavioral transition to occur.

4.2 Methods

4.2.1 Simulation Model and Deformations

Simulations were performed as described in CHAPTER II and CHAPTER III. To summarize, simulations were performed using the program LAMMPS [32] and the CHARMM36 all-atom lipid force field [33]. Seventy-two 1-palmitoyl-2-oleoylphosphatidylcholine (POPC) phospholipids and 9,070 TIP3P water molecules (original structure sourced from NIH's Laboratory of Computation Library [34] and 6,828 TIP3P water molecules were added) was equilibrated for five nanoseconds. This equilibration was repeated three times with different velocity seed numbers to obtain different initial structures. The structure created using the first seed number was then replicated by a factor of two in the x dimension, resulting in a 144 phospholipid structure. All 72 phospholipid structures were equilibrated for another five ns for a total of 10 ns of equilibration.

The equilibrated structures were subjected to constant velocity deformations in the x dimension and y dimensions as shown in Table 4.1 to give the equibiaxial and strip biaxial strain rates. The z dimension, and y dimension for uniaxial strain states, was allowed to adjust freely under a pressure of 1 atmosphere. Failure was assumed to have occurred when a water chain had extended through both bilayer leaflets.

Nose-Hoover style equations [35] were used for barostatting and thermostatting with a barostat constant of 500 fs, which was consistent with previous literature [28], and a thermostat constant of 100 fs. A particle-particle particle-mesh (PPPM) solver grid of 1×10^{-5} Å with analytical differentiation that updated every 500 fs was implemented. An inner cutoff radius of 10 Å was set for the Lennard-Jones and Coulombic interactions. A 0.5 fs timestep with the verlet integrator was used as recommended for systems with flexible molecules and bonds [36]. A neighbor list check was performed every timestep and updated if any atoms had moved more than 1 Å.

Table 4.1 Summary of Deformation Cases and Resulting Loading Rates

Case*	Strain State	$\dot{\varepsilon}_{VM}$ (s^{-1})	$\Re_\sigma$ ($MPa \cdot s^{-1}$)
72x4.0y3.8S1	Equibiaxial	5.5×10^8	4.3×10^{11}
72x3.7y4.0S2	Equibiaxial	5.5×10^8	4.2×10^{11}
72x4.0y3.7S3	Equibiaxial	5.5×10^8	4.2×10^{11}
72x2.8y2.7S1	Equibiaxial	3.9×10^8	3.5×10^{11}
72x0.6y0.6S1	Equibiaxial	8.7×10^7	9.1×10^{10}
72x0.2y0.2S1	Equibiaxial	3.3×10^7	4.2×10^{10}
72x0.1y0.1S1	Equibiaxial	1.3×10^7	1.8×10^{10}
72x5.0y0.0S1	Strip Biaxial	6.8×10^8	3.9×10^{11}
72x5.0y0.0S3	Strip Biaxial	6.8×10^8	3.6×10^{11}
72x4.7y0.0S2	Strip Biaxial	6.8×10^8	3.6×10^{11}
144x9.5y0.0S1	Strip Biaxial	6.8×10^8	3.4×10^{11}
72x0.0y4.8S1	Strip Biaxial	6.8×10^8	3.4×10^{11}
72x0.0y3.8S1	Strip Biaxial	5.5×10^8	3.3×10^{11}
144x7.6y0.0S1	Strip Biaxial	5.5×10^8	3.2×10^{11}
72x3.7y0.0S2	Strip Biaxial	5.5×10^8	3.0×10^{11}
72x4.0y0.0S1	Strip Biaxial	5.5×10^8	2.8×10^{11}
72x4.0y0.0S3	Strip Biaxial	5.5×10^8	2.6×10^{11}
144x5.7y0.0S1	Strip Biaxial	4.1×10^8	3.0×10^{11}
72x3.0y0.0S3	Strip Biaxial	4.1×10^8	2.7×10^{11}
72x2.8y0.0S2	Strip Biaxial	4.1×10^8	2.3×10^{11}
72x3.0y0.0S1	Strip Biaxial	4.1×10^8	1.9×10^{11}
72x2.0y0.0S1	Strip Biaxial	2.7×10^8	1.6×10^{11}
144x3.8y0.0S1	Strip Biaxial	2.7×10^8	1.6×10^{11}
72x1.8y0.0S2	Strip Biaxial	2.7×10^8	1.5×10^{11}
72x2.0y0.0S3	Strip Biaxial	2.7×10^8	2.7×10^{11}
72x1.0y0.0S1	Strip Biaxial	1.4×10^8	1.1×10^{11}
144x1.9y0.0S1	Strip Biaxial	1.4×10^8	9.9×10^{10}

*Case name identifies number of phospholipids, approximate velocities, and initial structure in the form: [Number of phospholipids]x[x velocity]y[y velocity]S[Initial velocity seed number]. For example, 72x4.0y3.8S1 is the equibiaxial strain state using the first equilibrated structure with x and y velocities of 4.0 and 3.8 $m \cdot s^{-1}$.

4.2.2 Correlation of Stress Versus Loading Rate

The defect-limited rupture relation experimentally derived for high loading rates in Evans, et al. [27] was adapted to the simulated datasets described above to examine

the divergence of the failure and yield stresses at the simulated loading rates. For clarity, the original procedure and modifications therof have been described. The originally derived equation is shown as Equation 4.1 [27].

$$\frac{\sigma}{\sigma_\delta} \cong ln\left(\frac{\mathcal{R}_\sigma}{\nu_{0\delta} * \sigma_\delta}\right) \tag{4.1}$$

Where σ ($N \cdot m^{-1}$) is the rupture surface tension, σ_δ ($N \cdot m^{-1}$) is a normalization material parameter, $\nu_{0\delta}$ (s^{-1}) is the frequency for spontaneous nucleation of defects, and $\Re_\sigma$ ($N \cdot m^{-1} \cdot s^{-1}$) is the loading rate. However, surface tension has been replaced by von Mises stress with units of megapascals. This change results in the normalization parameter σ_δ having units megapascals (MPa) and the loading rate $\Re_\sigma$ having units of megapascals per second ($MPa \cdot s^{-1}$). In line with this change, further descriptions of the method will simply refer to stress when describing the method rather than surface tension. $\Re_\sigma$ was recorded directly for each deformation case from the von Mises stress vs time curves and is shown in Table 4.1. A representative von Mises stress versus time curve demonstrating distinct loading regions and slope determination is shown in Figure C.1. Evans, et al. [27] recorded values for σ_δ as the slope from the rupture stress vs $\ln(\Re_\sigma)$ curves. Then, due to the linear nature of the defect-limited regime, the loading rate intercept can be extrapolated using the following relation [27]

$$\Re_{\sigma=0} = \nu_{0\delta} * \sigma_\delta \tag{4.2}$$

Here, the rearranged equation shows that $\nu_{0\delta}$ can be easily solved for after determining $\Re_{\sigma=0}$.

$$\nu_{0\delta} = \frac{\Re_{\sigma=0}}{\sigma_\delta} \tag{4.3}$$

This can be done easily using the equation of the line from the rupture stress vs $\ln(\Re_\sigma)$ curve. Since the relation is linear, the equation can be expressed simply with the equation $y = m * x + b$, where m is the slope and b is the intercept for the rupture stress vs $\ln(\Re_\sigma)$ curve. Plugging in the relevant variables, this equation becomes

$$\sigma = \sigma_\delta * \ln(\Re_\sigma) + b \tag{4.4}$$

At $\Re_{\sigma=0}$, this equation simply becomes

$$0 = \sigma_\delta * \ln(\Re_{\sigma=0}) + b \tag{4.5}$$

$$\Re_{\sigma=0} = \exp\left(-\frac{b}{\sigma_\delta}\right) \tag{4.6}$$

Lastly, the yield and failure stresses of bilayer systems as determined using simulated methods are being examined herein, not rupture stress as originally described by Evans, et al. [27].

4.3 Results

Figure 4.1 shows the applied strain rate affected the stress-strain behavior. For the three lowest strain rates shown in Figure 4.1, the stress-strain curve initially increased sharply before yielding. Post-yield, these cases continued to increase, but the rate of increase slowed and became more erratic. Conversely, the higher strain rates increased quickly to a much higher yield before beginning to decline. The strip biaxial strain state performed similarly, but the higher strain rate stress drop post-yield was more prominent. This stress-strain behavioral difference for the strip biaxial strain state is viewable in Figure 3.9 of CHAPTER III. Further, Figure 4.2 shows a comparison of the deformed structure for the equibiaxial strain state at the (A) highest and (B) lowest strain rates.

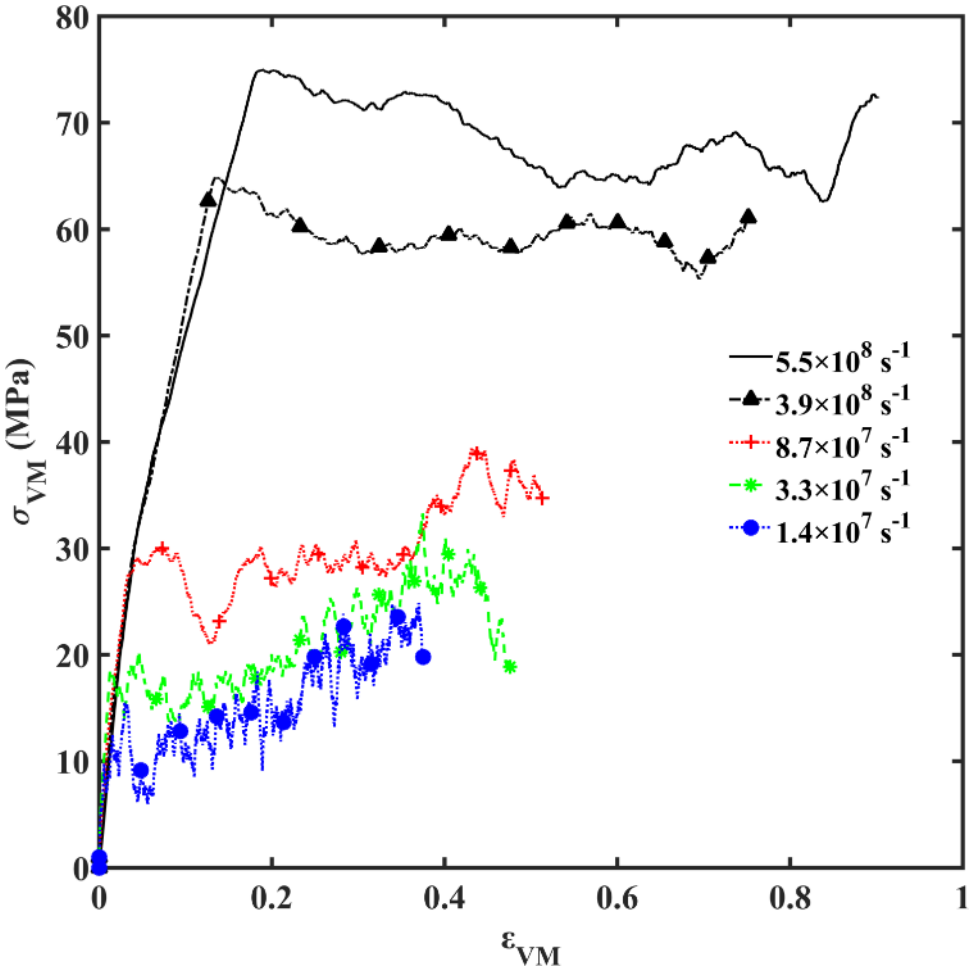

Figure 4.1 Von Mises stress-strain curve displaying the effect of strain rate ($\dot{\varepsilon}_{VM}$ =5.5 × 10^8 s^{-1}, 3.9 × 10^8 s^{-1}, 8.7 × 10^7 s^{-1}, 3.3 × 10^7 s^{-1}, and 1.4 × 10^7 s^{-1}) on the 72 phospholipid bilayer under equibiaxial tensile deformations.

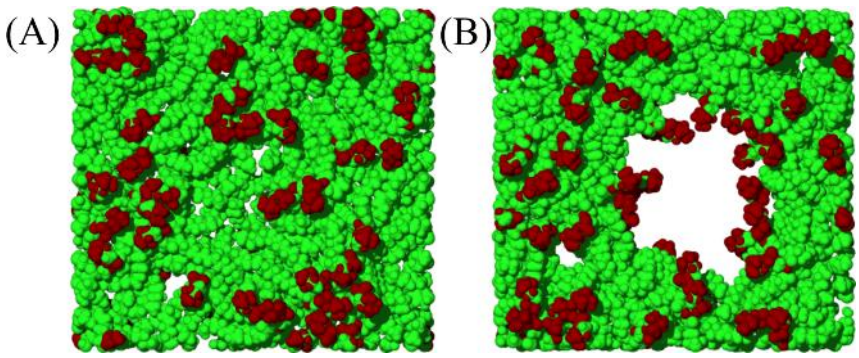

Figure 4.2 Top view comparison of the (A) 72x4.0y3.8S1 and (B) 72x0.1y0.1S1 cases at a von Mises strain (ε_{VM}) of 0.37.

Phospholipid headgroups are colored red, phospholipid tails are colored green, and water has been hidden. Note that water penetration had not occurred in (A).

The peak and failure stress were both fit using the procedure described by Evans, et al. [27]. Shown in Figure 4.3, the resulting fits were in good agreement with the obtained data for both the yield and failure stresses with the corresponding yield and failure R^2 values being 0.98 and 0.97 for the equibiaxial strain state and 0.98 and 0.92 for the strip biaxial strain state. Figure 4.3 also shows the yield and failure data intersect to provide an estimate for the strain rate regimes' transition point. The values determined using the Evans, et al. [27] empirical model are shown in Table 4.2. Additional equibiaxial mechanical properties including some estimated values from previous studies can be viewed in APPENDIX D.

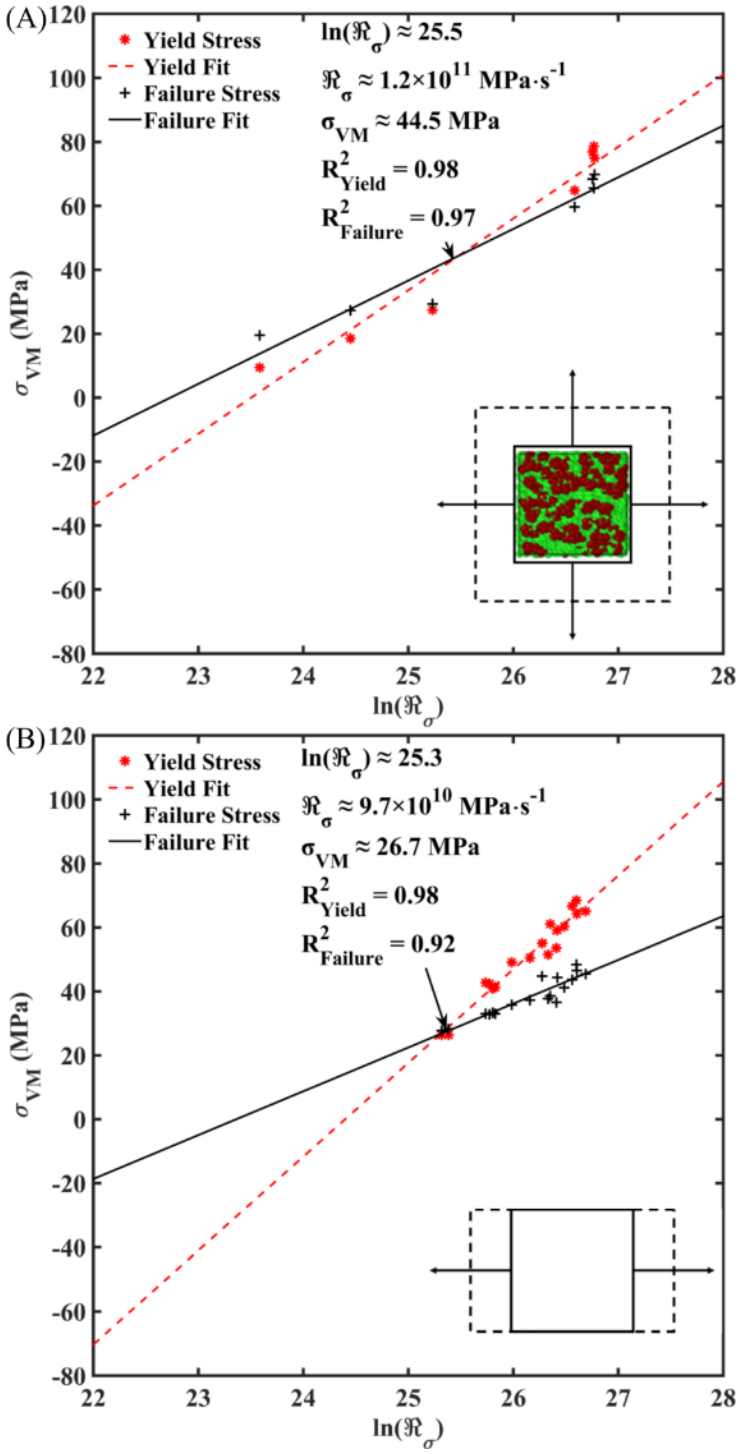

Figure 4.3 Yield and failure stress versus $\ln(\Re_\sigma)$ with the resulting linear fits for the (A) equibiaxial and (B) strip biaxial strain states.

In (A), the top view of the 72 phospholipid bilayer structure is shown with water hidden. Phospholipid headgroups are colored red and phospholipid tails are colored green.

Table 4.2 Summary of values determined using the method described by Evans, et al. [27] based on curves in Figure 4.3.

Fitting	Strain State	σ_δ (MPa)	R^2	$\Re_{\sigma=0}$ (MPa·s^{-1})	$\nu_{0\delta}$ (s^{-1})
Yield	Equibiaxial	22.4	0.98	1.6×10^{10}	7.2×10^{8}
	Strip Biaxial	29.3	0.98	3.9×10^{10}	1.3×10^{9}
	Both	22.7	0.95	2.1×10^{10}	9.4×10^{8}
Failure	Equibiaxial	16.2	0.92	7.5×10^{9}	4.6×10^{8}
	Strip Biaxial	13.7	0.97	1.4×10^{10}	1.0×10^{9}
	Both	12.9	0.77	8.5×10^{9}	6.6×10^{8}

4.4 Discussion

The potential for a behavioral transition von Mises strain rate in the defect-limited deformation regime of the phospholipid bilayer has been examined in the current study. While a comparison of studies shows a difference in properties and several studies have even observed effects related to exceeding this behavioral transition point [28-30], none have tried to quantify where this transition point occurs. In the context of improving the material model for TBI FEA models, quantifying this, and any other, major behavioral changes is essential to the overall goal of creating an accurate and comprehensive Mechano-Physiological Internal State Variable (MPISV) model. The current study demonstrates evidence for several of these effects including the effect on the stress-strain response and pore growth. Additionally, the simulation results were calibrated to the empirical model of Evans, et al [27] and have proposed a threshold strain rate and loading rate at which the discussed behavioral transition occurs.

4.4.1 Stress-Strain Behavior

Previous studies examining the deformation stress of the phospholipid structure have shown two distinct behaviors. Note that, while the current study uses von Mises

stress, most previous studies have used surface tension. Stress will be discussed in general regardless of which is being referred to because they provide a similar stress behavioral response, as shown in Figure B.3 of APPENDIX B. Several molecular dynamics studies have previously reported that equibiaxially deforming a membrane results in an immediate jump in stress before the structure yields, an observation of the current authors that was not made by the original authors, followed by a much slower gradual increase in stress until a sudden drop in stress occurs [28, 31]. Murphy, et al. [29] found that the membrane stress similarly increased to yield; however, the stress decreased post-yield with higher strain rates exhibiting a greater decrease in stress. The idea of multiple high strain rate regimes existing is consistent with these otherwise potentially conflicting results. Examining Figure 4.1, this distinct change can be confirmed. In this case, the range of von Mises strain rates extends from low 10^7 s^{-1} to mid 10^8 s^{-1}. Importantly, the stress behavior appears to change between the strain rate of 8.7×10^7 s^{-1} and 5.5×10^8 s^{-1}, displaying both stress behaviors mentioned above. This apparent transition narrows the potential range for the transition point.

For comparison, the Koshiyama and Wada [28] study's rates can be estimated from their reported structure dimensions and velocities, which shows their highest von Mises strain rate was on the order of 1.1×10^8 s^{-1}. Therefore, although their study also involved high rate deformations, the rates used by Murphy, et al. [29] were higher with a von Mises strain rate range of 1.4×10^8 s^{-1} to 6.8×10^8 s^{-1}. Interestingly, this estimate indicates the lower strain rate results reported by Murphy, et al. [29] were just above those reported by Koshiyama and Wada [28]. The magnitude of the stress response for the lowest strain rate examined by Murphy, et al. remained relatively constant post-yield,

meaning it did not truly follow the behavior described for either regime described. If it is assumed this unusual behavior is due to the lowest strain rate case being near the transition zone, this finding helps to further narrow the von Mises transition strain rate to around 1-1.4 × 10^8 s^{-1}.

4.4.2 Pore Growth Mechanism

Another important change in behavior involves the way pores grow. Figure 4.2 shows this change is quite dramatic with slower deformations allowing the growth of large pores at lower strains and higher rates initially nucleating more pores that do not grow as large. This difference is likely due to the phospholipids ability to react to the applied deformations to form more energetically favorable pore structure. Figure 4.2 (B) shows the phospholipid headgroups have repositioned themselves to face the pore walls and limit the water to phospholipid tail surface area, which provides evidence for this assertion. Due to the growth of large pores at lower strains, systems below the behavioral transition strain rate fail at lower strains. Looking again at Figure 4.2, small pores are visible in (A), but no water penetration has occurred even though water penetration has occurred and resulted in a large pore in (B). This difference could have potentially significant effects on how soon diffusion through the membrane would occur. Biologically, because lower strain rate deformations allow pores to grow large at low strains, they may actually be more detrimental than higher strain rate deformations because they would allow a loss of homeostasis under lower strains.

Several studies have also made note of this phenomena [28-30], but the results are seemingly contradictory. For example, Koshiyama and Wada [28] observed the multipore behavior, instead of a single larger pore, at a von Mises strain rate of 3.2 × 10^7 s^{-1}, based

on their reported structure size and velocities. Murphy, et al. reported seeing the single pore behavior at a rate equivalent to a von Mises strain rate of 2.7×10^8 s^{-1}. Further, Taiki, et al [30] reported that the multipore behavior occurs at a probability proportional to the deformation rate. Estimating the von Mises strain rates from their provided structure dimensions and velocities, they reported that a von Mises strain rate of 3.1×10^8 s^{-1} can exhibit the multipore behavior with a 55% probability for a pure dipalmitoyl-phosphatidylcholine (DPPC) membrane [30]. While this strain rate is similar to the rate found above, the current simulations have all exhibited multipore behavior in higher strain rates. This may be a difference due to the membrane types, system setup, or the lack of repeated studies for many of the simulation strain rates currently examined. However, these findings indicate that the transition strain rate may be relatively close for similar phospholipid types. Yield and failure vs ln(loading rate)

Recall from Figure 4.1 that the yield stress was lower than the failure stress during the lower strain rates and higher than failure stress during the higher shown strain rates. Due to this change of order, these properties can be used to further narrow down transition strain rate. The empirical equation derived by Evans, et al. [27] has been used to make this comparison. Essentially, both properties are plotted against the natural log of the loading rate, as shown in Figure 4.3. The equibiaxial and strip biaxial strain states have been separated due to the yield to failure difference being much larger for the strip biaxial strain state. In Figure 4.3(A), notice the three lowest equibiaxial loading rate simulations (cases 72x0.1y0.1S1, 72x0.2y0.2S1, and 72x0.6y0.6S1) are on the left of where the two lines intersect, indicating they are below the transition point. Additionally, the strip biaxial cases with the lowest strain rates fall on the intersection of the lines,

which is consistent with observations in Section 4.4.1. Despite this separation, the strain states independently give similar results of 1.2 x 10^{11} MPa·s^{-1} for the equibiaxial strain state and 0.97 x 10^{11} MPa·s^{-1} for the strip biaxial strain state. Correlating these values to Table 4.1 for the different strain states gives von Mises strain rates of approximately 2.6 × 10^{8} s^{-1} and 1.4 × 10^{8} s^{-1} for the equibiaxial and strip biaxial strain states, respectively. Both of these values fall within the estimates from above. Considering the similar values, the strain states can be assumed to have the same transition point, so the averaged value is ~1.4 × 10^{8} s^{-1}.

While the empirical relation derived by Evans, et al. [27] has proven to describe the data after fitting for the constants to the current data, the constants differ drastically from those found by Evans, et al. [27]. This difference reinforces the idea there is more than one high rate regime than those originally tested experimentally and fit by Evans, et al. [27]. However, because the data still follows the same trend, there are likely multiple loading rate regimes for which determined constants are valid. For example, Evans, et al. [27] found a $\nu_{0\delta}$ = ~0.2 s^{-1} for similar phospholipid types to those currently examined. This is much lower than the values found in Table 4.2. Physically, it is reasonable to expect that the nucleation rate $\nu_{0\delta}$ would increase with the deformation rate. However, the reason why the constants do not change over a range of loading rates, leading to defined regimes, may not be as readily apparent. The authors believe these loading rate regimes correspond to physical phenomena. In this case, the constants found above correspond to loading rates where the phospholipid bilayer cannot adequately rearrange to form the typical energetically favored pore form, resulting in the expansion of multiple pores that are less circular. This implies in addition to the linear curve and transition point currently

identified, there may be a series of strain rates that transition into additional linear regimes both above and below the currently examined strain rates. If true, it may be possible to identify similar linear curve with different constants until the regime (and constants) observed experimentally by Evans, et al. [27] are found, although this task may be computationally prohibitive currently.

4.4.3 Implications for Traumatic Brain Injury

The results herein show that multiple strain rate regimes exist for the phospholipid bilayer. This finding has important implications related to TBI. First, it shows the bilayer can withstand a much higher instant loading at high strain rates, meaning the cell membrane may have a much higher resilience to high rate impulse deformations than experimental studies may suggest. Unfortunately, the finding that larger pore growth during lower strain rates could be a negative implication. Since these large pores open at lower strain rate, they may also be more likely to cause a loss of homeostasis at those rates. This could mean that injury scenarios that result in a deformation impulse may not be as detrimental as a slower injury that may not seem bad, at least in regard to mechanoporation. However, this does not necessarily mean the neuron would be safe because other organelles that are not as resistant to impulse deformations may still cause neuron death if damaged. This finding shows how important it is to develop a mechano-physiological internal state variable material model that can capture these complex injury mechanism.

4.5 Conclusions

The current study has examined the existence of a high strain rate behavioral transition of the POPC phospholipid bilayer. A transition strain rate was successfully determined to be at a von Mises strain rate of ~1.4×10^8 s^{-1}. Several aspects of membrane mechanical properties were examined to help determine this strain rate. First, the stress-strain response was examined, showing that the yield stress is larger than the failure stress above this strain rate and smaller than the failure stress below this strain rate (Figure 4.1). Additionally, below this strain rate, pores tend to grow larger and are more circular leading to lower failure strains (Figure 4.2). Finally, the empirical relation derived by Evans, et al, [27] was exploited to pinpoint a more exact behavioral transition strain rate (Figure 4.3). This relation was also used to determine properties of interest, such as nucleation rate (Table 4.2).

4.6 Acknowledgements

This material is based upon work supported by the Department of Agricultural and Biological Engineering and the Center for Advanced Vehicular Systems at Mississippi State University. Further, material presented in this paper is a product of the CREATE-GV Element of the Computational Research and Engineering Acquisition Tools and Environments (CREATE) Program sponsored by the U.S. Department of Defense HPC Modernization Program Office. This effort was sponsored under contract number W912HZ-13-C-0037.

4.7 References

[1] M. Faul, L. Xu, M. M. Wald, and V. G. Coronado, "Traumatic Brain Injury in the United States: Emergency Department Visits, Hospitalizations, and Deaths 2002-2006," ed. Atlanta (GA): Centers for Disease Control Prevention, National Center for Injury Prevention and Control, 2010.

[2] I. Humphreys, R. L. Wood, C. J. Phillips, and S. Macey, "The costs of traumatic brain injury: a literature review," *ClinicoEconomics and outcomes research : CEOR,* vol. 5, pp. 281-7, 2013. doi: 10.2147/CEOR.S44625.

[3] A. A. Hyder, C. A. Wunderlich, P. Puvanachandra, G. Gururaj, and O. C. Kobusingye, "The impact of traumatic brain injuries: A global perspective," *NeuroRehabilitation,* vol. 22, 2007.

[4] M. F. Kraus, T. Susmaras, B. P. Caughlin, C. J. Walker, J. A. Sweeney, and D. M. Little, "White matter integrity and cognition in chronic traumatic brain injury: a diffusion tensor imaging study," *Brain,* vol. 130, pp. 2508-2519, October 1, 2007 2007. doi: 10.1093/brain/awm216.

[5] I. Cernak, B. Stoica, K. R. Byrnes, S. D. Giovanni, and A. I. Faden, "Role of the Cell Cycle in the Pathobiology of Central Nervous System Trauma," *Cell Cycle,* vol. 4, pp. 1286-1293, 2005.

[6] M. T. Begonia, R. Prabhu, J. Liao, W. R. Whittington, A. Claude, B. Willeford*, et al.*, "Quantitative analysis of brain microstructure following mild blunt and blast trauma," *Journal of Biomechanics,* vol. 47, pp. 3704-3711, 11/28/ 2014. doi: 10.1016/j.jbiomech.2014.09.026.

[7] M. LaPlaca and L. Thibault, "Anin vitro traumatic injury model to examine the response of neurons to a hydrodynamically-induced deformation," *Annals of Biomedical Engineering,* vol. 25, pp. 665-677, 1997/07/01 1997. doi: 10.1007/BF02684844.

[8] M. C. LaPlaca, D. K. Cullen, J. J. McLoughlin, and R. S. Cargill Ii, "High rate shear strain of three-dimensional neural cell cultures: a new in vitro traumatic brain injury model," *Journal of Biomechanics,* vol. 38, pp. 1093-1105, 2005/05// 2005. doi: 10.1016/j.jbiomech.2004.05.032.

[9] M. C. LaPlaca and G. R. Prado, "Neural mechanobiology and neuronal vulnerability to traumatic loading," *Journal of Biomechanics,* vol. 43, pp. 71-78, 1/5/ 2010. doi: 10.1016/j.jbiomech.2009.09.011.

[10] K. Miller, "Constitutive model of brain tissue suitable for finite element analysis of surgical procedures," *Journal of Biomechanics,* vol. 32, pp. 531-537, 1999/05// 1999. doi: 10.1016/S0021-9290(99)00010-X.

[11] K. K. Mendis, R. L. Stalnaker, and S. H. Advani, "A Constitutive Relationship for Large Deformation Finite Element Modeling of Brain Tissue," *Journal of Biomechanical Engineering,* vol. 117, pp. 279-285, 1995. doi: 10.1115/1.2794182.

[12] T. El Sayed, A. Mota, F. Fraternali, and M. Ortiz, "A variational constitutive model for soft biological tissues," *Journal of Biomechanics,* vol. 41, pp. 1458-1466, 2008 2008. doi: 10.1016/j.jbiomech.2008.02.023.

[13] R. Prabhu, M. F. Horstemeyer, M. T. Tucker, E. B. Marin, J. L. Bouvard, J. A. Sherburn*, et al.*, "Coupled experiment/finite element analysis on the mechanical response of porcine brain under high strain rates," *Journal of the Mechanical Behavior of Biomedical Materials,* vol. 4, pp. 1067-1080, 2011. doi: 10.1016/j.jmbbm.2011.03.015.

[14] B. Rashid, M. Destrade, and M. D. Gilchrist, "Mechanical characterization of brain tissue in tension at dynamic strain rates," *Forensic Biomechanics,* vol. 33, pp. 43-54, 2014/05// 2014. doi: 10.1016/j.jmbbm.2012.07.015.

[15] R. J. H. Cloots, H. M. T. Gervaise, J. A. W. van Dommelen, and M. G. D. Geers, "Biomechanics of Traumatic Brain Injury: Influences of the Morphologic Heterogeneities of the Cerebral Cortex," *Annals of Biomedical Engineering,* vol. 36, pp. 1203-1215, 2008/07/01 2008. doi: 10.1007/s10439-008-9510-3.

[16] N. C. Colgan, M. D. Gilchrist, and K. M. Curran, "Applying DTI white matter orientations to finite element head models to examine diffuse TBI under high rotational accelerations," *Progress in Biophysics and Molecular Biology,* vol. 103, pp. 304-309, 12// 2010. doi: 10.1016/j.pbiomolbio.2010.09.008.

[17] R. Prabhu, M. F. Horstemeyer, Y. Mao, J. L. Bouvard, E. B. Marin, L. N. Williams*, et al.*, "Simulation Based Analysis of an Experimentally Quantified Traumatic Brain Injury from an In-Theater Blast Explosion.," *(Under review, PNAS),* 2014.

[18] T. El Sayed, A. Mota, F. Fraternali, and M. Ortiz, "Biomechanics of traumatic brain injury," *Computer Methods in Applied Mechanics and Engineering,* vol. *197*, pp. 4692-470, 2008. doi: 10.1016/j.cma.2008.06.006.

[19] B. Rashid, M. Destrade, and M. D. Gilchrist, "Mechanical characterization of brain tissue in compression at dynamic strain rates," *Journal of the Mechanical Behavior of Biomedical Materials,* vol. 10, pp. 23-38, 2012/06// 2012. doi: 10.1016/j.jmbbm.2012.01.022.

[20] B. Rashid, M. Destrade, and M. D. Gilchrist, "Mechanical characterization of brain tissue in simple shear at dynamic strain rates," *Journal of the Mechanical Behavior of Biomedical Materials,* vol. 28, pp. 71-85, 2013/12// 2013. doi: 10.1016/j.jmbbm.2013.07.017.

[21] M. F. Horstemeyer, *Integrated Computational Materials Engineering (ICME) for Metals: Using Multiscale Modeling to Invigorate Engineering Design with Science*: Wiley, 2012.

[22] M. F. Horstemeyer and P. Wang, "Cradle-to-grave simulation-based design incorporating multiscale microstructure-property modeling: Reinvigorating design with science," *Journal of Computer-Aided Materials Design,* vol. 10, pp. 13-34, 2003. doi: 10.1023/b:jcad.0000024171.13480.24.

[23] O. Farkas, J. Lifshitz, and J. T. Povlishock, "Mechanoporation Induced by Diffuse Traumatic Brain Injury: An Irreversible or Reversible Response to Injury?," *J Neurosci,* vol. 26, pp. 3130-40, Mar 22 2006. doi: 10.1523/JNEUROSCI.5119-05.2006.

[24] D. Kilinc, G. Gallo, and K. A. Barbee, "Mechanically-induced membrane poration causes axonal beading and localized cytoskeletal damage," *Experimental Neurology,* vol. 212, pp. 422-430, 8// 2008. doi: 10.1016/j.expneurol.2008.04.025.

[25] D. M. Geddes, R. S. Cargill, 2nd, and M. C. LaPlaca, "Mechanical stretch to neurons results in a strain rate and magnitude-dependent increase in plasma membrane permeability," *J Neurotrauma,* vol. 20, pp. 1039-49, Oct 2003. doi: 10.1089/089771503770195885.

[26] O. Farkas and J. T. Povlishock, "Cellular and subcellular change evoked by diffuse traumatic brain injury: a complex web of change extending far beyond focal damage," in *Progress in Brain Research*. vol. Volume 161, T. W. John and I. R. M. Andrew, Eds., ed: Elsevier, 2007, pp. 43-59.

[27] E. Evans, V. Heinrich, F. Ludwig, and W. Rawicz, "Dynamic tension spectroscopy and strength of biomembranes," *Biophys J,* vol. 85, pp. 2342-50, Oct 2003. doi: 10.1016/S0006-3495(03)74658-X.

[28] K. Koshiyama and S. Wada, "Molecular dynamics simulations of pore formation dynamics during the rupture process of a phospholipid bilayer caused by high-speed equibiaxial stretching," *Journal of Biomechanics,* vol. 44, pp. 2053-8, 2011/07/28/ 2011. doi: 10.1016/j.jbiomech.2011.05.014.

[29] M. A. Murphy, M. F. Horstemeyer, S. R. Gwaltney, T. Stone, M. LaPlaca, J. Liao*, et al.*, "Nanomechanics of phospholipid bilayer failure under strip biaxial stretching using molecular dynamics," *Modelling and Simulation in Materials Science and Engineering,* vol. 24, p. 055008, 2016. doi: 10.1088/0965-0393/24/5/055008.

[30] T. Shigematsu, K. Koshiyama, and S. Wada, "Effects of Stretching Speed on Mechanical Rupture of Phospholipid/Cholesterol Bilayers: Molecular Dynamics Simulation," *Scientific Reports,* vol. 5, p. 15369, 10/16/online 2015. doi: 10.1038/srep15369.

[31] M. D. Tomasini, C. Rinaldi, and M. S. Tomassone, "Molecular dynamics simulations of rupture in lipid bilayers," *Experimental Biology and Medicine (Maywood, N.J.),* vol. 235, pp. 181-8, Feb 2010. doi: 10.1258/ebm.2009.009187.

[32] S. Plimpton, "Fast Parallel Algorithms for Short-Range Molecular Dynamics," *Journal of Computational Physics,* vol. 117, pp. 1-19, 3/1/ 1995. doi: 10.1006/jcph.1995.1039.

[33] J. B. Klauda, R. M. Venable, J. A. Freites, J. W. O'Connor, D. J. Tobias, C. Mondragon-Ramirez*, et al.*, "Update of the CHARMM All-Atom Additive Force Field for Lipids: Validation on Six Lipid Types," *Journal of Physical Chemistry B,* vol. 114, pp. 7830-7843, 2010/06/17 2010. doi: 10.1021/jp101759q.

[34] J. B. Klauda. (n.d., June 23). *Laboratory of Molecular & Thermodynamic Modeling*. Available: http://mackerell.umaryland.edu/CHARMM_ff_params.html

[35] W. Shinoda, M. Shiga, and M. Mikami, "Rapid estimation of elastic constants by molecular dynamics simulation under constant stress," *Physical Review B,* vol. 69, p. 134103, 04/07/ 2004.

[36] A. Leach, *Molecular Modelling: Principles and Applications (2nd Edition)*. Harlow, England: Prentice Hall, 2001.

CHAPTER V

CONCLUSIONS

While mechanoporation has been observed to result in TBI, the underlying stress, strain, and damage limits for mechanoporation and the effect of strain state, strain rate, and planar area on these properties have not been previously quantified for a membrane structure. The current studies have quantified the nanoscale stress and mechanoporation damage responses for a simplified phospholipid bilayer as a representative model of a neuronal membrane during TBI. Several important findings were revealed as a result. The first study, CHAPTER II, showed that the equibiaxial strain paths resulted in higher stress and lower nucleation and failure strains. Study 1 also showed that the variation due to the initial structure was relatively small. The second study, CHAPTER III, showed that the strain rate affected the stress response but not the failure response. However, the third study, CHAPTER IV, showed that the stress response, pore growth, and failure strain changed below a behavioral transition von Mises strain rate of approximately 1.4×10^8 s^{-1}. Lastly, the second study showed that the structure size did not affect the results. Additionally, despite finding that both strain rate and strain state affecting the stress response, stress did not appear to cause any kind of actual damage to the membrane.

While these findings show the mechanical response due to the applied deformations, they must be considered in the context of developing the nanoscale portion

of a mechano-physiological internal state variable (MPISV) material model for a hierarchical multiscale material model. In this context, it is beneficial look at the properties individually and the process of scaling up each in the multiscale model.

The first property to consider is yield stress, which was affected by both strain rate and strain state. However, recall that both strain state and strain rate affected the loading rate. Therefore, the loading rate may be the true property affecting the yield stress, where higher loading rates result in higher yield stresses. By reducing the dependence to a single property, scaling the yield stress up in the multiscale hierarchy can be simplified. Therefore, it may be beneficial to investigate the direct loading rate to yield stress relation.

Yield strain, the second property, was only affected by the strain rate, not strain state, with higher strain rates resulting in higher yield strains. Therefore, this property can also be passed up using only a single property which should make scaling yield strain up relatively straight forward.

Additional properties to consider scaling up are the failure strain, pore growth, and damage responses. These properties were only affected by the strain state in the higher strain rates. Therefore, it may be possible to define these properties with regards to strain state only. However, below the behavioral transition strain rate, the pore growth behavior changed, which also changes the failure and damage responses. Therefore, this determination must be done for above and below the behavioral transition strain rate.

Some of the other findings will also help with implementing these data in the MPISV material model. Importantly, the initial structure only had a small effect on the results, so implementing the uncertainty due to the initial structure should be

straightforward. Additionally, bilayer system size had no effect, so this will not need to be considered other than to consider where the length scale limit should be. Lastly, the membrane failure limit diagram (MFLD), developed in CHAPTER II, showed that the different strain states had a linear x to y strain relationship for the theoretical water threshold, failure, and theoretical calcium threshold, which are physiological events of interest in TBI. This finding should simplify implementing these properties in the MPISV material model.

The determined nanoscale mechanical properties of the phospholipid bilayer presented herein demonstrate which of the examined boundary conditions have a significant effect on which mechanical properties. These data will progress the current understanding of TBI and neuronal injury at the nanoscale and aid to develop higher fidelity macroscale TBI constitutive models through MPISVs.

CHAPTER VI

FUTURE WORK

6.1 Add Model Complexity

The current model was highly simplified in nature when compared to the true cell membrane. To create a more complex model, which is needed to make the membrane more specific to neurons, a number of different aspects can be explored.

The first potential addition would be a more physiologically accurate membrane with a complex composition of phospholipid types and cholesterol added to make the structure tissue specific. This addition actually has two parts that could be addressed. The first would need to be the introduction of other types of phospholipids and cholesterol in concentrations specific to a given tissue (brain in this case). This inclusion should provide more realistic results because the membrane's properties likely depend on the type of phospholipids present. In particular, it is known that cholesterol affects the membrane's mechanical properties, such as stiffness [1], and simulations have shown that introducing cholesterol increases the failure limit [2]. Second would be to account for the phospholipid inequality between the bilayer leaflets. Building the membrane can be accomplished using membrane building tools, which can handle the tasks of leaflet inequality and distribute phospholipids to meet specified concentrations [3, 4]. However, it is necessary to determine the appropriate concentrations to be used. While I have managed to find some work describing the phospholipid components of human brain [5],

it did not specify the individual phospholipid types, only categories. Alternatively, using the results for a non-human mammalian brain may work [6], or we could try to perform the experiments based on the methods of Mitchell, et al. [6] to determine the phospholipid concentrations found in the human brain.

The second addition would be to add ions in the water to determine if they would penetrate the bilayer during the simulation time. It is possible statistically, assuming it is possible for the ion penetration would occur, to perform this simulation using typical molecular dynamics. However, this may not be an efficient simulation method and the possibility of steered molecular dynamics should potentially be explored in conjunction with introducing an ion gradient.

The third addition would be to include portions of the cytoskeleton. Although computationally, it may be more appropriate to treat this addition as a simulation of its own assuming the result could be related back to those of the phospholipid bilayer.

The fourth addition would be a small protein or rigid body representing a protein body. This would primarily be intended to serve as pre-existing object that would create an additional restraint when deforming the bilayer to determine if the bilayer fails more easily when objects similar to proteins are inserted.

6.2 Multiscale Implementation

A large portion of this study has focused on quantifying nanoscale injury mechanisms with the intent of implementing this data into a Mechano-Physiological Internal State Variable (MPISV) model for TBI. Therefore, further investigating the requirements to and adding this data to the MPISV model is a future goal of this work.

The multiscale hierarchical diagram shown in Figure 3.1 demonstrates the idea of a mechano-physiological internal state variable model that would allow for more accurate TBI models. The mechano-physiological part means the model has both mechanical and physiological properties, both of which are needed to model TBI. A finite element model sits at the top of this hierarchy. However, this finite element model cannot inherently capture lower length scale damage without an internal state variable (ISV) material model developed from the lower length scales. For each length scale, relevant parameters are identified by scaling down. These parameters are then quantified and passed up to the relevant length scales. For this hierarchy, the length scales range from the atomic to macroscale, each with their own properties of interest.

The current studies have focused on high rate mechanisms, such as pore nucleation and growth, on the nanoscale, which would be passed up via bridge 6 in Figure 3.1. By quantifying properties of interest on this length scale, a form of cell damage, mechanoporation in this case, can be implemented in the material model for the overall finite element model. As mentioned in the overall conclusions, CHAPTER V, the stress-strain, failure strain, pore growth and nucleation, and damage were calculated for this purpose, which can be passed up to the macroscale. Diffusion rates can also be analyzed from this length scale to provide evidence for if a cell would likely die from the applied deformations, which would impact the viability for groups of cells. Moving further up the length scale, the bulk mechanical properties would also be implemented from the tissue scale. Altogether, implementing mechanoporation damage in the material model may allow researchers to create finite element models that can estimate localized cell death in an affected area of the brain during a given injury scenario. This ability

would allow the analysis and development of optimized safety devices via computational methods with a true rubric of device effectiveness.

6.3 Additional Strain States

In the current study, it has been determined that, out of those tested, the biaxial deformation conditions were the most detrimental. However, additional strain states exist that can be tested to further elucidate the deformation and failure of the phospholipid bilayer. Two strain states that would provide potentially relevant data with regard the motivation of TBI.

The first is compression, which would be potentially experienced during a multitude of injury situations, such as contusions due to the brain impacting the interior of the skull and blast wave damage. These would result in two lines of simulations depending on rate because the blast wave simulation would result in much higher strain rates than that of normal injury.

The second is shear which can be experienced during TBI diffuse axonal injury (DAI). During DAI, the neuron axon fiber experiences shear which can lead to damage leading to eventual cell death. Performing simulations shearing the bilayer will help to determine if this damage is partially due to bilayer failure or purely an effect of the underlying cytoskeletal damage.

6.4 References

[1] D. Needham and R. S. Nunn, "Elastic deformation and failure of lipid bilayer membranes containing cholesterol," *Biophysical Journal,* vol. 58, pp. 997-1009, 10// 1990. doi: 10.1016/S0006-3495(90)82444-9.

[2] T. Shigematsu, K. Koshiyama, and S. Wada, "Molecular dynamics simulations of pore formation in stretched phospholipid/cholesterol bilayers," *Chemistry and Physics of Lipids,* vol. 183, pp. 43-49, 10// 2014. doi: 10.1016/j.chemphyslip.2014.05.005.

[3] S. J. Marrink, H. J. Risselada, S. Yefimov, D. P. Tieleman, and A. H. de Vries, "The MARTINI Force Field: Coarse Grained Model for Biomolecular Simulations," *The Journal of Physical Chemistry B,* vol. 111, pp. 7812-7824, 2007/07/01 2007. doi: 10.1021/jp071097f.

[4] E. L. Wu, X. Cheng, S. Jo, H. Rui, K. C. Song, E. M. Dávila-Contreras*, et al.*, "CHARMM-GUI Membrane Builder toward realistic biological membrane simulations," *Journal of Computational Chemistry,* vol. 35, pp. 1997-2004, 2014. doi: 10.1002/jcc.23702.

[5] J. S. O'Brien and E. L. Sampson, "Lipid composition of the normal human brain: gray matter, white matter, and myelin," *Journal of Lipid Research,* vol. 6, pp. 537-544, October 1, 1965 1965.

[6] T. W. Mitchell, K. Ekroos, S. J. Blanksby, A. J. Hulbert, and P. L. Else, "Differences in membrane acyl phospholipid composition between an endothermic mammal and an ectothermic reptile are not limited to any phospholipid class," *Journal of Experimental Biology,* vol. 210, pp. 3440-3450, 2007-10-01 00:00:00 2007. doi: 10.1242/jeb.007286.

APPENDIX A

CHAPTER II SUPPLEMENTAL FIGURES

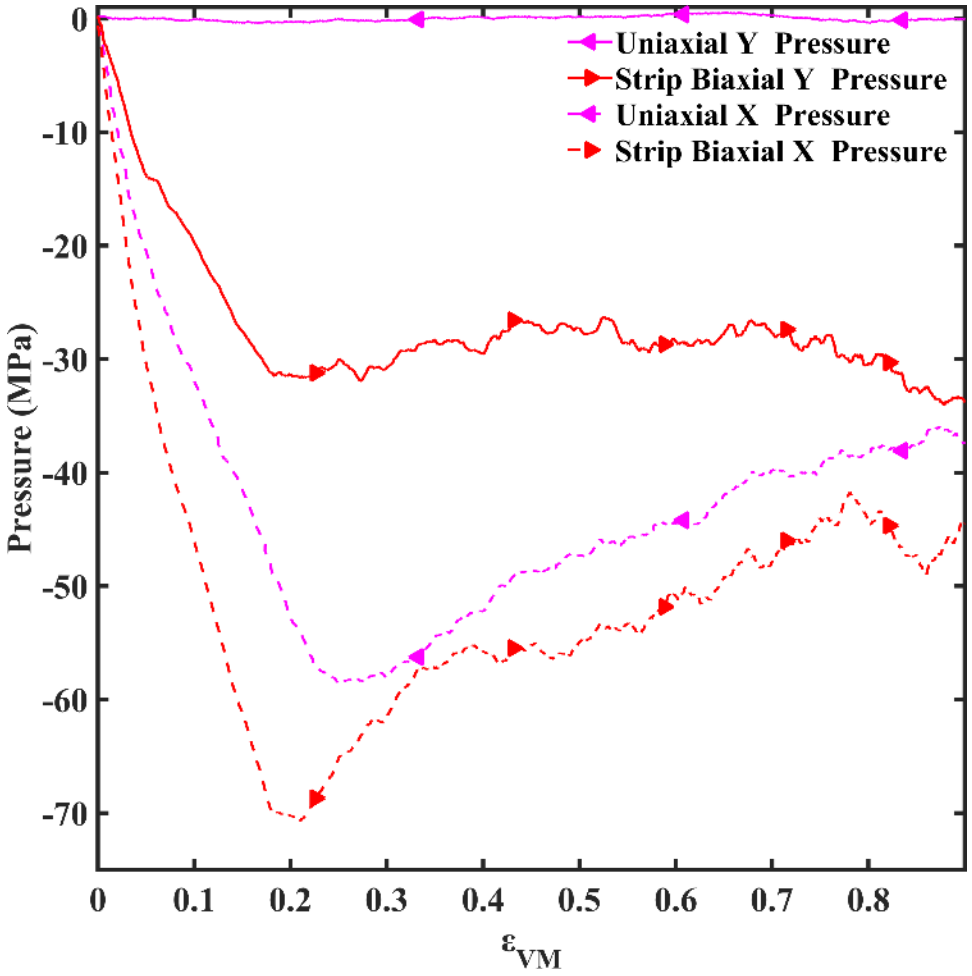

Figure A.1 Strip biaxial and uniaxial component pressure comparison

Representative comparison of the x and y component pressures (stresses) versus von Mises strain for the strip biaxial and uniaxial strain states at $\dot{\varepsilon}_{VM} = 5.5 \times 10^8\ s^{-1}$.

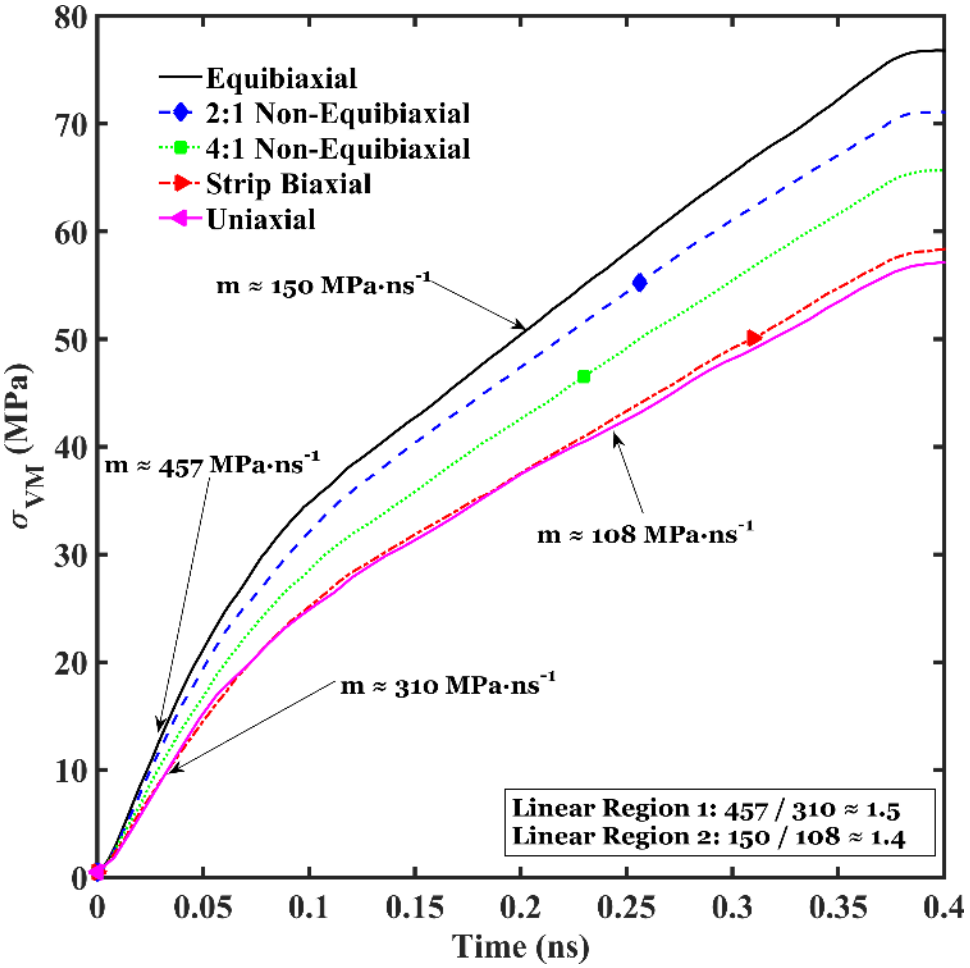

Figure A.2 Loading rate for different strain paths.

Average von Mises stress versus time curve displaying the effect of the strain path (equibiaxial, 2:1 non-equibiaxial, 4:1 non-equibiaxial, strip biaxial, and uniaxial) simulated on loading rate at $\dot{\varepsilon}_{VM} = 5.5 \times 10^{8}\ s^{-1}$.

APPENDIX B

SURFACE TENSION CALCULATION AND JUSTIFICATION

This appendix has been published previously in the journal Modelling and Simulation in Materials Science and Engineering as supplementary information (doi: 10.1088/0965-0393/24/5/055008).

The magnitude of the surface tension is affected by the height l_z (surface tension equation: $\gamma = \sigma_z - (\sigma_x + \sigma_y)/2) * l_z$ with the stresses being independent of the box height. When close to equilibrium, this affect is largely negligible due to the pressure term $\sigma_z - (\sigma_x + \sigma_y)$ becoming a small or zero value because the principle stresses are isotropic, but the pressure term becomes larger during non-equilibrium scenarios because the lateral pressures are much larger than the perpendicular pressure (which remains ~1 atm during deformations). In far from equilibrium cases, the effect of l_z on the surface tension value calculated using the above equation is greatly affected by the rapidly decreasing simulation box height, as shown in Figure B.1. Therefore, an approximation for l_z is needed that only includes the bilayer height with a layer of water, so we chose to use the height of the bilayer plus a ~15 Å layer of water. This method is valid because only the region near the interface is contributing to the surface tension [1]. This limitation has also been mentioned in other simulation papers of phospholipid bilayer deformations, but they said the use of the equation was acceptable due to the water layer becoming "reasonably small" during deformations [2].

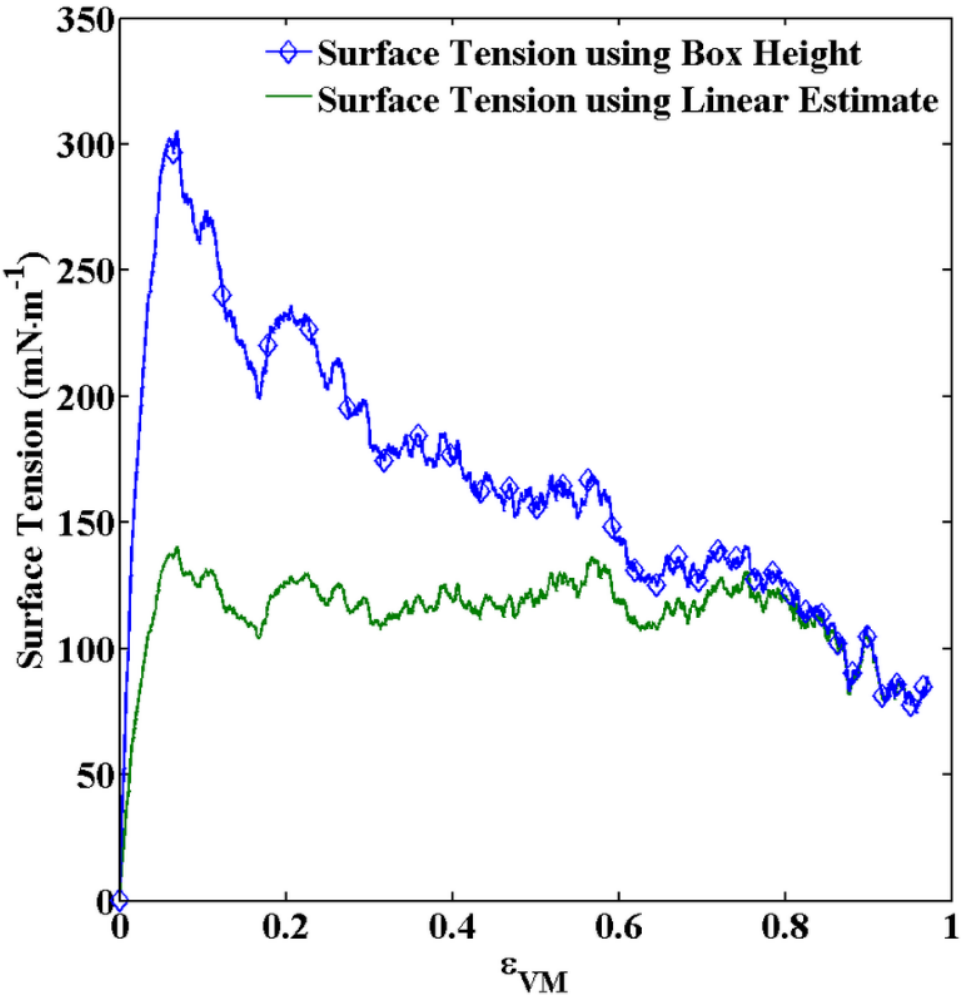

Figure B.1 Comparison of surface tension calculation using box height and linear estimate for the 72x1 (72 lipid, x = 1.0 m·s^{-1}, y = 0.0 m·s^{-1}) case.

The decrease in height of the bilayer was estimated to decrease linearly from 60 Å to the final box height, which included the final bilayer height plus a layer of water approximately 15 Å thick. Figure B.2 has a comparison of the heights for the simulation box, estimates, and measured values taken from coordinate files and shows that the post-deformation box height gives a good approximation of the bilayer with a 15 Å water layer. Additionally, due to the layer of water being present post-deformation, there is still

enough water to avoid interactions between phospholipid bilayer periodic images. With this approximation, the surface tension and von Mises stress result in similar curve trends, shown in Figure B.3.

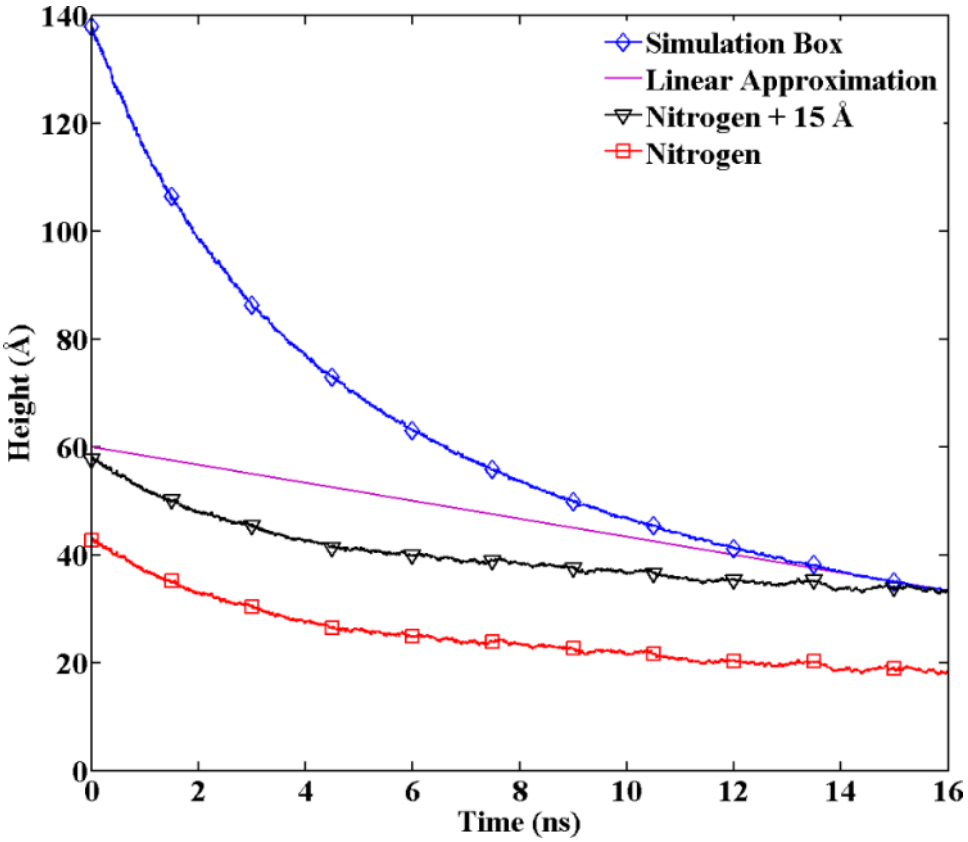

Figure B.2 Comparison of simulation box, linear estimate, nitrogen plus a 15 Å layer of water, nitrogen, and phosphorus heights for the 72x1 (72 lipid, x = 1.0 $m \cdot s^{-1}$, y = 0.0 $m \cdot s^{-1}$) case.

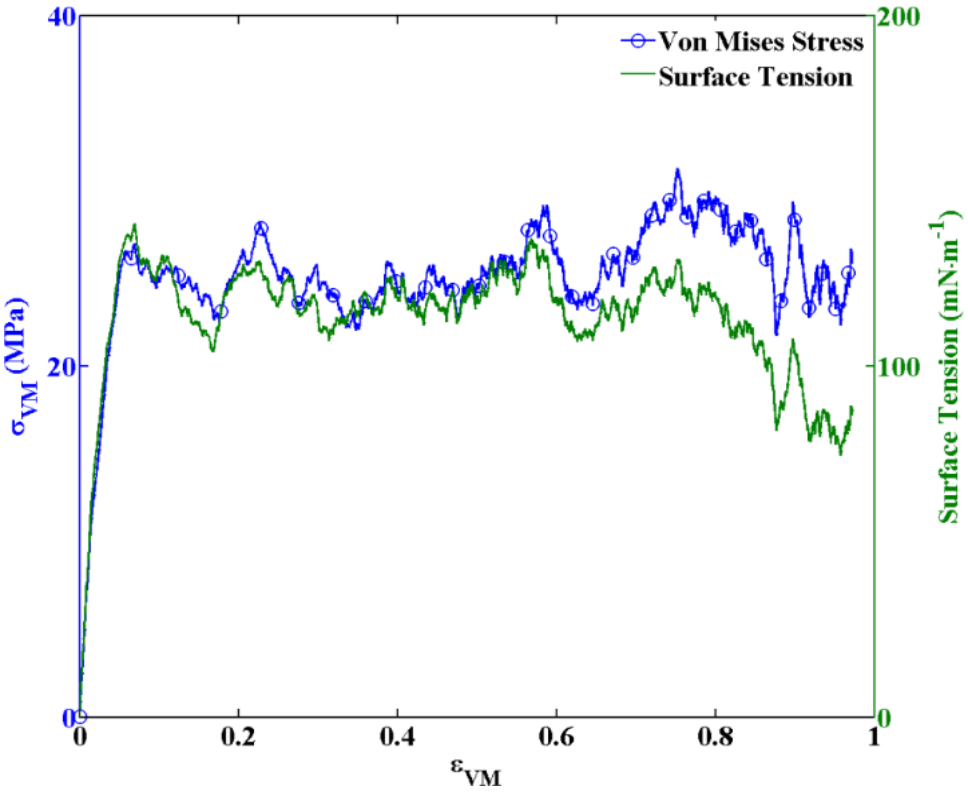

Figure B.3 Comparison of surface tension (using linear estimate) versus von Mises strain curve and the von Mises stress-strain curve for the 72x1 case (72 lipid, x = 1.0 $m \cdot s^{-1}$, y = 0.0 $m \cdot s^{-1}$) case.

A.1 References

[1] Y. Zhang, S. E. Feller, B. R. Brooks, and R. W. Pastor, "Computer simulation of liquid/liquid interfaces. I. Theory and application to octane/water," *The Journal of Chemical Physics,* vol. 103, pp. 10252-10266, 1995. doi: 10.1063/1.469927.

[2] K. Koshiyama and S. Wada, "Molecular dynamics simulations of pore formation dynamics during the rupture process of a phospholipid bilayer caused by high-speed equibiaxial stretching," *Journal of Biomechanics,* vol. 44, pp. 2053-8, 2011/07/28/ 2011. doi: 10.1016/j.jbiomech.2011.05.014.

APPENDIX C

CHAPTER III SUPPLEMENTAL FIGURE

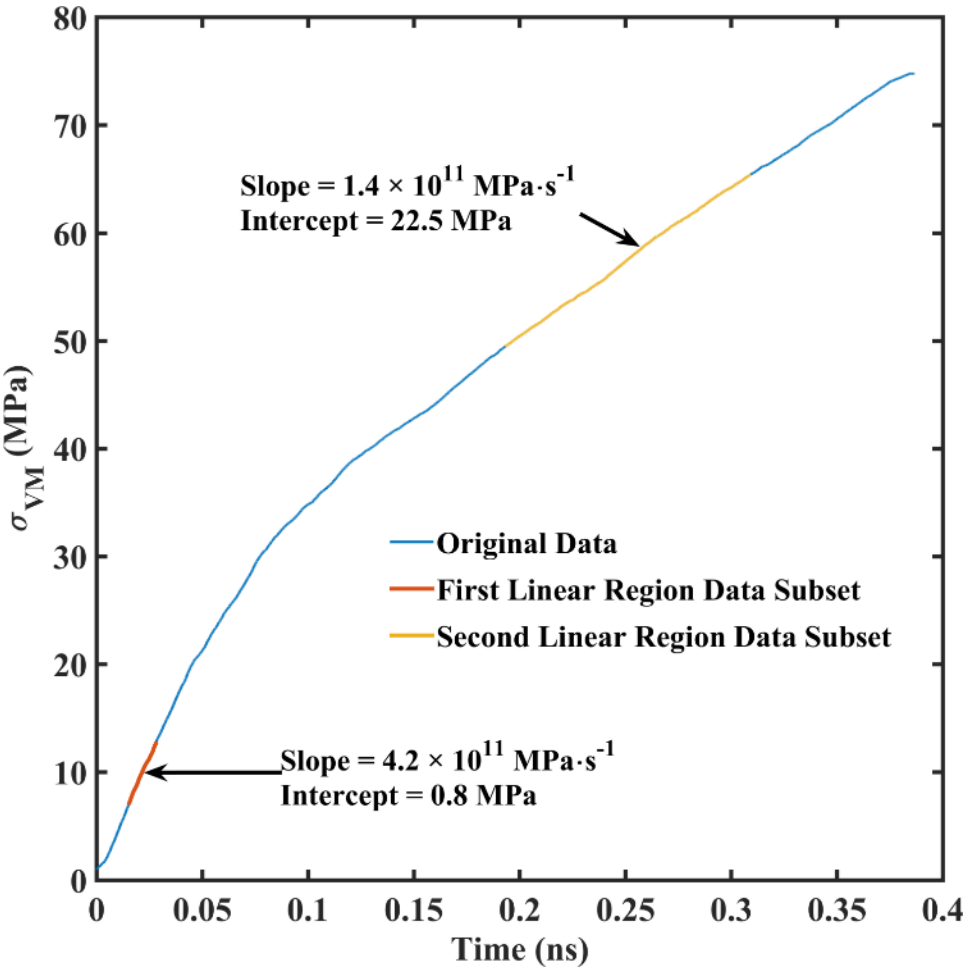

Figure C.1 Representative von Mises stress versus time curve demonstrating distinct loading regions and slope determination.

The slope from the first linear region data subset gives $\Re_\sigma$.

APPENDIX D

CHAPTER IV SUPPLEMENTAL DATA AND FIGURES

Table D.1 Comparison of Select Equibiaxial Simulations To Previous Studies

Case Name	Lipids	X Dimension (nm) *	Y Dimension (nm) *	v_x (m/s)	v_y (m/s)	$\dot{\varepsilon}_{VM}$ (s^{-1}) *
Prabhu 1	-	-	-	-	-	33.33
Prabhu 2	-	-	-	-	-	166.67
Prabhu 3	-	-	-	-	-	300
Prabhu 4	-	-	-	-	-	366.67
Prabhu 5	-	-	-	-	-	500
Koshiyama 1	128	6.32	6.32	0.1	0.1	1.05×10^7
Koshiyama 2	128	6.32	6.32	0.3	0.3	3.16×10^7
Koshiyama 3	128	6.32	6.32	1.0	1.0	1.05×10^8
72x0.1y0.1	72	4.89 Å	4.61	0.1	0.1	1.40×10^7
72x0.2y0.2	72	4.89 Å	4.61	0.2	0.2	3.30×10^7
72x0.6y0.6	72	4.89 Å	4.61	0.6	0.6	8.70×10^7
72x2.8y2.7	72	4.89 Å	4.61	2.8	2.7	3.90×10^8
72x4.0y3.8	72	4.89 Å	4.61	4.0	3.8	5.50×10^8

*Values approximated for Prabhu and Koshiyama cases where appropriate
Prabhu cases are from Prabhu et al [1]. Data is for high-rate uniaxial porcine brain tests.
Koshiyama cases are from Koshiyama and Wada [2]

Table D.2 Summary of Moduli, Yield, and Failure Values

Case Name*	Elastic Modulus 1 (MPa)*	Elastic Modulus 2 (MPa)	σ_{Yield}^{VM} (MPa) *	ε_{Yield}^{VM} *	$\sigma_{Failure}^{VM}$ (MPa) *	$\varepsilon_{Failure}^{Vm}$ *	$\frac{Area_{Failure}}{Lipid}$ (nm^2) *
Prabhu 1	-	-	0.02	-	-	-	-
Prabhu 2	-	-	0.04	-	-	-	-
Prabhu 3	-	-	0.11	-	-	-	-
Prabhu 4	-	-	0.21	-	-	-	-
Prabhu 5	-	-	0.32	-	-	-	-
Koshiyama 1	380.6	N/A	7.5	0.012	12.5	0.267	1.39
Koshiyama 2	507.5	N/A	10.0	0.012	14.2	0.282	1.46
Koshiyama 3	847.5	N/A	16.7	0.012	15	0.315	1.61
72x0.1y0.1	1205.3	N/A	9.5	0.006	19.5	0.332	1.7
72x0.2y0.2	1259.2	N/A	18.5	0.013	27.3	0.366	1.88
72x0.6y0.6	1047.8	635.4	27.5	0.034	29.3	0.365	1.87
72x2.8y2.7	1009.9	383.79	64.8	0.138	59.7	0.421	2.21
72x4.0y3.8	830.84	307.69	75	0.190	69.8	0.425	2.24

*Values approximated for Prabhu and Koshiyama cases. Data is for high-rate uniaxial tests of porcine brain.

Table D.3 Summary of Strains for Initial Pore Nucleation and Growth Of Pores To Allow Theoretical Passage Of Molecules Through The Membrane

Case Name	$\varepsilon_{FirstPore}$	$\varepsilon^{H_20}_{FirstPore}$	$\varepsilon^{Ca^{2+}}_{FirstPore}$
72x0.1y0.1	0.049	0.244	0.362
72x0.2y0.2	0.026	0.287	0.413
72x0.6y0.6	0.065	0.345	0.446
72x2.8y2.7	0.159	0.316	0.501
72x4.0y3.8	0.138	0.342	0.495

Table D.4 Summary of Nucleation (η), Pore Growth (ν), and Damage (ϕ) Values at Points of Interest

Case Name	η_{Yield}	ν_{Yield}	ϕ_{Yield}	$\eta_{Failure}$	$\nu_{Failure}$	$\phi_{Failure}$
72x0.1y0.1	0	0	0	0.333	1.491	0.495
72x0.2y0.2	0	0	0	0.536	1.979	1.060
72x0.6y0.6	0	0	0	0.456	2.443	1.113
72x2.8y2.7	3.29×10^{-3}	0.260	8.53×10^{-4}	0.587	5.815	3.414
72x4.0y3.8	6.10×10^{-3}	0.566	3.45×10^{-3}	0.399	7.392	2.951

*Mean pore area is used to represent pore growth but is technically pore growth times coalescence ($\nu * c$)

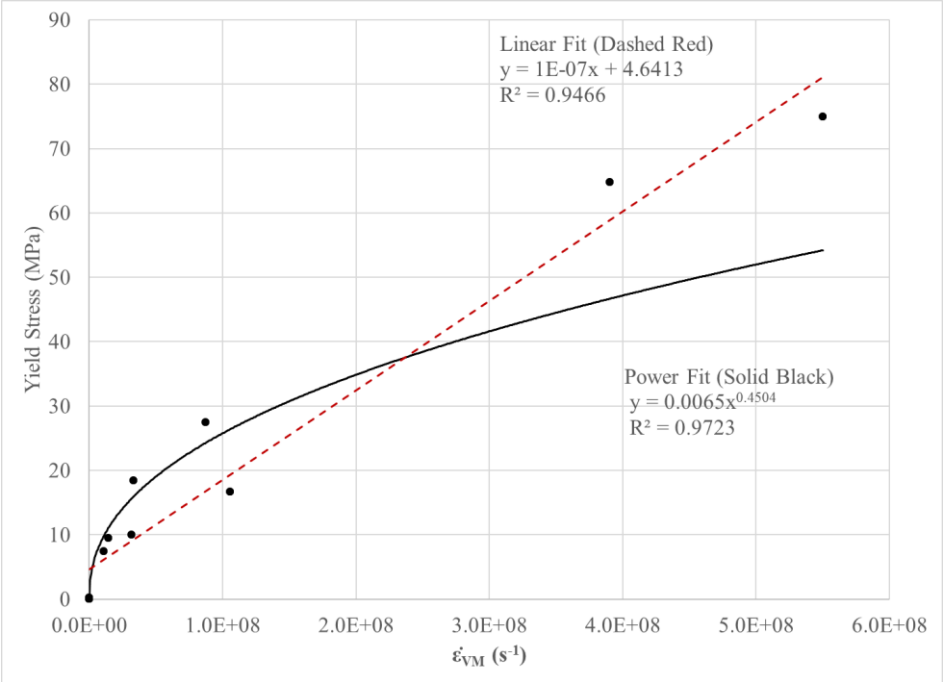

Figure D.1 Yield stress vs strain rate curve with linear and power fits for the cases in Table D.1.

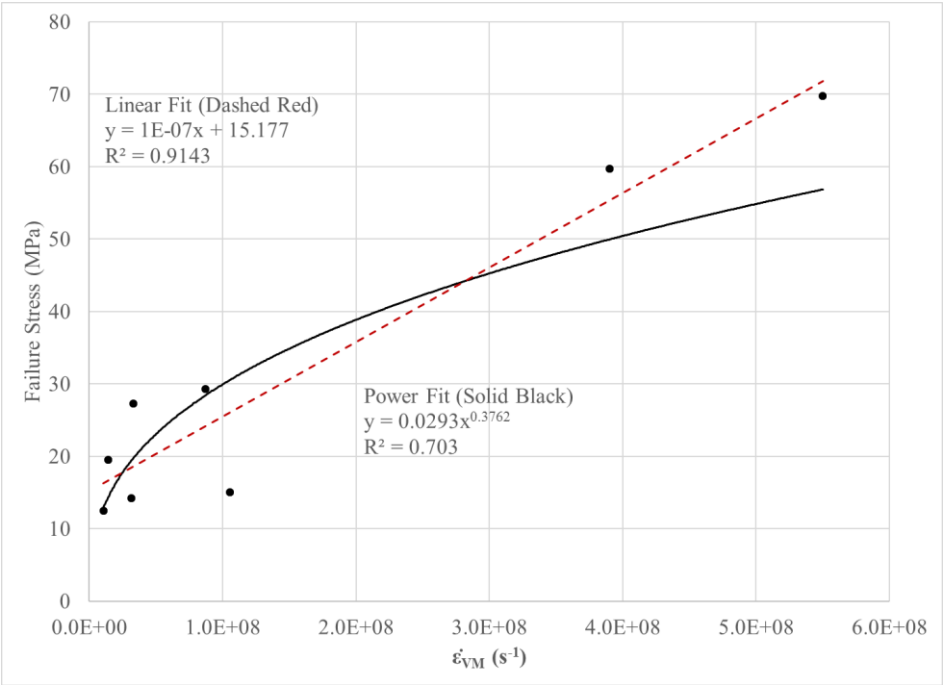

Figure D.2 Failure stress vs strain rate curve with a linear and power fits for the cases in Table D.1 except Prabhu cases.

A.2 References

[1] R. Prabhu, M. F. Horstemeyer, M. T. Tucker, E. B. Marin, J. L. Bouvard, J. A. Sherburn*, et al.*, "Coupled experiment/finite element analysis on the mechanical response of porcine brain under high strain rates," *Journal of the Mechanical Behavior of Biomedical Materials,* vol. 4, pp. 1067-1080, 2011. doi: 10.1016/j.jmbbm.2011.03.015.

[2] K. Koshiyama and S. Wada, "Molecular dynamics simulations of pore formation dynamics during the rupture process of a phospholipid bilayer caused by high-speed equibiaxial stretching," *Journal of Biomechanics,* vol. 44, pp. 2053-8, 2011/07/28/ 2011. doi: 10.1016/j.jbiomech.2011.05.014.

APPENDIX E

EFFECT OF STREAMING VELOCITY REMOVAL

Streaming velocities were not removed during deformation simulations. To show this omission did not significantly affect the results, a comparison of the stress response (Figure E.1), deformed structure (Figure E.2), and other properties (Table A.1) with and without the velocity correction are provided.

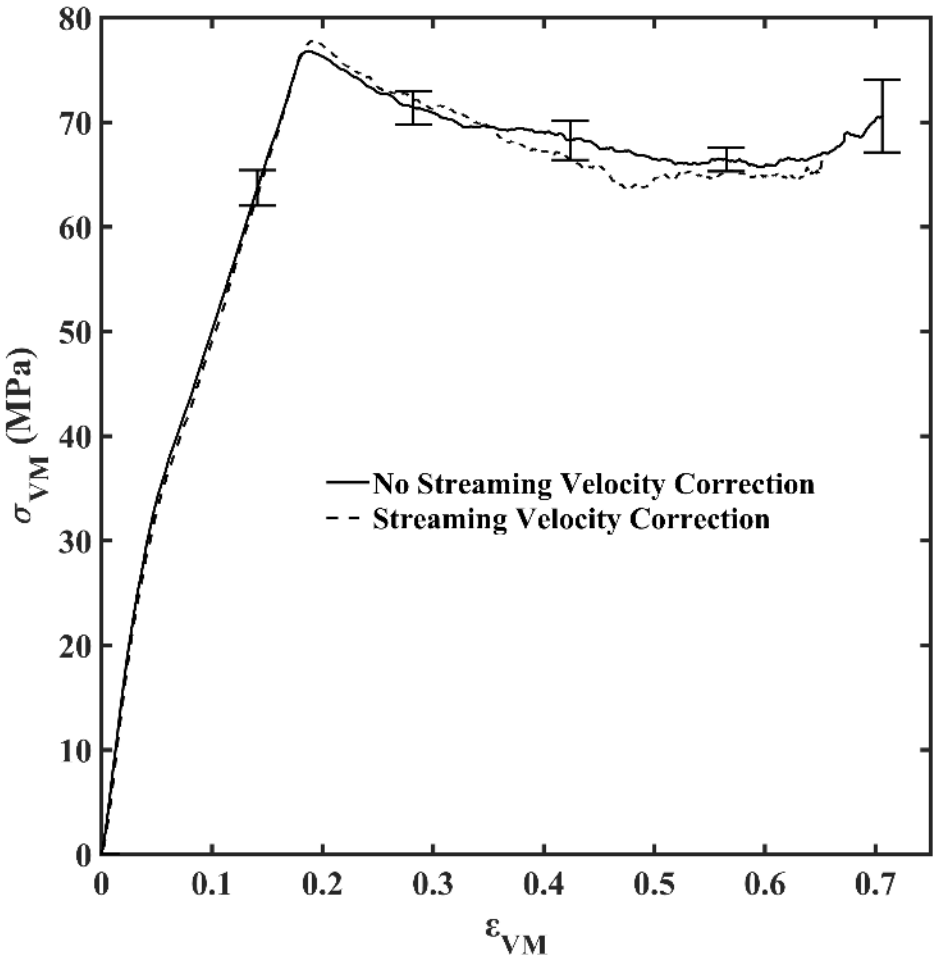

Figure E.1 Stress vs strain comparing with and without streaming velocity correction

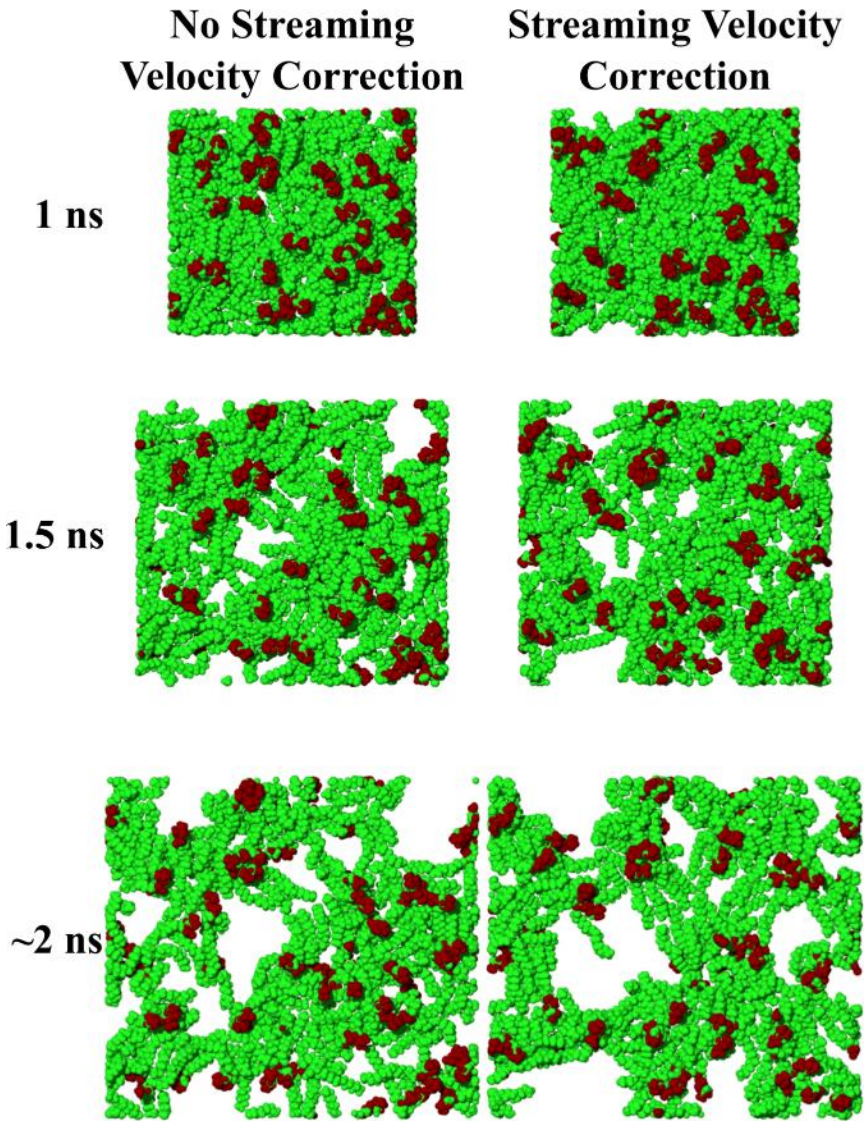

Figure E.2 Comparison of representative deformed equibiaxial structure with and without velocity streaming correction

Table A.1 Comparison of Peak Time, Failure Time, and Failure Stress

Property	No Streaming Velocity Correction	Streaming Velocity Correction
Peak Stress Time	0.5289	0.5259
Failure Time	1.2 ± 9.7%	0.99
~Failure Stress (MPa)	68.9	68.9